

Northwestern University

Characterization of Carbon Nanotube Reinforced Cementitious Materials

A dissertation

submitted to the graduate school
in partial fulfillment of the requirements for the degree

Doctor of Philosophy

Field of Civil and Environmental Engineering

by

Yuan Gao

Evanston, Illinois

September, 2018

Abstract

Recently, there has been increasing interest in exploring nano-materials used as an additive to existing concrete materials. With respect to fiber-shaped nanomaterials such as carbon nanofibers (CNF), many studies have shown that mechanical strength properties of cementitious materials can be improved significantly. In this dissertation, the research has focused on the development of nanomodified cementitious materials with CNF. With relatively low CNT dosages (0.05% to 0.1% to cement weight) and a unique dispersion approach, uniform incorporation of CNT into a cementitious matrix is possible. The beneficial increase in properties such as flexural strength, fracture roughness, modulus of elasticity, autogenous shrinkage, shrinkage cracking resistance, and electrical conductivity are all of particular note. For the case of flexural strength and modulus of elasticity, the percentage improvement in properties with CNT is larger with mortar and concrete than it is with cement paste– this unexpected result implies that nano- and micro-structural changes are occurring in the presence of CNT at interfacial transitional zone between bulk paste and aggregates. To approve above statement, nano-scale metrology techniques have been adopted to investigate mechanical and chemical properties of ITZ in CNF reinforced cement concrete. The samples of cement mortar and cement concrete with and without CNFs are prepared. The quantitative nano-mechanical mapping (based on atomic force microscopy, AFM) technique is adopted to measure the Young's modulus of ITZ. The elemental and phase investigation of the SEM samples are carried out by Energy-dispersive X-ray (EDX). Based on the fundamental chemical composition in ITZ, the Ca to Si ratio is calculated, which proves a potential modification of nanostructure in C-S-H gel. Furthermore, a new numerical modelling considering real interfacial condition is established,

and ITZ effect is discussed based on numerical simulation. In addition, transport properties have been investigated which proves that CNF is able to reduce the water absorption rate and chloride penetration depth indicating a refinement of microstructure of cement matrix. The investigation of hydration rate using FTIR and calorimetry test doesn't find an accelerate or delay effect of the nanomaterials, and other possible mechanisms on property improvement are needed for future work. Each of these topics represents one of the few barriers remaining to commercialization of CNT/CNF as a beneficial admixture for concrete production, demonstrating the large potential impact of this fundamental characterization research.

Acknowledgment

I express my sincere gratitude towards my advisor Prof. Surendra P. Shah for his guidance and support throughout this work. He has always motivated and encouraged me to grow in my career. The job and enthusiasm he has for her research was contagious and motivational for me, especially during tough times in the Ph.D. pursuit. He has guided so many students and they all become successful in their career. I am thankful to be one of them who is advised by the world-renowned research scientist of cementitious material.

I am also grateful to my co-advisor Prof. David Corr for his guidance and encouragement. He is always helpful on my research and my life at Northwestern University. He is very supportive for introducing me to other specialists in many national and international conferences that facilitated fruitful discussions and international collaboration.

I greatly acknowledge our collaborator, Prof. Maria Konsta-Ddoutos for her valuable suggestions and constructive suggestions on numerous occasions. Her knowledge on CNT added cementitious material is always valuable for my research at NU. I also thank Prof. Mark Hersam, for his valuable suggestions and participation in my qualifier and defense committee. His novel ideas on the dispersion of nanomaterials were an inspiration, making this interdisciplinary work a great learning experience for me.

I gratefully acknowledge the funding sources that made my PhD work possible. I was funded by the CEMEX company for my first year of research. My work was also supported by the Australia Research Council Nanocomm Hub.

Lastly, I would like to thank my family for all their love and encouragement. For my parents who raised me with a love of science and supported me in all my pursuits. They have devoted their time taking care my young daughter so I can focus on my research and my defense. Also, my loving, supportive, encouraging, and patient husband Haitao Liu whose faithful support during the final stages of this PhD is so appreciated. And most of all for my beloved daughter, Zoey Liu, who is God's gift to me and I can't express how much I love her. Thanks so much to come to my life.

Table of Contents

Acknowledgment -----	1
Abstract -----	3
Table of Contents -----	5
List of Figures -----	9
List of Tables -----	15
Chapter 1 Introduction -----	16
1.1 Background	
1.2 Carbon Nanotubes	
1.3 CNT-polymer Composites	
1.3.1 Fiber-reinforced Concrete	
1.3.2 Challenges and Limitations of CNT's Application in Cementitious Materials	
1.4 Research Significance and Objectives	
1.5 Structures of This Dissertation	
Chapter 2 Literature Review -----	29
2.1 Introduction	
2.2 Dispersion for CNTs	
2.2.1 Chemical Agitation	
2.2.1.1 Noncovalent Approach	
2.2.1.2 Covalent Approach	
2.2.2 Mechanical Agitation	
2.2.3 Characterization of Dispersion Results	
2.2.3.1 Imaging Techniques	
2.2.3.2 Ultraviolet-visible Spectroscopy	
2.2.3.3 Other methods?	
2.2.4 Re-agglomeration Phenomenon within Cement Matrix	
2.3 Research Work on CNT Reinforced Cementitious Materials	

2.3.1 Mechanical Properties

2.3.2 Electrical Properties

2.3.3 Durability

2.4 Motivation and Objectives

Chapter 3 Experimental Work with CNT Reinforced Cementitious Materials at Macro Scale -----53

3.1 Introduction

3.2 Dispersion Method

3.3 Materials

3.4 Mechanical Properties

3.4.1 Three-point bending

3.4.2 Compression Test

3.5 Autogenous Shrinkage and Shrinkage Cracking

3.5.1 Autogenous shrinkage measurement

3.5.2 Restrained ring test

3.6 Experiment Results and Discussions

3.6.1 Mechanical tests

3.6.2 Autogenous shrinkage

3.6.3 Restrained ring test

3.7 Summary

Chapter 4 Experimental Work with CNT Reinforced Cementitious Materials at Nano Scale -----79

4.1 Introduction

4.2 Nanomechanical Characterization with CNT Reinforced Cement Composite

4.2.1 PeakForce Quantitative Nanoscale Mechanical Characterization

4.2.2 Sample preparation

4.2.3 Test process

4.2.4 Test results

4.3 SEM/EDS Test with CNT Reinforced Cement Composite

4.4 Summary

Chapter 5 Simulation of CNT Reinforced Concrete-----103

4.1 Introduction

5.2 Model development

5.2.1 Spherical symmetry

5.2.2 Axisymmetry

5.2.3 Effective aggregate considering interphase effect

5.3 FEM simulation process

5.3.1 Sample preparation

5.3.2 Gray-scale image analysis

5.3.3 Input experiment results

5.3.4 Finite element simulation

5.4 Results and discussion

5.4.1 Comparison and validation

5.4.2 Influencing factor analysis

5.5 Summary

Chapter 6 Cement Hydration-----131

6.1 Introduction

6.2 FTIR test

6.2.1 FTIR spectra of several fundamental samples

6.2.2 FTIR study on cement paste mixed with SP

6.2.3 FTIR study on cement paste incorporating CNTs

6.3 Semi-adiabatic calorimetry test

6.4 XRD test

6.5 Summary

Chapter 7 Transport Properties of CNT Reinforced Concrete-----147

7.1 Introduction

7.2 Experiment methods

7.2.1 Water sorptivity test

7.2.2 Chloride penetration depth

7.2.3 Half-cell potential test

7.3 Experiment results

7.3.1 Water sorptivity test

7.3.2 Chloride penetration test

7.3.3 Half-cell potential test

7.4 Summary

Chapter 8 Conclusions and Scope of Future Work-----160

8.1 Conclusions

8.2 Scope of Future Work

List of Figures

Figure 1.1 TEM image of CNT

Figure 1.2 High resolution image of CNF

Figure 1.3 TEM images of cement-CNT hybrids

Figure 1.4. Typical load-elongation curve for glass fiber in tension

Figure 2.1 Schematic of defect functionalization of CNT

Figure 2.2 Schematic of noncovalent functionalization of CNTs

Figure 2.3 Sonication probe (photo courtesy from Sonics)

Figure 2.4 Schematics of ball milling technique (a) and container (b)

Figure 2.5 High-shear mixing of CNT and asphalt

Figure 2.6 Typical UV-vis spectrum of CNTs in aqueous solution

Figure 2.7 Evolution of the maximum absorbance of 0.1 wt% CNTs for different SDS concentrations

Figure 2.8 Effect of sonication energy on the flexural strength of cement paste reinforced with 0.048 wt% CNFs

Figure 2.9 Modulus of elasticity E for cement paste and mortar with 0.1 wt% CNTs

Figure 2.10 Piezoresistive behavior of cement composites with 0.1 wt% of CNT or CNF

Figure 2.11 Autogenous shrinkage of cement paste with 0.025 or 0.048 wt% of CNT

Figure 2.12 Probability plots of the Young's modulus of cement paste with CNTs

Figure 2.13 Half-cell potential versus time for CNT or CNF reinforced cement mortars

Figure 3.1 Schematic diagram of dispersion process

Figure 3.2 Sonication tip

Figure 3.3 Schematic diagram of UV-Vis spectroscopy and an example of CNT's spectrum

Figure 3.4 Absorbance of samples with different ultrasonication time

Figure 3.5 Peak absorbance Vs. Sonication energy

Figure 3.6. Grading of coarse aggregate

Figure 3.7 Higher Resolution Image of Carbon Nanofiber from *Pyrograf Products*

Figure 3.8 Set-up of flexural test

Figure 3.9 Set-up of compression test

Figure 3.10 Set up of autogenous shrinkage test

Figure 3.11 Set up of restrained ring test

Figure 3.12 Restrained ring sample and portable microscope

Figure 3.13 Three-point bending results of cement paste: a) flexural strength; b) Young's modulus

Figure 3.14 Three-point bending results of cement mortar: a) flexural strength; b) Young's modulus

Figure 3.15 Autogenous shrinkage for: (a) cement paste (w:c=0.4); (b) cement mortar (w:c:s=0.4:1:2.75); (c) high performance mortar(HPM) (w:c:s=0.34:1:1.75)

Figure 3.16 Restrained ring test of cement mortar with or without CNF

Figure 4.1 Ca/Si ratio vs. distance from aggregate surface

Figure 4.2 AFM equipment

Figure 4.3 Test area for AFM-QNM (mortar without CNFs)

Figure 4.4 Test area for AFM-QNM (mortar with CNFs)

Figure 4.5 Test area for AFM-QNM (concrete without CNFs)

Figure 4.6 Test area for AFM-QNM (concrete with CNFs)

Figure 4.7 Topography of ITZ (a) without CNF and (b) with CNF

Figure 4.8 Roughness of test samples (a) with CNF and (b) without CNF

Figure 4.9 Test process of PeakForce Tapping Mode

Figure 4.10 Nanoscope Analysis interface

Figure 4.11 Schematic photo of spherical AFM tip

Figure 4.12 Tip-separation curve

Figure 4.13 Young's modulus of concrete with CNF

Figure 4.14 Young's modulus of concrete without CNF

Figure 4.15 Histogram of Young's modulus for interface area of mortar

Figure 4.16 Histogram of Young's modulus for interface area of concrete

Figure 4.17 Hitachi SU8030 SEM

Figure 4.18 SEM photo of CNF added concrete sample

Figure 4.19 Line protocol of SEM/EDS results on an area containing aggregate, ITZ, and bulk paste

Figure 4.20 Ca/Si ratio of plain concrete

Figure 4.21 Ca/Si ratio of CNF added concrete

Figure 4.22 The probability of Ca/Si within ITZ of concrete specimens from SEM/EDS

Figure 5.1 Models describing the interfacial zone

Figure 5.2 Calculation of effective Young's modulus and effective Poisson's ratio of inclusion based on spring layer interface model

Figure 5.3 FEM simulation process

Figure 5.4 Gray-scale image processing

Figure 5.5 Input parameters for the simulation model

Figure 5.6 Aggregate profile in FEM model

Figure 5.7 Von Mises stress contours and strain contours for FEM simulations of cement concrete (a) without or (b) with CNFs

Figure 5.8 Effect of Young's modulus of aggregate on that of concrete under different ITZ Young's modulus

Figure 5.9. Effect of Young's modulus of aggregate on that of concrete under different ITZ thickness

Figure 5.10. Effect of Young's modulus of cement mortar on that of concrete under different ITZ Young's modulus

Figure 5.11. Effect of Young's modulus of cement mortar on that of concrete under different ITZ thickness

Figure 5.12. Effect of properties of ITZ on Young's modulus of concrete

Figure 5.13. Strain contours for FE simulations of cement concrete with different ITZ properties

Figure 6.1 FTIR spectra of CNT sample

Figure 6.2 FTIR spectra of dry cement

Figure 6.3 FTIR spectra of plain cement at 7 days

Figure 6.4 Shift of silicon-oxygen stretching vibration

Figure 6.5 FTIR spectra of cement pastes with or without SP: (a) at 8h; (b) at 9h; (c) at 10h; (d) at 11h; (e) at 12h

Figure 6.6 FTIR spectra of cement pastes with or without CNTs: (a) at 8h; (b) at 9h; (c) at 10h; (d) at 11h; (e) at 12h

Figure 6.7 Picture of semi-adiabatic calorimetry

Figure 6.8 Semi-adiabatic calorimetry result

Figure 7.1 Schematic of water sorptivity test

Figure 7.2 Set-up of chloride penetration test

Figure 7.3 Colorimetric measurement of penetration depth

Figure 7.4 Half-cell Potential (Ag/AgCl) as a function of exposure time for reinforced cement mortars in 3.5 wt% NaCl Solution

Figure 7.5 Schematic of half-cell potential testing

Figure 7.6 Reinforced concrete sample for half-cell potential testing

Figure 7.7 Water absorption rate of concretes containing 0.1 wt% CNF

Figure 7.8 The difference of penetration depth between (a) plain concrete; (b) concrete with CNF

List of Tables

Table 3.1 Chemical composition of cement

Table 3.2 Carbon nanofiber properties

Table 3.3 Mix composition for autogenous shrinkage test

Table 3.4. Results on compression test for concrete with or without CNF

Table 3.5 Summary table for the effect of CNF within cement composites

Table 3.6 Comparison of autogenous shrinkage and shrinkage cracking results

Table 4.1 Roughness of test samples

Table 4.2 MOE on ITZ for mortar of concrete from AFM-QNM test

Table 4.3 Ca/Si ratio of the major hydrated phases

Table 5.1 Mix proportions of cylindrical samples

Table 5.2 Compression Test Results for Mortar and Concrete Cylinders

Table 5.3. Input parameters for numerical simulation

Table 5.4 Young's parameters of partial aggregates in Sample 1

Table 5.5 Young's parameters of partial aggregates in Sample 2

Table 5.6 Comparison of Young's modulus between simulation results and test results

Table 7.1 Sorptivity value of concrete containing CNFs after 14 days of curing

Chapter 1

Introduction

1.1 Background

Cement nanocomposites is a cementitious material that utilizes nanomaterials or with nanomaterials added in which the size of the nano particles is less than 500 nm. It is believed that the addition of nanomaterial increase the strength as well as durability of conventional concrete. The need of developing cement nanocomposites, or nano concrete starts from the increasing demand for ultra-high performance concrete since the early millennium. Popular nano-reinforcement for cement material includes nano silica, carbon nanotube (CNT), graphene oxide (GO), and nano alumina. Due to the extreme small dimension of nanomaterials, they have the potential to modify the nanostructure of the cement matrix and improve bulk properties in nanoscale. Nano particles can perform a filler effect by refining the intersectional zone in cement and densify the structure. Also, the excellent mechanical properties of nanomaterials can target

on the downside of concrete materials, such as low tensile strength and modulus of elasticity, large shrinkage. However, the high cost and difficulties in handling nanomaterials still limit the use of them in construction industry. The research with CNT reinforced cementitious materials has started more than a decade ago. With the dropping cost of the CNT materials and their successfully utilization in many composite materials, the amount of studies with CNT added cementitious materials keep increasing and many new advantages has been found.

1.1.1 Carbon Nanotubes

Since carbon nanotubes were first discovered by Iijima in 1991, they had drawn a large attention. He produced multiwalled carbon nanotubes (MWNTs) through arc-discharge evaporation[1]. The method is initially used for producing C₆₀ fullerenes, creating CNTs through arc-vaporization of two carbon rods placed end to end in an enclosure that is filled with low pressure gas. The discovery of CNTs stimulated researchers worldwide to search for new forms of carbon due to their stable structures other than graphite and diamond. However, CNT-related commercial activity has develops most rapidly during the past decade, and the number of CNT-related publications and issue patents continues to increase.

CNTs are tube-shaped graphitic carbon with excellent mechanical, electrical and thermal properties. There can be one or more layers of graphene sheet, with open or closed ends. Single-layer CNTs are typically ranges from 0.8 to 2 nm and multi-wall CNTs (MWNTs) are typically 5-20 nm, although MWNTs can exceed 100 nm. The length of CNTs ranges from less than 100 nm to several centimeters (see Fig 1.1). The carbon nanofiber (CNF) is a special form of CNT, which is typically 50-150 nm in diameter. The aspect ratio of CNT is around 1000. With a hollow structure as the CNT, the CNF has graphite plane canted out from the longitudinal

direction (Fig. 1.2). They share similar properties and effects in composites, so they are referred as CNT in this thesis for brevity. CNTs have excellent mechanical, electrical and thermal properties, which makes them a great candidate to improve the tensile strength, Young's modulus, and electrical conductivity of cement-based materials. The elastic modulus of CNTs are approximately 1 TPa, which is 5 times high than steel. And the tensile strength is approximately 100 GPa, which is 50 times higher than steel[2]. The CNT walls made of graphene sheets can be metallic or semiconducting, and it can carry currents of up to 10^9 A/cm²[3]. CNTs can have great thermal conductivity of 3500 W/m·K, which is greater than diamond[4].

CNTs are firstly produced by the arc discharge method as mentioned earlier, however the method is not suitable for large-scale production. High-volume production of CNT uses mainly chemical vapor deposition (CVD) of hydrocarbons over a metal catalyst. The scaling-up, using of low-cost feedstocks have substantially decreased MWNT prices, which also promotes the development of CNT reinforced composites. CNTs produced by the CVD process often have large quantities of structure defects, which can lead to reduced mechanical, electronic and thermal properties compared for pristine nanotubes. The Young's modulus and the tensile strength of CVD-MWNT are reported to be 0.45 TPa and ~4 GPa, respectively[5].

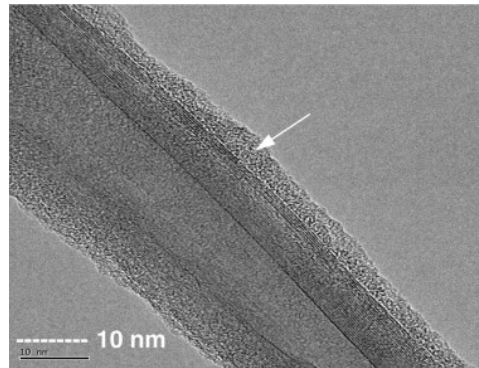


Figure 1.1 TEM image of CNT (photo courtesy from Nanoshel)

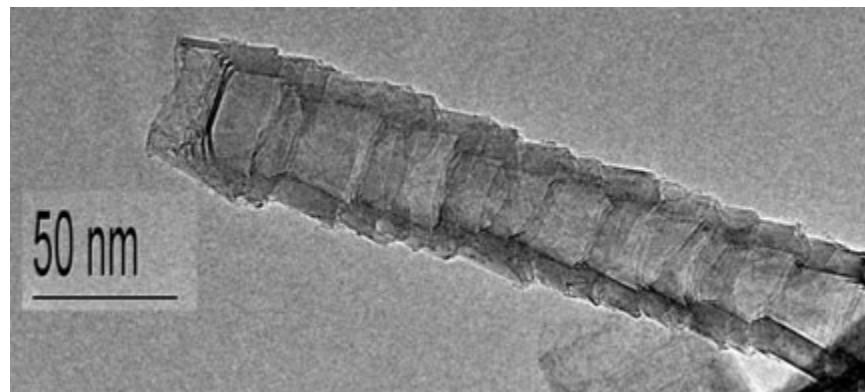


Figure 1.2 High resolution image of CNF (photo courtesy from Pyrograf Products)

1.1.2 CNT-polymer Composites

CNT has been successfully applied in many polymer composites to manipulate a material's conductivity, strength, thermal stability, static properties, and weight. To fully utilize the benefits of the nanomaterial, there are four requirements for the nano-reinforcing system[6]. These are good dispersion, large aspect ratio, alignment and interfacial stress transfer. Dispersion of nanomaterials is known to be the key factor limiting the behavior of nanocomposite, since large agglomerations due to the poor dispersion can always lead to defect sites within the composite matrix. The defect sites lowered the efficiency of load transfer and create unnecessary voids in

the system, which is detrimental to polymer's mechanical properties. The aspect ratio can be maximized by good dispersion if the CNTs are fully exfoliated. Large aspect ratio could increase the load bearing capabilities, and contact areas between the CNT and the polymer matrix. The alignment issue is less critical, since it is not always beneficial for the improvement of strength and stiffness. Interfacial shear strength is also an important factor, which determines the stress transferred from the composite matrix to the nanotubes. The interaction between nanotubes and the polymer could be covalently or noncovalently, where covalent attachment is expected to increase the interfacial shear strength of the CNT-polymer system theoretically.

So far, CNTs have mostly been utilized as electrically conductive fillers in plastics. CNT modified plastics have been extensively used in the automotive industry, where energy storage applications (batteries and supercapacitors), capacitive touch sensors can be modified with CNTs. For load-bearing applications, CNT could improve the modulus, strength, and toughness of the polymer to a certain degree[7]. CNTs are also able to improve damping properties of the polymer, and it has been used in sporting goods to replace carbon fiber, such as bicycle frames, tennis racquets, and baseball bats.

In situ polymerization of CNT has also drawn large attention because it enables large scale nanocomposite production and higher CNT contents and it always ensures a stronger bond between the nanotubes and the polymer particles. CNTs can be directly grafted onto alumina[8], copper[9], carbon fibers[10], and even cement particles[11][12]. The synthesis of CNT grafted cement particles is carried out in CVD method, which is largely used to produce CNTs. The compressive strength, flexural strength as well as electrical conductivity is found to be improved with the direct synthesis method[12].

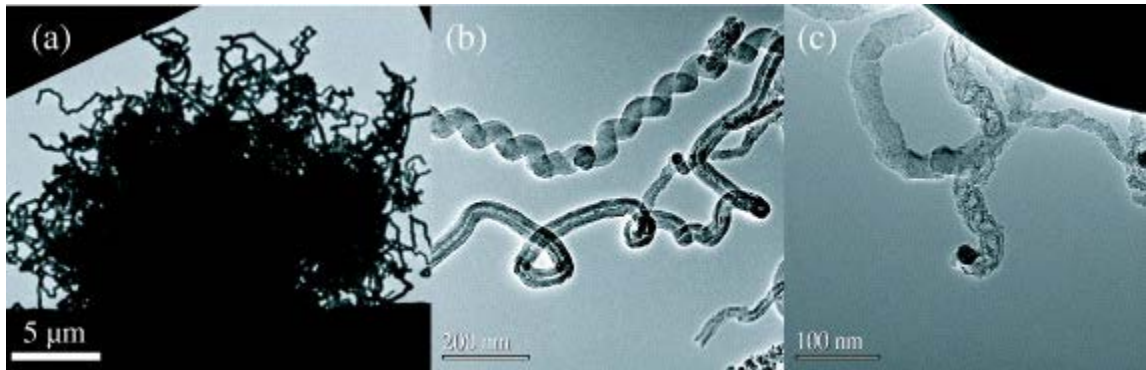


Figure 1.3 TEM images of cement-CNT hybrids[13]

1.3.1 Fiber Reinforced Concrete

Conventional fiber reinforced concrete is widely believed to have a substantially higher toughness by incorporating steel fibers in millimeter range and the volume of fibers is in the range of one percent [14]. By controlling crack width and altering the post-peak response of stress-strain curve in flexural load, micro-fibers are able to enhance the toughness of concrete materials. The fracture toughness can be measured with Jenq and Shah's two parameter model [15], Hillerborg fictitious crack model[16] and Bazant's size effect law[17]. In addition, micro-fibers are used to control shrinkage cracking in concrete slabs or pavements[18]. With cast-in-place construction, it is often difficult to add more than about 1% by volume of fibers, since the addition of fibers make concrete less workable. Depending upon the type and geometry of fibers, and the rheology of matrix, the higher the amount of fibers, the more difficult it is to uniformly disperse them. Another commonly used fiber reinforcement for concrete material is the glass fiber, which is used in the range of 4-12%. Glass fiber reinforced cement (GFRC) panels are produced by spraying glass fiber and cement slurry on a desired form, and initiate the strain hardening type of response for the material (Fig. 1.4)[19]. The strain hardening response is the

elongation behavior happened after the bend over point (BOP), which is tested under tension load.

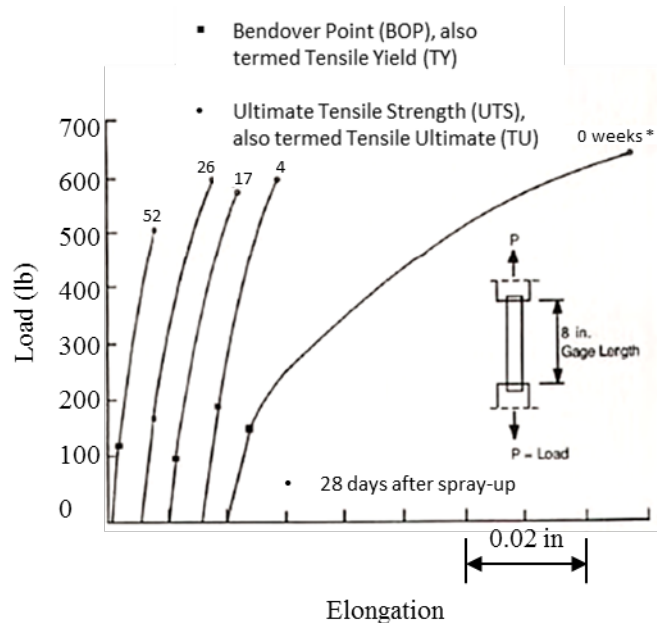


Figure 1.4. Typical load-elongation curve for glass fiber in tension[19]

In concrete structures, concrete is reinforced with steel bars or prestressing strands. The rebars or strands do not alter tensile strength (BOP) of concrete. Only after the major cracks are formed, reinforcing bars constrain these cracks so that the ultimate load is much higher than the load at cracking. High performance fiber reinforced concrete should enhance the bend over point (that is increase the tensile strength of the matrix). This is possible since fibers can interact with microcracks and delay formation of macrocracks. Microcracks are initiated from flaws in cement paste matrix. Can we constrain these flaws which are in nanoscale? These considerations have led to the development of concrete reinforced with carbon nanotube and carbon nanofibers.

1.3.2 Challenges and limitations of CNT's application in cementitious materials

Though CNTs have the potential to improve various properties of cement-based materials, it has not been largely applied in construction industry as other polymer composites. The reason is believed to be its high cost and difficulties in homogeneously distribution within cement matrix. As mentioned previously in this section, a good dispersion is crucial for cement nanocomposite's behavior, and bad dispersion is detrimental to mechanical properties by introducing unnecessary voids. In addition, the alkaline environment within cement matrix could potential create secondary agglomeration of CNTs which makes dispersion even more difficult. The high cost of nanomaterials is another issue limiting the use of nanomaterial in construction industry. The increasing interest of CNT's application in composite materials expands the production of the nanomaterials and thus reduces the cost worldwide. The initial intention of using CNTs in cement-based material comes from the wisdom of successful application of micro-fiber reinforcements. And the dosage of CNTs was similar to steel fiber ranging between 0.5-1.5% [20][21]. The results were not satisfying since the dispersion of CNTs was particularly difficult within this dosage range.

1.4 Research Significance and Objectives

The research with CNT for cement-based composites at Northwestern University started to use a much less fiber amount at around 0.1 % to cement weight. The one order magnitude of decrease in the CNT's dosage not only solve the problem of dispersion, but also lower the cost of the nanomaterial within cementitious material[22]. Preliminary studies have shown that with relative small dosages of well dispersed CNT can produce notable increases in strength properties as well as modulus of elasticity, which is quite promising and motivate the proposed study of CNT additions to concrete. A recent meeting of a committee of concrete industry leaders in Chicago is

particular interested in this study, particular the enhancement of Young's modulus due to the addition of CNTs. In tall building design, high strength concrete is often specified in order to achieve a stiff frame: high strength concrete is needed for its enhanced Young's modulus, not because the stresses in the structural frame warrant it. There is significant interest in an additive that could increase Young's modulus more economically and sustainably than high strength concrete can. The promise of developing new sustainable material systems using the well-established Portland cement industrial framework is an important motivation for this thesis.

1.5 Structure of This Dissertation

The thesis is written in the format of an article thesis as a summary of the entire PhD work. The summary consists of Chapters 1-7.

- **Chapter 1** serves as a general introduction to the materials including CNTs, CNT added polymers, and fiber reinforced cement-based composite. It clarifies the objective and challenges of using CNTs in cementitious material.
- **Chapter 2** aims to summarize previous work done on the research subject, especially the dispersion method of CNTs and its characterization techniques.
- **Chapter 3** introduces the experiment work with CNT reinforced cementitious material in macro scale. It evaluates the mechanical properties such as Young's modulus, flexural strength and compressive strength. It also discusses the well-dispersed CNTs effect on autogenous shrinkage and shrinkage cracking.
- **Chapter 4** demonstrates the characterization work with CNT reinforced cementitious material in nanoscale by using AFM-QNM, SEM/EDS. It not only presents the

mechanical modification but also the chemical modification in nanoscale due to the addition of CNTs

- **Chapter 5** utilize the results from mechanical testing and nanoscale characterizations, and develops a finite element model with the focus on the interface effect between bulk paste and aggregates.
- **Chapter 6** gives an analysis of CNT's effect on cement hydration, using FTIR, semi-adiabatic calorimetry, and XRD test.
- **Chapter 7** describes the CNT's effect on transport properties of concrete material using different experiment methods.
- **Chapter 8** is the last chapter and here both discussion and conclusions derived from the content in this thesis are given along with suggestions for future research

References:

- [1] S. Iijima, Helical microtubules of graphitic carbon, *Nature*. 354 (1991) 56.
<http://dx.doi.org/10.1038/354056a0>.
- [2] B. Peng, M. Locascio, P. Zapol, S. Li, S.L. Mielke, G.C. Schatz, H.D. Espinosa, Measurements of near-ultimate strength for multiwalled carbon nanotubes and irradiation-induced crosslinking improvements, *Nat. Nanotechnol.* 3 (2008) 626.
<http://dx.doi.org/10.1038/nnano.2008.211>.
- [3] B.Q. Wei, R. Vajtai, P.M. Ajayan, Reliability and current carrying capacity of carbon nanotubes, *Appl. Phys. Lett.* 79 (2001) 1172–1174. doi:10.1063/1.1396632.
- [4] E. Pop, D. Mann, Q. Wang, K. Goodson, H. Dai, Thermal Conductance of an Individual

- Single-Wall Carbon Nanotube above Room Temperature, *Nano Lett.* 6 (2006) 96–100.
doi:10.1021/nl052145f.
- [5] S. Xie, W. Li, Z. Pan, B. Chang, L. Sun, Mechanical and physical properties on carbon nanotube, *J. Phys. Chem. Solids.* 61 (2000) 1153–1158.
doi:[https://doi.org/10.1016/S0022-3697\(99\)00376-5](https://doi.org/10.1016/S0022-3697(99)00376-5).
- [6] J.N. Coleman, U. Khan, W.J. Blau, Y.K. Gun'ko, Small but strong: A review of the mechanical properties of carbon nanotube–polymer composites, *Carbon N. Y.* 44 (2006) 1624–1652. doi:<https://doi.org/10.1016/j.carbon.2006.02.038>.
- [7] F.H. Gojny, M.H.G. Wichmann, U. Köpke, B. Fiedler, K. Schulte, Carbon nanotube-reinforced epoxy-composites: enhanced stiffness and fracture toughness at low nanotube content, *Compos. Sci. Technol.* 64 (2004) 2363–2371.
doi:<https://doi.org/10.1016/j.compscitech.2004.04.002>.
- [8] G. Yamamoto, M. Omori, T. Hashida, H. Kimura, A novel structure for carbon nanotube reinforced alumina composites with improved mechanical properties, *Nanotechnology.* 19 (2008) 315708. <http://stacks.iop.org/0957-4484/19/i=31/a=315708>.
- [9] Direct synthesis of carbon nanofibers on the surface of copper powder, *Carbon N. Y.* 48 (2010) 4559. <http://dx.doi.org/10.1016/j.carbon.2010.07.028>.
- [10] N. De Greef, L. Zhang, A. Magrez, L. Forró, J.-P. Locquet, I. Verpoest, J.W. Seo, Direct growth of carbon nanotubes on carbon fibers: Effect of the CVD parameters on the degradation of mechanical properties of carbon fibers, 2014.
doi:10.1016/j.diamond.2014.11.002.

- [11] L. Nasibulina, I. Anoshkin, S. Shandakov, A. Nasibulin, A. Cwirzen, P. Mudimela, K. Habermehl-Cwirzen, J. Malm, T. Koltsova, Y. Tian, E. Vasilieva, V. Penttala, O. Tolochko, M. Karppinen, E. Kauppinen, Direct Synthesis of Carbon Nanofibers on Cement Particles, *Transp. Res. Rec. J. Transp. Res. Board.* 2142 (2010) 96–101. doi:10.3141/2142-14.
- [12] A novel approach to composite preparation by direct synthesis of carbon nanomaterial on matrix or filler particles, *Acta Mater.* (2013). <http://dx.doi.org/10.1016/j.actamat.2012.12.007>.
- [13] A.G. Nasibulin, S.D. Shandakov, L.I. Nasibulina, A. Cwirzen, P.R. Mudimela, K. Habermehl-Cwirzen, D.A. Grishin, Y. V Gavrilov, J.E.M. Malm, U. Tapper, Y. Tian, V. Penttala, M.J. Karppinen, E.I. Kauppinen, A novel cement-based hybrid material, *New J. Phys.* 11 (2009) 23013. <http://stacks.iop.org/1367-2630/11/i=2/a=023013>.
- [14] P.N. Balaguru, S.P. Shah, *Fiber-reinforced cement composites*, McGraw-Hill, 1992. https://books.google.com/books?id=z_ZRAAAAMAAJ.
- [15] Y. Jenq, S.P. Shah, Two Parameter Fracture Model for Concrete, *J. Eng. Mech.* 111 (1985) 1227–1241. doi:10.1061/(ASCE)0733-9399(1985)111:10(1227).
- [16] A. Hillerborg, *A model for fracture analysis*, Lund Institute of Technology, Division of Building materials, 1978.
- [17] Z.P. Bazant, J. Planas, *Fracture and size effect in concrete and other quasibrittle materials*, CRC press, 1997.

- [18] and S.P.S. Mirosław Grzybowski, Shrinkage Cracking of Fiber Reinforced Concrete, *Mater. J.* 87 (n.d.). doi:10.14359/1951.
- [19] S.P. Shah, D. Ludirdja, TOUGHNESS OF GLASS FIBER REINFORCED CONCRETE PANELS SUBJECTED TO ACCELERATED AGING., *PCI J.* 32 (1987) 82–99.
- [20] I. Campillo, J.S. Dolado, A. Porro, High-Performance Nanostructured Materials for Construction, in: *Nanotechnol. Constr.*, The Royal Society of Chemistry, 2004: pp. 215–225. doi:10.1039/9781847551528-00215.
- [21] G.Y. Li, P.M. Wang, X. Zhao, Mechanical behavior and microstructure of cement composites incorporating surface-treated multi-walled carbon nanotubes, *Carbon N. Y.* 43 (2005) 1239–1245. doi:<https://doi.org/10.1016/j.carbon.2004.12.017>.
- [22] M.S. Konsta-Gdoutos, Z.S. Metaxa, S.P. Shah, Highly dispersed carbon nanotube reinforced cement based materials, *Cem. Concr. Res.* 40 (2010) 1052–1059. doi:10.1016/j.cemconres.2010.02.015.

Chapter 2

Literature Review

2.1 Introduction

The literature review explores the recent progress that has been made on carbon nanotube (CNT) or carbon nanofiber (CNF) reinforced cementitious materials. This section is organized as follows. Section 2.2 provides an introduction to existing dispersion techniques as well as the characterization technique of dispersion results. Section 2.3 provides the extensive literature review on CNT/CNF reinforced cement composites. Section 2.4 presents the motivation and objectives of the present work.

2.2 Dispersion of CNTs

As mentioned in the previous section, CNTs have high aspect ratio (~ 1000) and thus extremely large surface area. It makes the nanomaterials tend to agglomerate due to presence of attractive forces (van der Waals). The commercialized CNTs are usually supplied in the form of heavily

entangled bundles, which results in challenges in dispersion. And the poor dispersion and rope-like entanglement of CNTs in the composite matrix always leading to many defect sites in the composites, and limiting the efficiency of CNT's effect within nanocomposite. A proper agitation must be used to break the CNT agglomerations. The process of de-agglomeration and uniform distribution of nanomaterials within composite is called dispersion. Dispersion method could be categorized to chemical agitation and mechanical agitation. Chemical agitation is used to modify the surface properties of CNTs with chemicals and mechanical agitation introduces shear force to mechanically separate CNT agglomerations. They are often combined with respect to CNT dispersions. At last, the method evaluating the dispersion effect is presented as part of dispersion techniques.

2.2.1 Chemical Agitation

In order to solve the problem related to the dispersion of CNT within cement matrix, surface modifications have to be applied. For cement nanocomposite, a proper surface modification will not only separate CNTs from agglomerations, also improve the bonding between CNTs and cement hydrates. Either covalent or non-covalent chemical agitation could be applied depending on the interactions between the particles and the matrix.

Covalent method: Covalent method is based on the covalent linkage of functional groups onto sidewalls or termini of the tubes, and it is found to increase the interfacial bonding with many polymers[1]. The most common covalent treatment is defect functionalization, which is also called oxidation functionalization[2]. Functional groups such as $-\text{COOH}$ (carboxylic acid) and $-\text{OH}$ (hydroxyl) are attached to defects on CNTs. Defect sites could be open ends and/or holes in the sidewalls, irregularities on graphene framework. They are mostly produced by reaction with

strong acids such as nitric acid (HNO_3), sulfuric acid (H_2SO_4) or their mixture[3][4](as seen in Fig 2.1), strong oxidants such as KMnO_4 , ozone and reactive plasma[5]. The treatment with HNO_3 and H_2SO_4 exert electrostatic repulsive forces overcoming the attractive force and causing exfoliation. After the acid treatment, the mixture needs to be washed with deionized water, while the pH value is maintained at neutral. Then the suspension is centrifuged can functionalized CNTs are obtained[6][7]. It also changes the nature of the CNTs from hydrophobic to hydrophilic due to the attachment of polar groups, which is quite useful for cement mixture. Other covalent method include sidewall functionalization and polarization treatment.

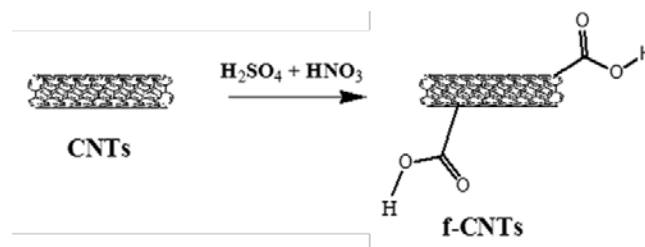


Figure 2.1 Schematic of defect functionalization of CNT

The advantage of covalent method is that it produces strong interfacial bond between CNTs and the matrix, which allows CNT-added cement composite to possess high mechanical and functional properties. The disadvantage of covalent method, however, is that it is often very aggressive and changes the intrinsic properties of the CNTs. Defects are also produced during covalent approach, resulting in degradation in mechanical properties of CNTs as well as disruption of π -electron system in nanotubes.

Noncovalent method: Noncovalent method is an alternative method to modify the surface properties of CNTs. A typical noncovalent method utilize polymers, such as polymeric polystyrene[8] or poly (p-phenylene vinylene)[9], to wrap around the CNTs to form

supermolecular complexes. The polymer wrapping treatment forms a thin layer of polymers on top of CNTs which could provide functional groups for special design purpose. Another noncovalent method utilizes surfactants to treat CNTs, where surfactants are physically adsorbed on the surface of CNTs[10]. Fig 2.2 illustrates the schematic of noncovalent chemical treatment. Surfactants attached to the CNTs can reduce surface tension of water and increase electrostatic and/or steric repulsions between tube surfaces. When combined with mechanical agitation, surfactant treatment improve the stability of aqueous dispersion of nanomaterials. The efficiency of surfactant aided dispersion depends strongly on the contents of CNTs and the ratio of the surfactant to CNTs. The commonly used polycarboxylate-based superplasticizer (water-reducing agent) as a dispersion agent in the study of cement nanocomposite is considered to be a surfactant attaching process, which shows a great compatibility to the host matrix and is low in cost.

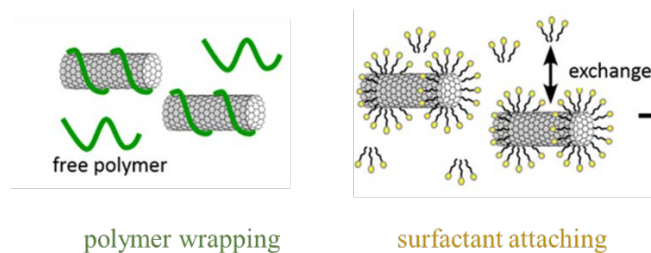


Figure 2.2 Schematic of noncovalent functionalization of CNTs

Noncovalent method is a generally simple procedure, compared to covalent method, which only achieved by the mixing of CNTs with molecules under a shear force treatment such as sonication. The drawback of noncovalent method, especially surfactant attaching treatment, is not as stable as covalent method.

2.2.2 Mechanical agitation

Conventional shear mixing used for cement material couldn't provide enough shear energy to break the CNT agglomerations. So several mechanical agitation were used in different studies to provide large shear forces in order to mechanically separate CNTs from each other.

Sonication: high-energy sonication is the most commonly used mechanical agitation to uniformly disperse the carbon nanomaterials in a solution. In the laboratory, it is usually achieved using an ultrasonication tip or ultrasonication bath[5]. The ultrasonication tip can generate larger energies with smaller frequencies, showing better effect on the dispersion of CNTs than the ultrasonication bath. The diameter of the probes needs to be determined by the quantity of dispersion products. Dispersion through ultrasonications are the results of ultrasonic cavitation. The high-energy energy is passed through the medium and produces attenuated sound waves. These sound waves form ultrasonic cavitation in liquids, which causes high speed liquid jets and it applies mechanical stress on the attracting forces between the individual particles (shown in Fig 2.3). This technique is only used for low viscous liquid, such as water, acetone and ethanol, so CNTs has to be dissolved or diluted with a solvent first rather than dispersed within cement directly. Sonication techniques are reported shortens CNTs and introduce defects at sidewalls if the agitation is too aggressive and/or too long[11]. A study finds lower sonication energy with longer sonication time proves better results than high sonication energy with shorter sonication time when ultrasonication energy is used to disperse carboxylate functionalized CNTs[12]. The localized damage of CNTs reduce both the electrical and mechanical properties of the CNT/cement composites. Therefore it is essential to optimize the total amount of energy as well as the energy intensity when utilizing the sonication for CNT dispersion. Even though

most studies on CNT's dispersion remains in lab-scale, the ultrasonication technique could be up-scaled to production level, which could deliver 1000 watts of energy using the industrial system.



Figure 2.3 Sonication probe (photo courtesy from Sonics)

Ball milling: Ball milling is a grinding procedure where a powder mixture placed in the ball mill and subjected to high-energy collision from the balls. The schematic of ball milling technique is provided in Fig 2.4. The ball milling process can grind mixture particles to as small as 100 nm. It is usually used to disperse CNTs in metallic matrices, such as aluminum[13] or copper[14]. The technique is also used with CNT powder in the presence of dry ice in a planetary ball milling [15].

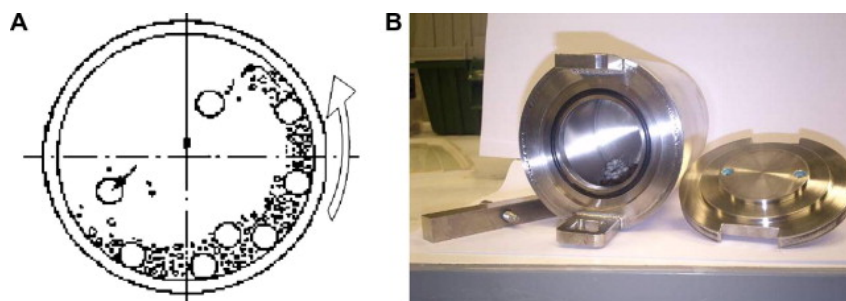


Figure 2.4 Schematics of ball milling technique (a) and container (b)

High-shear mixing: High-shear mixing is used to disperse fibers and a high content of CNTs within soluble polymers. Different from sonication technique, high-shear mixing could be used with high viscous material, such as asphalt (as seen in Fig. 2.5) at high CNT content. Though it has not been used to disperse CNT within cement, it potentially is a good choice for large quantity production of CNT reinforced cementitious material in industry.

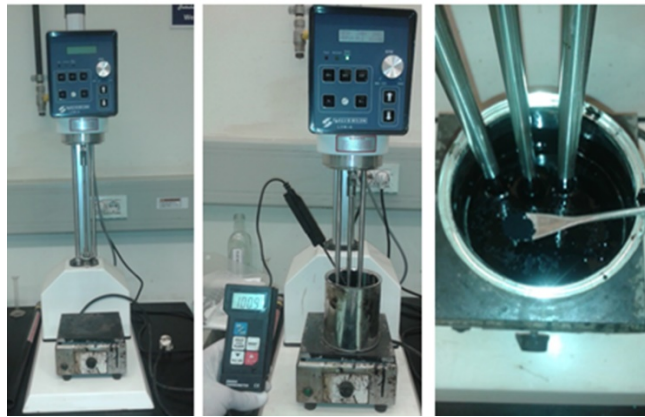


Figure 2.5 High-shear mixing of CNT and asphalt[16]

There are other mechanical agitation for CNT's dispersion, such as extrusion (for thermoplastics), calendaring (for liquid polymer). However it is not suitable for their application into cement composites. In addition, the damage to the tube itself can't be avoided with using mechanical agitation, and it should be minimized by optimizing the input parameters, such as total energy, intensity, during the treatment. The most commonly used dispersion method for CNTs is the combination of the use of ultra-sonication energy and superplasticizer for cement reinforcement. The dispersion process is achieved within aqueous solution and the dispersed suspension of CNTs will then be added into cement.

2.2.3 Evaluation of Dispersion Results

The efficiency of this dispersion process could be evaluated with different methods, such as ultraviolet-visible spectroscopy (UV-vis), and mechanical tests. The literature review of the evaluation methods are presented below.

2.2.3.1 Ultraviolet-visible Spectroscopy

Individual MWNT is active in the UV-vis region and it shows a single peak between 200 and 1200 nm, as shown in Fig 2.6[17]. Contrary to dispersed CNTs, bundle-form CNTs are not active within the wavelength mentioned above[18]. Therefore, UV-vis is a useful tool to monitor the exfoliation dynamic of CNTs in aqueous solution by relating the intensity of absorption at a specific wavelength to the concentration of suspend CNTs through the Beer-Lambert law. It can be used to investigate on input parameters of ultrasonication process, such as sonication energy, applied concentration of CNTs or ratio of CNTs to superplasticizer[19][20]. A study evaluates the optimum CNT to surfactant ratio for 0.1 wt% of CNTs dispersed with sodium dodecyl sulfate (SDS, a typical surfactant used for noncovalent dispersion)[19]. A “dynamic sonication curve” could be plotted by relating the absorbance at a certain wavelength to the corresponding input energy. Then the optimum input energy could be determined when the curve reaches its plateau. With the method, the study finds the minimum SDS to MWNT ratio of 1.5-1 is required to achieve fully dispersions, as presented in Fig 2.7[19]. Another study investigates the influence of calcium hydroxide ($\text{Ca}(\text{OH})_2$) to the dispersion solution using UV-vis technique, and it finds the $\text{Ca}(\text{OH})_2$ could reduce the dispersion degree and could potentially cause re-agglomeration of CNTs within cement pore structure. It should be noted that the UV-vis method is only valid for the evaluation of CNT’s dispersion within aqueous solution, and it cannot be used to evaluate the

final stage of CNTs within cement matrix. As mentioned above, a change of dispersion stage (re-agglomeration phenomenon) could happen and other characterization methods should be considered, such as imaging techniques and mechanical tests.

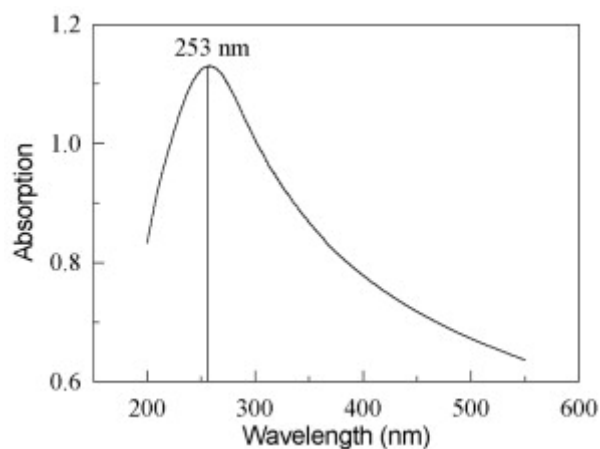


Figure 2.6 Typical UV-vis spectrum of CNTs in aqueous solution[17]

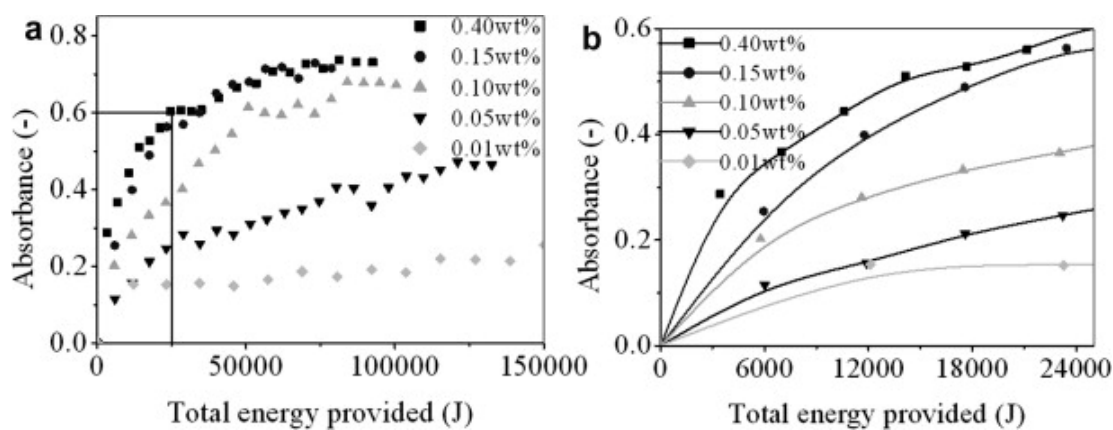


Figure 2.7 Evolution of the maximum absorbance of 0.1 wt% CNTs for different SDS concentrations[19]

2.2.3.2 Mechanical Tests

The mechanical tests of CNT added cement paste could be performed to evaluate the dispersion effect of dispersion. A flexural test has been performed with CNT/cement nanocomposite to determine the optimum surfactant to MWCNTs weight ratio for CNT's dispersion[21]. The study finds the flexural strength is directly related to the surfactant amount and at a weight ratio of 4:1 reveals the best mechanical property of the cement nanocomposite and thus gives the best dispersion effect. The flexural test could also evaluate the optimum sonication energy for the dispersion of 0.05 wt% CNFs (to weight cement), and it finds 2800 KJ/liter is sufficient yielding the highest flexural strength[22], as illustrated in Fig 2.8. With less amount of sonication energy, CNT agglomerations exist and create voids within the cement paste, diminishing the reinforcing effect of CNTs. On the other hand, excessive sonication energy could damage the structure of CNTs and shortens its length, which also gives a lower flexural strength compared to the optimum sonication energy.

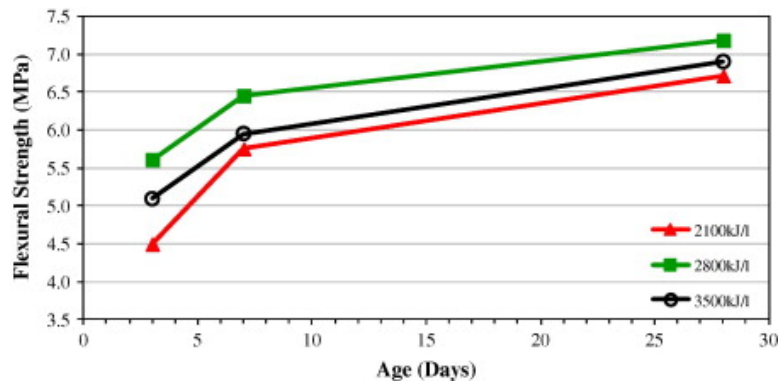


Figure 2.8 Effect of sonication energy on the flexural strength of cement paste reinforced with 0.048 wt% CNFs[22]

2.2.4 Re-agglomeration phenomenon within cement matrix

CNT's re-agglomeration issue has been reported in some studies due to the presence of alkaline environment within cement paste[23][24]. A possible explanation of this phenomenon is that the hydroxide ions react with the surfactant acid and influence its attachment to the tube surface. However, an addition of silica fume is found to be able to solve the issue in several studies[25][26][27]. The silica fume, as a generally added supplementary cement material, can consume the OH^- within pore solution. In addition, the small dimension of silica fume (about 200 nm particle size) relative to cement grains could facilitate the secondary dispersion of CNTs in cement matrix.

2.3 Research Work on CNT Reinforced Cementitious Materials

There is a quick expansion on the research with CNT reinforced cementitious materials in the last decade, probably due to the evolution of dispersion technique and the price drop of the nanomaterials. The first wisdom of dealing with nanoscale fibers comes from the addition of conventional microfibers where the typical addition is 2-5 wt% to cement weight. However the dispersion technique of using sonication energy and surfactant has a limitation on CNT's content and it can only disperse a small CNT dosage around 0.05-0.2 wt%. The research work on CNT reinforced cementitious materials could be categorized into following: mechanical properties, electrical properties, cement hydration, and shrinkage properties.

2.3.1 Mechanical properties

Due to the extraordinary mechanical properties and chemical stability, CNTs are acknowledged to be effective reinforcing composite materials including cement composites. Various mechanical properties has been evaluated for cement paste, mortar and concrete with

incorporation of CNTs, such as tensile strength[28][29][30], compressive strength[26][30][31], flexural strength[21], flexural toughness[7][32][33][34], fracture energy[34], Young's modulus[35][36], and ductility[37]. Among these studies, the most effective dosages of CNT are between 0.05-0.2 wt% to cement weight, which is mostly due to the efficiency of the dispersion treatment. A recent study with MWCNTs added cement mortar observes an improvement of 118% in flexural strength, 124% in Young's modulus and 103% in flexural toughness[38], where the ultra-sonication and surfactant are used for dispersion. The author also compares the improvement between cement paste, mortar and concrete with the addition of 0.1 wt% CNT. And it finds the enhancement on flexural strength and Young's modulus is more significant in mortar compared to cement paste (see Fig. 2.9), indicating a potential modification on the interfacial transitional zone (ITZ) between paste and aggregate[36].

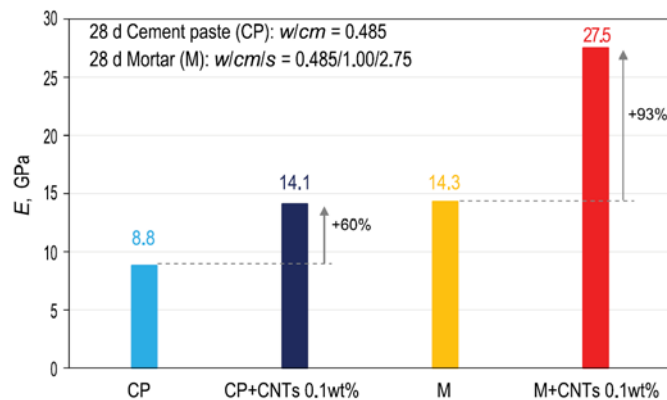


Figure 2.9 Modulus of elasticity E for cement paste and mortar with 0.1 wt% CNTs[36]

Four mechanisms are proposed with respect to the reinforcing effect on mechanical properties[39]: 1. CNTs can act as nucleating sites for cement hydration and changes the hydration products within cement matrix; 2. CNTs has bridging effect within micro-cracks, which increase fracture properties; 3. CNTs modifies the microstructure of cement matrix; 4.

CNTs fill in fine pores and alter the pore structure. However, these theories need further examination in nanoscale.

2.3.2 Electrical properties

Cement-based materials generally have low electrical conductivity and no self-sensing behavior. With incorporation of carbon nanomaterials within a certain dosage, the electrical properties will be enhanced dramatically. An electrical resistance test has been formed with CNTs and CNFs at an amount of 0.1 wt% and 0.3 wt% to cement weight [40]. With increasing amount of dispersed CNT within cement matrix, the electrical resistance decreases, increasing the electrical property of the cement composite. Then the piezoresistive behavior of the cement nanocomposite is evaluated under cyclic compressive loading, as illustrated in Fig 2.10.

Research on the electrical properties of CNT reinforced cement materials proves that CNT could greatly improve the electrical conductivity of the nanocomposite, transforming the material into self-sensing smart material under compression [41][42][43].

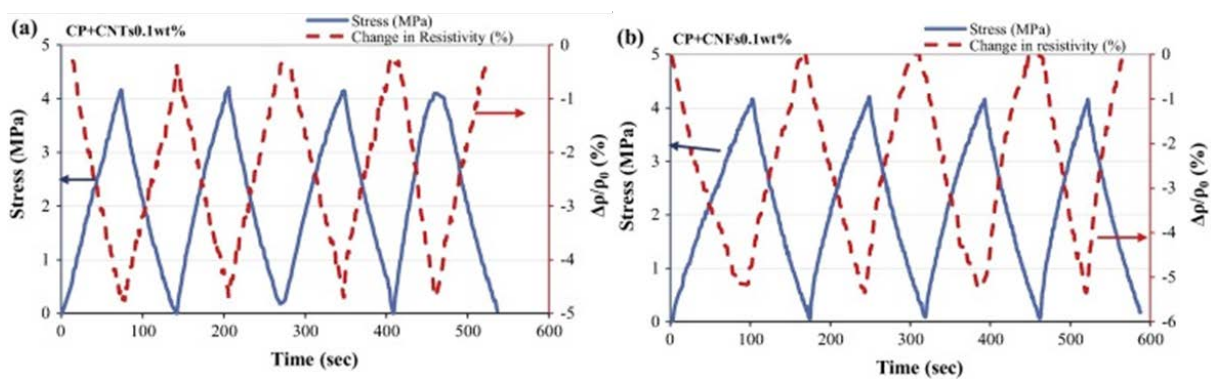


Figure 2.10 Piezoresistive behavior of cement composites with 0.1 wt% of CNT or CNF [40]

2.3.3 Durability

Durability is also evaluated for CNT added cementitious composites, such as autogenous shrinkage and reinforcement corrosion.

Autogenous Shrinkage: Autogenous shrinkage is known to be a serious issue in high performance concrete where water/cement ratio is low. The beneficial effect by incorporation of CNTs in cement composite is seen on autogenous shrinkage. A study has investigated the effect of CNTs or CNFs on autogenous shrinkage of cement paste at the dosage varying from 0.005 to 0.1 wt% to cement weight. It finds a significant reduction due to the addition of nanomaterials in most dosages in the first 7 hours after mixing [44]. The possible mechanism of CNT's effect on autogenous shrinkage given by the author is that the addition of CNT densify the structure of cement matrix and also provide a better interconnection between hydration products formed at the early stage. A similar effect has been seen in another study where 0.025 and 0.048 wt% of CNTs were added into cement paste and a 40 % reduction on autogenous shrinkage has been seen for the higher dosage[45], as seen in Fig. 2.11. A nano-indentation test has also been performed proving that high stiffness calcium-silicate-hydrate (C-S-H) increases by incorporation of CNTs (see Fig. 2.11).

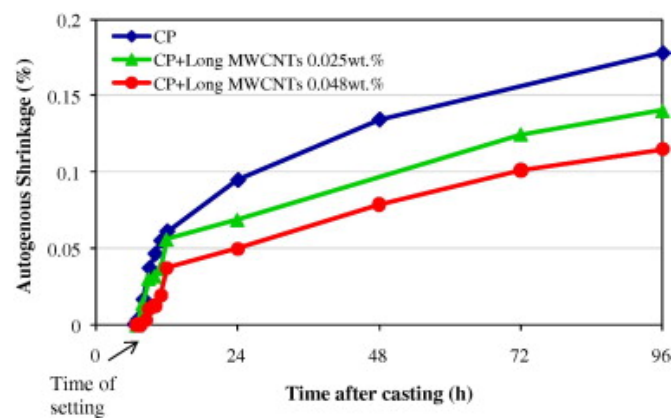


Figure 2.11 Autogenous shrinkage of cement paste with 0.025 or 0.048 wt% of CNT[45]

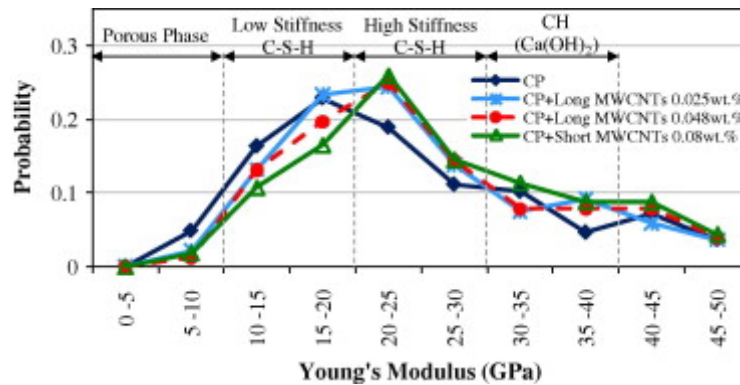


Figure 2.12 Probability plots of the Young's modulus of cement paste with CNTs[45]

Reinforcement Corrosion

Corrosion of steel in concrete is a major contributor to degradation of concrete. Since the addition of CNT increase the electrical conductivity of cementitious materials as mentioned above, there is concern about the increase in galvanic activity and its impact on steel reinforcement corrosion. However, since CNT is believed to densify the microstructure of the cement matrix by reducing the fine pores, chloride ion intrusion could be arrested which would greatly improve corrosion behavior[46][47]. A study has conducted a corrosion test on CNT added cement mortar and it shows a great improvement on corrosion prohibiting with 0.1 wt% CNTs or CNFs, which is shown in Fig 2.13[48].

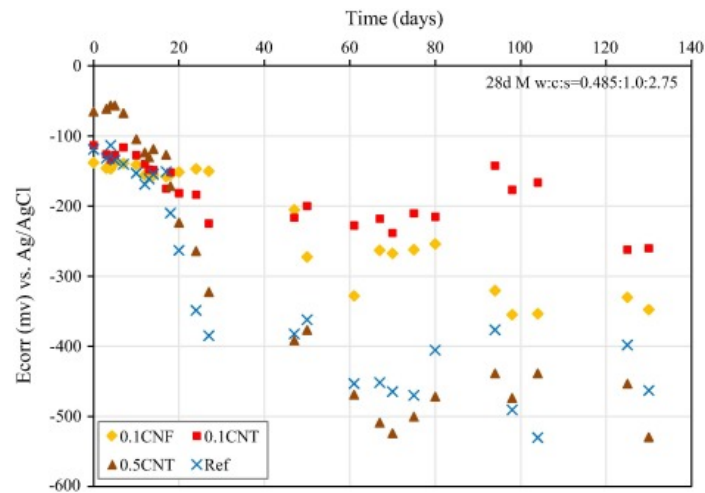


Figure 2.13 Half-cell potential versus time for CNT or CNF reinforced cement mortars[48]

2.4 Motivation and Objectives of the Present Work

CNTs has been used in many composite materials to improve their performance and properties due to the great mechanical properties (tensile strength and Young's modulus). Though a wide variety of reinforcing fibers has been used in cement materials, their effect is more limited on controlling the size and distribution of macro cracks. The addition of CNTs are possibly the strongest and smallest reinforcing fibers that can be incorporated in cement composite to arrest micro-cracks and enhance the micro structure of the materials. Based on the previous research, CNTs are showing promising results on the improvement of cement-based materials on many different aspects. CNT has great effect on improving the mechanical properties, especially the unexpected development of Young's modulus on mortar compared to paste. The significant reduction on autogenous shrinkage due to CNTs enables great potential application in concrete materials and construction industry. The objective of the present work will focus on investigations of the nanoparticle dispersion optimization, nanostructure of OPC and C-S-H. The research will also evaluate material-scale structural properties with CNT added concrete samples.

References

- [1] M. Abdalla, D. Dean, D. Adibempe, E. Nyairo, P. Robinson, G. Thompson, The effect of interfacial chemistry on molecular mobility and morphology of multiwalled carbon nanotubes epoxy nanocomposite, *Polymer (Guildf)*. 48 (2007) 5662–5670.
doi:<https://doi.org/10.1016/j.polymer.2007.06.073>.
- [2] R. Atif, F. Inam, Reasons and remedies for the agglomeration of multilayered graphene and carbon nanotubes in polymers, *Beilstein J. Nanotechnol.* 7 (2016) 1174–1196.
doi:[10.3762/bjnano.7.109](https://doi.org/10.3762/bjnano.7.109).
- [3] J. Liu, A.G. Rinzler, H. Dai, J.H. Hafner, R.K. Bradley, P.J. Boul, A. Lu, T. Iverson, K. Shelimov, C.B. Huffman, F. Rodriguez-Macias, Y.-S. Shon, T.R. Lee, D.T. Colbert, R.E. Smalley, Fullerene Pipes, *Science (80-.)*. 280 (1998) 1253–1256.
doi:[10.1126/science.280.5367.1253](https://doi.org/10.1126/science.280.5367.1253).
- [4] V. Likodimos, T.A. Steriotis, S.K. Papageorgiou, G.E. Romanos, R.R.N. Marques, R.P. Rocha, J.L. Faria, M.F.R. Pereira, J.L. Figueiredo, A.M.T. Silva, P. Falaras, Controlled surface functionalization of multiwall carbon nanotubes by HNO₃ hydrothermal oxidation, *Carbon N. Y.* 69 (2014) 311–326.
doi:<https://doi.org/10.1016/j.carbon.2013.12.030>.
- [5] P.-C. Ma, N.A. Siddiqui, G. Marom, J.-K. Kim, Dispersion and functionalization of carbon nanotubes for polymer-based nanocomposites: A review, *Compos. Part A Appl. Sci. Manuf.* 41 (2010) 1345–1367. doi:<https://doi.org/10.1016/j.compositesa.2010.07.003>.

- [6] G.Y. Li, P.M. Wang, X. Zhao, Mechanical behavior and microstructure of cement composites incorporating surface-treated multi-walled carbon nanotubes, *Carbon N. Y.* 43 (2005) 1239–1245. doi:<https://doi.org/10.1016/j.carbon.2004.12.017>.
- [7] A.A.-R.R. K., T.B. M., Y. Ardavan, G. Zachary, Mechanical Properties of Nanocomposite Cement Incorporating Surface-Treated and Untreated Carbon Nanotubes and Carbon Nanofibers, *J. Nanomechanics Micromechanics*. 2 (2012) 1–6. doi:10.1061/(ASCE)NM.2153-5477.0000041.
- [8] D.E. Hill, Y. Lin, A.M. Rao, L.F. Allard, Y.-P. Sun, Functionalization of Carbon Nanotubes with Polystyrene, *Macromolecules*. 35 (2002) 9466–9471. doi:10.1021/ma020855r.
- [9] B. Mc Carthy, J.N. Coleman, R. Czerw, A.B. Dalton, D.L. Carroll, W.J. Blau, Microscopy studies of nanotube-conjugated polymer interactions, *Synth. Met.* 121 (2001) 1225–1226. doi:[https://doi.org/10.1016/S0379-6779\(00\)00906-1](https://doi.org/10.1016/S0379-6779(00)00906-1).
- [10] L. Vaisman, H.D. Wagner, G. Marom, The role of surfactants in dispersion of carbon nanotubes, *Adv. Colloid Interface Sci.* 128–130 (2006) 37–46. doi:<https://doi.org/10.1016/j.cis.2006.11.007>.
- [11] J. Rausch, R.-C. Zhuang, E. Mäder, Surfactant assisted dispersion of functionalized multi-walled carbon nanotubes in aqueous media, *Compos. Part A Appl. Sci. Manuf.* 41 (2010) 1038–1046. doi:<https://doi.org/10.1016/j.compositesa.2010.03.007>.
- [12] L. Coelho, jaqueline suave, S. Pezzin, S. Amico, Effect of sonication on thermo-mechanical properties of epoxy nanocomposites with carboxylated-SWNT, 2009.

doi:10.1016/j.msea.2009.01.036.

- [13] A. Esawi, K. Morsi, Dispersion of carbon nanotubes (CNTs) in aluminum powder, *Compos. Part A Appl. Sci. Manuf.* 38 (2007) 646–650.
doi:<https://doi.org/10.1016/j.compositesa.2006.04.006>.
- [14] S.J. Yoo, S.H. Han, W.J. Kim, A combination of ball milling and high-ratio differential speed rolling for synthesizing carbon nanotube/copper composites, *Carbon N. Y.* 61 (2013) 487–500. doi:<https://doi.org/10.1016/j.carbon.2013.04.105>.
- [15] J.H. Lee, B.G. Lee, Experimental and mechanical analysis of cement–nanotube nanocomposites, *Bull. Mater. Sci.* 40 (2017) 819–829. doi:10.1007/s12034-017-1431-z.
- [16] I. Amin, S.M. El-Badawy, T. Breakah, M.H.Z. Ibrahim, Effect of Functionalization and Mixing Process on the Rheological Properties of Asphalt Modified with Carbon Nanotubes, *Am. J. Civ. Eng. Archit.* 4 (2016) 90–97. doi:10.12691/ajcea-4-3-4.
- [17] L. Jiang, L. Gao, J. Sun, Production of aqueous colloidal dispersions of carbon nanotubes, *J. Colloid Interface Sci.* 260 (2003) 89–94. doi:[https://doi.org/10.1016/S0021-9797\(02\)00176-5](https://doi.org/10.1016/S0021-9797(02)00176-5).
- [18] N. Grossiord, O. Regev, J. Loos, J. Meuldijk, C.E. Koning, Time-Dependent Study of the Exfoliation Process of Carbon Nanotubes in Aqueous Dispersions by Using UV–Visible Spectroscopy, *Anal. Chem.* 77 (2005) 5135–5139. doi:10.1021/ac050358j.
- [19] J. Yu, N. Grossiord, C.E. Koning, J. Loos, Controlling the dispersion of multi-wall carbon nanotubes in aqueous surfactant solution, *Carbon N. Y.* 45 (2007) 618–623.

- doi:10.1016/j.carbon.2006.10.010.
- [20] R. Rastogi, R. Kaushal, S.K. Tripathi, A.L. Sharma, I. Kaur, L.M. Bharadwaj, Comparative study of carbon nanotube dispersion using surfactants, *J. Colloid Interface Sci.* 328 (2008) 421–428. doi:10.1016/j.jcis.2008.09.015.
- [21] M.S. Konsta-Gdoutos, Z.S. Metaxa, S.P. Shah, Highly dispersed carbon nanotube reinforced cement based materials, *Cem. Concr. Res.* 40 (2010) 1052–1059. doi:<https://doi.org/10.1016/j.cemconres.2010.02.015>.
- [22] Z.S. Metaxa, M.S. Konsta-Gdoutos, S.P. Shah, Carbon nanofiber cementitious composites: Effect of debulking procedure on dispersion and reinforcing efficiency, in: *Cem. Concr. Compos.*, 2013. doi:10.1016/j.cemconcomp.2012.10.009.
- [23] A. Yazdanbakhsh, Z. Grasley, B. Tyson, R. Abu Al-Rub, Distribution of Carbon Nanofibers and Nanotubes in Cementitious Composites, *Transp. Res. Rec. J. Transp. Res. Board.* 2142 (2010) 89–95. doi:10.3141/2142-13.
- [24] O. Mendoza, G. Sierra, J.I. Tobón, Influence of super plasticizer and Ca(OH)₂ on the stability of functionalized multi-walled carbon nanotubes dispersions for cement composites applications, *Constr. Build. Mater.* 47 (2013) 771–778. doi:<https://doi.org/10.1016/j.conbuildmat.2013.05.100>.
- [25] Y. Ardavan, G. Zachary, Utilization of Silica Fume to Stabilize the Dispersion of Carbon Nanofilaments in Cement Paste, *J. Mater. Civ. Eng.* 26 (2014) 6014010. doi:10.1061/(ASCE)MT.1943-5533.0001016.

- [26] H.K. Kim, I.W. Nam, H.K. Lee, Enhanced effect of carbon nanotube on mechanical and electrical properties of cement composites by incorporation of silica fume, *Compos. Struct.* 107 (2014) 60–69. doi:10.1016/j.compstruct.2013.07.042.
- [27] S. Alrekabi, A. Cundy, R.L.D. Whitby, A. Lampropoulos, I. Savina, Effect of Undensified Silica Fume on the Dispersion of Carbon Nanotubes within a Cementitious Composite, *J. Phys. Conf. Ser.* 829 (2017) 12011. <http://stacks.iop.org/1742-6596/829/i=1/a=012011>.
- [28] F. Collins, J. Lambert, W.H. Duan, The influences of admixtures on the dispersion, workability, and strength of carbon nanotube-OPC paste mixtures, *Cem. Concr. Compos.* 34 (2012) 201–207. doi:10.1016/j.cemconcomp.2011.09.013.
- [29] S.S.-H. Gillani, A. Khitab, S. Ahmad, R.A. Khushnood, G.A. Ferro, S.M. Saleem Kazmi, L.A. Qureshi, L. Restuccia, Improving the mechanical performance of cement composites by carbon nanotubes addition, *Procedia Struct. Integr.* 3 (2017) 11–17. doi:<https://doi.org/10.1016/j.prostr.2017.04.003>.
- [30] S.-H. Jang, S. Kawashima, H. Yin, Influence of Carbon Nanotube Clustering on Mechanical and Electrical Properties of Cement Pastes, *Materials (Basel)*. 9 (2016) 220. doi:10.3390/ma9040220.
- [31] A. Sobolkina, V. Mechtcherine, V. Khavrus, D. Maier, M. Mende, M. Ritschel, A. Leonhardt, Dispersion of carbon nanotubes and its influence on the mechanical properties of the cement matrix, *Cem. Concr. Compos.* 34 (2012) 1104–1113. doi:<https://doi.org/10.1016/j.cemconcomp.2012.07.008>.
- [32] P.A. Danoglidis, M.S. Konsta-Gdoutos, E.E. Gdoutos, S.P. Shah, Strength, energy

- absorption capability and self-sensing properties of multifunctional carbon nanotube reinforced mortars, *Constr. Build. Mater.* 120 (2016) 265–274.
doi:10.1016/j.conbuildmat.2016.05.049.
- [33] E.E. Gdoutos, M.S. Konsta-Gdoutos, P.A. Danoglidis, Portland cement mortar nanocomposites at low carbon nanotube and carbon nanofiber content: A fracture mechanics experimental study, *Cem. Concr. Compos.* 70 (2016) 110–118.
doi:10.1016/j.cemconcomp.2016.03.010.
- [34] Y. Hu, D. Luo, P. Li, Q. Li, G. Sun, Fracture toughness enhancement of cement paste with multi-walled carbon nanotubes, *Constr. Build. Mater.* 70 (2014) 332–338.
doi:<https://doi.org/10.1016/j.conbuildmat.2014.07.077>.
- [35] R.K. Abu Al-Rub, A.I. Ashour, B.M. Tyson, On the aspect ratio effect of multi-walled carbon nanotube reinforcements on the mechanical properties of cementitious nanocomposites, *Constr. Build. Mater.* 35 (2012) 647–655.
doi:10.1016/j.conbuildmat.2012.04.086.
- [36] M.S.K.-G. Surendra P. Shah, Uncoupling Modulus of Elasticity and Strength, *Concr. Int.* 39 (2017) 37–42.
- [37] J. Lin Luo, Z. Dong Duan, T. Jun Zhao, Q. Yi Li, Effect of Multi-Wall Carbon Nanotube on Fracture Mechanical Property of Cement-Based Composite, 2010.
doi:10.4028/www.scientific.net/AMR.146-147.581.
- [38] M.S. Konsta-Gdoutos, P.A. Danoglidis, M.G. Falara, S.F. Nitodas, Fresh and mechanical properties, and strain sensing of nanomodified cement mortars: The effects of MWCNT

- aspect ratio, density and functionalization, *Cem. Concr. Compos.* 82 (2017) 137–151.
doi:<https://doi.org/10.1016/j.cemconcomp.2017.05.004>.
- [39] Carbon nanotube reinforced cementitious composites: An overview, *Compos. Part A Appl. Sci. Manuf.* (2016). <http://dx.doi.org/10.1016/j.compositesa.2016.10.020>.
- [40] M.S. Konsta-Gdoutos, C.A. Aza, Self sensing carbon nanotube (CNT) and nanofiber (CNF) cementitious composites for real time damage assessment in smart structures, *Cem. Concr. Compos.* 53 (2014) 162–169.
doi:<https://doi.org/10.1016/j.cemconcomp.2014.07.003>.
- [41] G.Y. Li, P.M. Wang, X. Zhao, Pressure-sensitive properties and microstructure of carbon nanotube reinforced cement composites, *Cem. Concr. Compos.* 29 (2007) 377–382.
doi:<https://doi.org/10.1016/j.cemconcomp.2006.12.011>.
- [42] F. Azhari, N. Banthia, Cement-based sensors with carbon fibers and carbon nanotubes for piezoresistive sensing, *Cem. Concr. Compos.* 34 (2012) 866–873.
doi:<https://doi.org/10.1016/j.cemconcomp.2012.04.007>.
- [43] H.K. Kim, I.S. Park, H.K. Lee, Improved piezoresistive sensitivity and stability of CNT/cement mortar composites with low water–binder ratio, *Compos. Struct.* 116 (2014) 713–719. doi:<https://doi.org/10.1016/j.compstruct.2014.06.007>.
- [44] F. Blandine, K. Habermehi-Cwirzen, A. Cwirzen, Contribution of CNTs/CNFs morphology to reduction of autogenous shrinkage of Portland cement paste, *Front. Struct. Civ. Eng.* 10 (2016) 224–235. doi:[10.1007/s11709-016-0331-4](https://doi.org/10.1007/s11709-016-0331-4).

- [45] M.S. Konsta-Gdoutos, Z.S. Metaxa, S.P. Shah, Multi-scale mechanical and fracture characteristics and early-age strain capacity of high performance carbon nanotube/cement nanocomposites, *Cem. Concr. Compos.* 32 (2010) 110–115.
doi:10.1016/j.cemconcomp.2009.10.007.
- [46] T. Nochaiya, A. Chaipanich, Behavior of multi-walled carbon nanotubes on the porosity and microstructure of cement-based materials, *Appl. Surf. Sci.* 257 (2011) 1941–1945.
doi:<https://doi.org/10.1016/j.apsusc.2010.09.030>.
- [47] B. Han, Z. Yang, X. Shi, X. Yu, Transport Properties of Carbon-Nanotube/Cement Composites, *J. Mater. Eng. Perform.* 22 (2013) 184–189. doi:10.1007/s11665-012-0228-x.
- [48] M. Konsta, G. Batis, P. Danoglidis, A. K. Zacharopoulou, E. K. Zacharopoulou, M. Falara, S. Shah, Effect of CNT and CNF loading and count on the corrosion resistance, conductivity and mechanical properties of nanomodified OPC mortars, 2017.
doi:10.1016/j.conbuildmat.2017.04.112.

Chapter 3

Experimental Work with CNT Reinforced Cementitious Material at Macro Scale

3.1 Introduction

Based on previous study with CNT reinforced cement paste at Northwestern University (NU), it has been proven that the fiber-shaped carbon nanomaterial can improve the mechanical properties of the cement paste on its flexural strength and modulus of elasticity (MOE). The study continues in this thesis and upscaled to mortar and concrete, which is the most used construction material around the world. With the patented dispersion method at NU, CNF is well dispersed and added in cement paste, mortar and concrete, then the mechanical properties, autogenous shrinkage and shrinkage cracking are tested in macro-scale. Both mechanical test and autogenous shrinkage test finds a more obvious effect in mortar than in paste, where interfacial transitional zone (ITZ) is potentially enhanced in nanoscale. In addition, the uncoupling effect of

MOE and compressive strength is particularly interesting due to the addition of well-dispersed CNFs. Higher MOE is becoming quite critical for the design of high-rise buildings, which determines its lateral movement under lateral forces. The MOE can be increased by increasing the compressive strength based on their direct relationship ($E = 57000\sqrt{f'c}$). However, the higher compressive strength always increases the cost during construction, though it is far beyond the design requirement. The uncoupling effect of CNT in concrete material could be a promising alternative to achieve the higher requirement of MOE.

3.2 Dispersion Method

The dispersion method used in this dissertation is a combination of the use of non-covalent chemical agitation and the ultrasonication energy. The dispersed suspension is then characterized under ultraviolet-visible spectroscopy (UV-Vis). The complete process is demonstrated in Fig 3.1. The water added in the CNT suspension is the bulk water in cement mixture, and no extra water is needed during concrete mixing. The agent used for non-covalent chemical agitation is a polycarboxylated superplasticizer (SP), which is a commonly used high-range water-reducing agent for concrete material. The polycarboxylated SP is composed of a methoxy-polyethylene glycol copolymer side chain grafted with methacrylic acid copolymer main chain. The number and the length of side chains are flexible parameters and can be easily manipulated for different SP products. Basically, the SP is a comb-shaped polymer, where the backbone is negatively charged, and the side chains are uncharged but rather hydrophilic. The mechanism of the dispersion effect for CNTs is that SPs are physically adsorbed on CNT surfaces, creating electrostatic repulsion to overcome the Van der Waals forces. The ratio of SP to CNT is 4:1, and it is added in aqueous solution before applying the sonication energy. The sonication energy is

delivered via a sonication tip with a total amount of 2800 KJ/L at a rate frequency of 50J/s. The sonication process is applied in cycles of 20 s to prevent overheating. A high temperature should be prevented which could hinder the effect of dispersion. The equipment is shown in Fig 3.2.

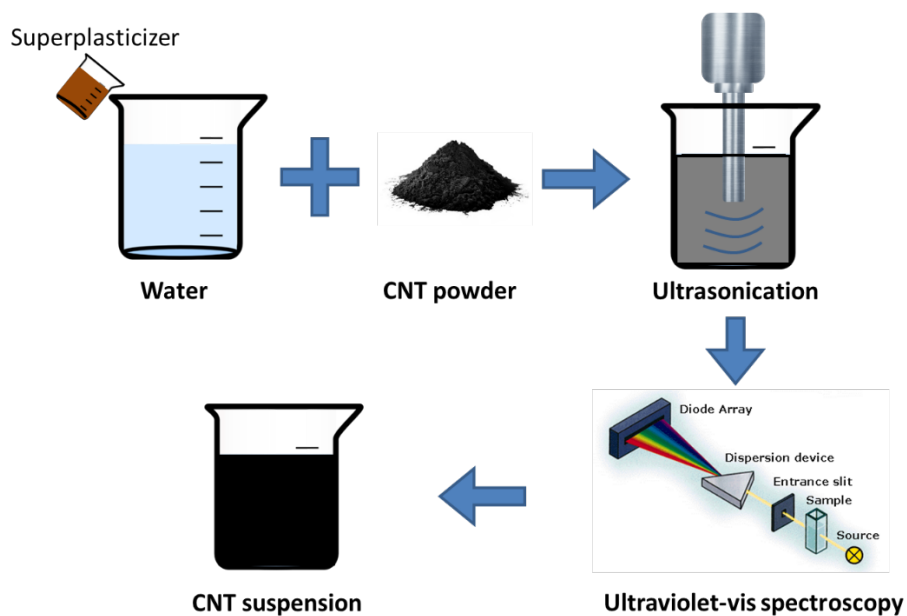


Figure 3.1 Schematic diagram of dispersion process



Figure 3.2 Sonication tip

The UV-Vis spectroscopy is employed as an evaluation method of dispersion effect. As mentioned in Chapter 2, only individual CNT is active within 200-800 nm wavelength, while bundled CNTs are hardly active within the same range wavelength, probably because carriers are tunneling between the nanotubes and thus their photoluminescence would be quenched. Based on this principle, UV-Vis intensity can be correlated to the concentration of well-dispersed CNTs within the aqueous solution. The suspension is diluted 100 times, and the absorbance of SP is subtracted from the absorbance of CNT suspensions.

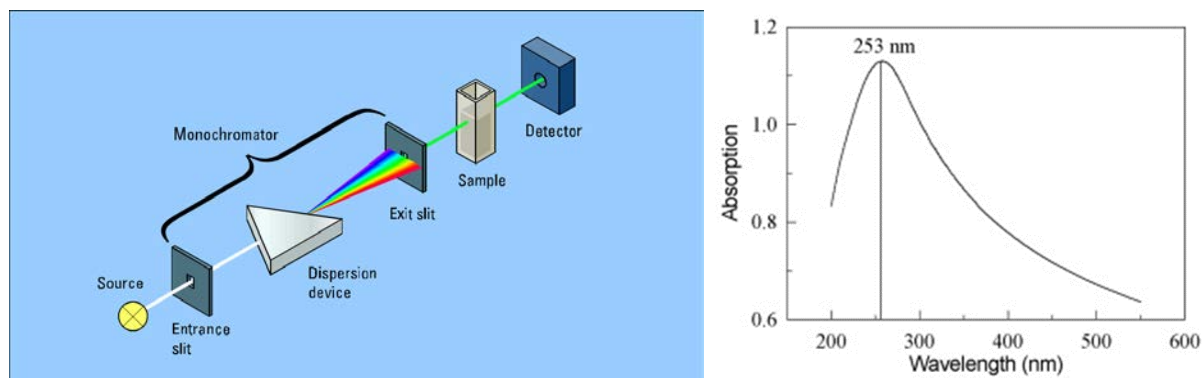


Figure 3.3 Schematic diagram of UV-Vis spectroscopy and an example of CNT's spectrum

A small amount of sample is taken every hour during the dispersion process, and the absorbances are measured using UV-Vis. The peak absorbances value from each absorbance curve are extracted and plotted with the corresponding input energy. The dynamic dispersion process could be monitored with the Energy-Peak Absorbance curve. The peak absorbance is increasing with the input energy, meaning the amount of individual CNTs is increasing in the suspension. Then the peak absorbance reaches a plateau and the amount of individual CNTs can't be further developed. The corresponding input energy would be the optimum ultrasonication energy for the dispersion. The method can be used to evaluate the optimum energy and the efficiency of the SP, however it is not suitable to quantify the dispersion effect of different CNT concentrations.

To compare the dispersion effect between different CNT concentrations, a calibration curve should be constructed. UV-Vis spectrums of CNT suspensions with small concentrations are needed, where a full dispersion can be obtained easily. Then peak absorbances could be plotted with CNT concentrations, and a linear regression could be drawn to predict a peak absorbance for higher concentrations.

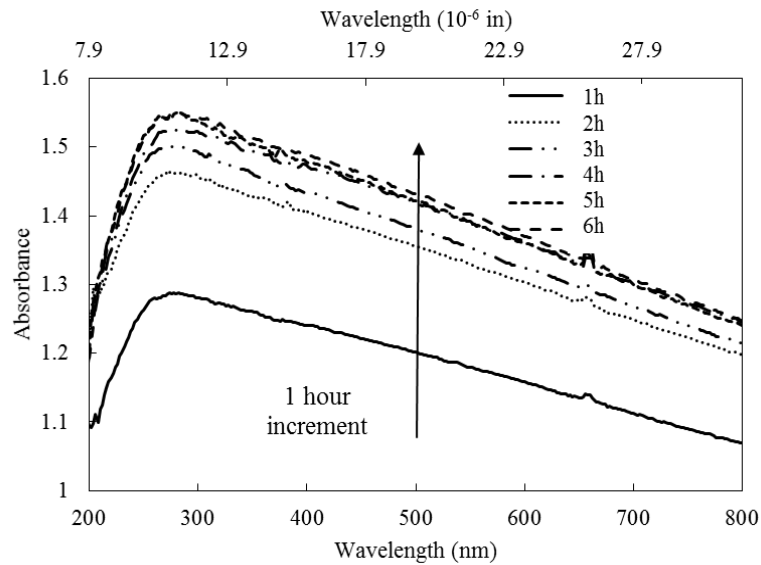


Figure 3.4 Absorbance of samples with different ultrasonication time

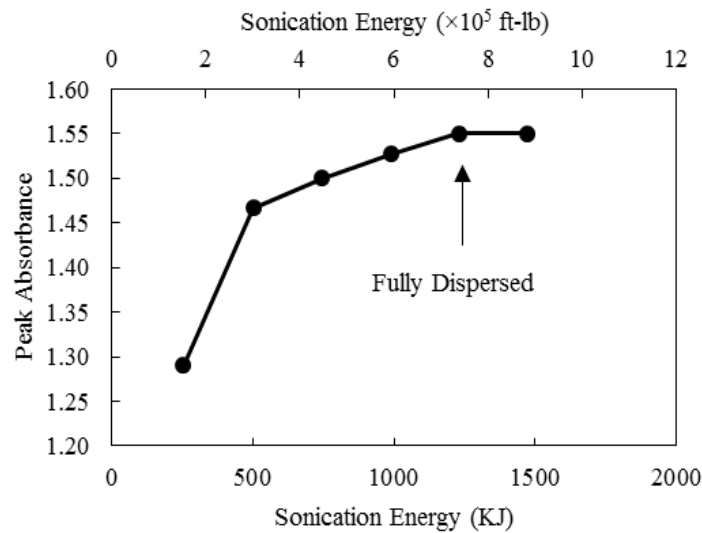


Figure 3.5 Peak absorbance Vs. Sonication energy

3.3 Materials

The cementitious material used in this thesis is type I Ordinary Portland Cement with a chemical composition shown in Table 3.1. The sand is commercially available river sand. The coarse aggregate added in concrete samples is locally available crushed limestone with a grading shown

in Fig. 3.6. The CNF used in the study is a vapor-grown, highly graphitic carbon nanofiber, produced by Pyrograf Products with a product number PR-24-XR-PS. The fiber has an average diameter of about 150 nm and exhibits a minimal chemical vapor deposited (CVD) layer of carbon on its surface. Detailed properties are shown in Table 3.2. The fiber is cone shaped graphene with graphite planes canted with respect to the longitudinal fiber axis. The stick-out planes may facilitate the bonding between the fiber and the substrate material. The morphology of individual CNF is shown in Fig 3.7.

Table 3.1 Chemical composition of cement

Oxide	% by weight
SiO ₂	21.1
Al ₂ O ₃	3.9
Fe ₂ O ₃	3.2
CaO	65.7
SO ₃	3.5
MgO	0.9

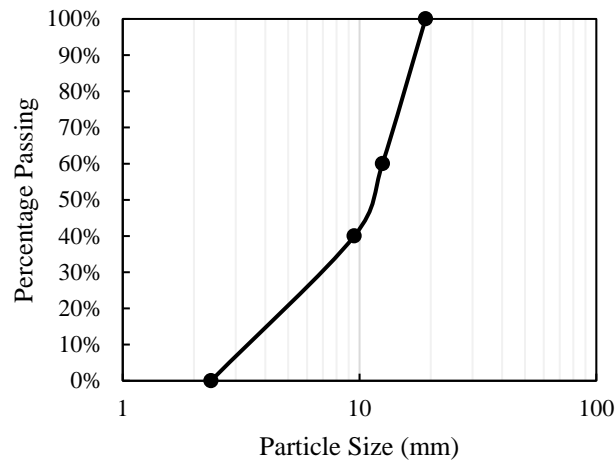


Figure 3.6. Grading of coarse aggregate

Table 3.2 Carbon nanofiber properties

Carbon Purity, wt%	98
Average Diameter, nm	150
Fiber Length, μm	50—200
Bulk Density, g/cm^3	0.03
Iron Content, ppm	11,096
Aspect Ratio	~670
Specific Surface Area, m^2/g	20—30
Modulus of Elasticity, GPa	200-600

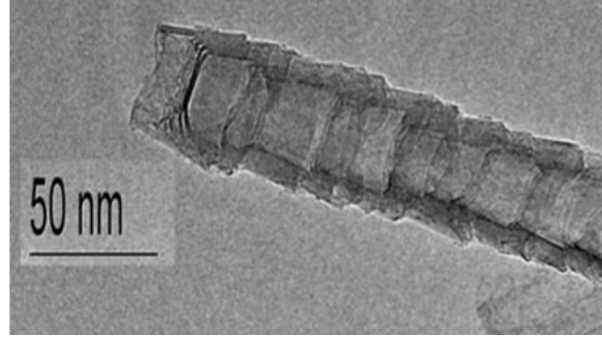


Figure 3.7 Higher Resolution Image of Carbon Nanofiber from Pyrograf Products

3.4 Mechanical Properties

3.4.1 Three-point Bending Test

The three-point bending test is performed on beam samples of cement paste ($w/c=0.485$) and mortar ($w/c=0.485$, $s/c=2.75$), which has a dimension of $2\text{ cm} \times 2\text{ cm} \times 8\text{ cm}$. A 6 mm notch is cut in the middle of each sample from the bottom, where an extensometer is attached under it to record the crack mouth opening displacement (CMOD). The test set-up is shown in Fig. 3.8.

Four samples of each specimen are tested in three-point bending at the age of 3, 7 and 28 days, and average values are taken for each age. A closed-loop MTS servo-hydraulic testing machine is used to perform the CMOD-controlled test. The MOE is calculated based on the load-CMOD data, using the two-parameter fracture model by Jenq and Shah [1].

The flexural stress is calculated by:

$$\sigma_f = \frac{3FL}{2t(d-a_0)^2} \quad (1)$$

where L , t , d , and a_0 are specimens' dimensions showing in Fig. 3.8.

The MOE is calculated by:

$$E = \frac{6Sa_0g_2(a_0)}{C_i b^2 t} \quad (2)$$

Where a , S , b , t are specimens' dimensions, C_i = the compliance of the loading portion of the load-CMOD curve; $g_2(a_0)$ = geometric function defined by:

$$g_2(a_0) = 0.76 - 2.28a_0 + 3.87a_0^2 - 2.04a_0^3 + \frac{0.66}{(1-a_0)^2} \quad (3)$$

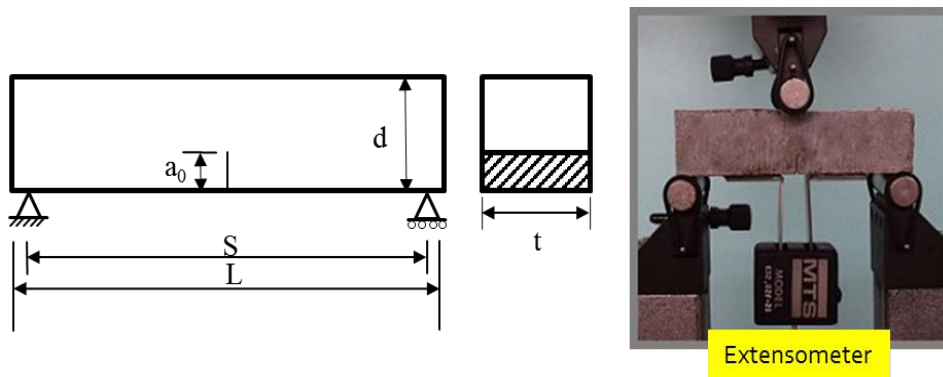


Figure 3.8 Set-up of flexural test

3.4.2 Compression Test

The compression test is performed on concrete cylinder specimens of 10 cm × 20 cm in dimension. The specimens are tested at 28 days after curing in humidity chamber (100% humidity, 23 °C) and capped with hydrostone prior to compression testing. The compression test follows ASTM C469[2], where a compressometer is used to measure the longitudinal strain under loading as shown in Figure 3.9. Three concrete specimens are prepared for each mix. The first cylinder is tested to failure and the compressive strength is calculated. Then the other two samples are compressed to 40% of their compressive strength with the recording of the compression strains by the compressometer. The MOE is then calculated for the two samples and average values are taken. Lastly, the two cylinders are tested to failure and compressive strength

is taken as the average values of three samples. The volume fraction of CNFs is calculated for cement paste, mortar and concrete specimen of mechanical tests based on the weight dosage (0.1 % to cement weight) and its density ($1.4 - 1.6 \text{ g/cm}^3$ according to the manufacture).

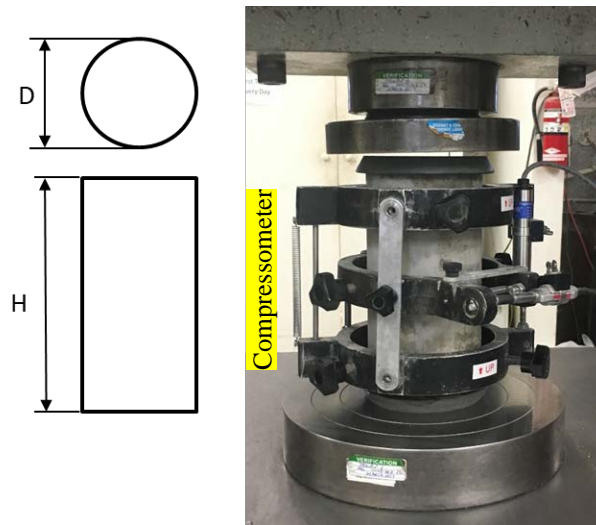


Figure 3.9 Set-up of compression test

3.5 Autogenous Shrinkage and Shrinkage Cracking

Shrinkage of concrete, as a volume reduction in cement binder, mainly includes autogenous shrinkage, drying shrinkage and thermal shrinkage that have different mechanisms. Autogenous shrinkage is caused by cement hydration after the formation of initial structure of the cement matrix and is most significant in the first 24 hours after mixing[3]. Unlike other forms of shrinkage, autogenous shrinkage does not involve any volume change due to substances ingression, temperature variation or application of external restraint. So, it is well accepted that the autogenous shrinkage is mainly driven by the capillary pressure, and is considered as self-desiccation shrinkage. Autogenous shrinkage is critical when water to cement (w/c) is low, and the internal moisture is insufficient to hydrate cement particles. For this reason, it is more

harmful to high and ultra-high performance concrete. The capillary tension theory is the most acknowledged to explain autogenous shrinkage mechanism. Free water decreases as the cement hydrating over time, and thus the internal relative humidity reduces. Pores are formed and the water in pores keeps reducing. Consequently, the pores are becoming unsaturated, where the inner surface of pores starts to be subjected to an internal pressure. To reach the state of equilibrium on the pore surfaces, the capillary tension develops and the autogenous shrinkage takes place.

Several strategies have been developed to mitigate the autogenous shrinkage by using shrinkage reducing agents, fibers, saturated lightweight aggregates (LWA), and superabsorbent polymers (SAP). Previous works find the addition of steel fibers in micro-scale can reduced the shrinkage of concrete because of the high elastic modulus strengthen the skeleton to resist the free shrinkage of concrete[4]. The incorporation of lightweight aggregates can absorb water, which increase the internal humidity and release water under the action of capillary tension[5]. SAP are new polymer materials with high water absorption. It improves the curing environment of concrete by releasing free water at low internal humidity like LWAs[6][7]. While these methods are effective lowering shrinkage strains, they have a limited ability to restrain the width of autogenous shrinkage cracks. Fiber reinforcement has proven beneficial in restraining shrinkage cracking, and CNT may have a potential effect by arresting crack initiation and coalescence at the nanometer scale[8][9].

3.5.1 Autogenous Shrinkage Measurement

Autogenous shrinkage measurements are performed on three different mixtures with the mix composition shown in Table 1. The same water to cement ratio of 0.4 and CNF dosage of 0.8 % per weight of cement is used for both pastes and mortars. Due to the addition of sand in mortar samples, the fiber amount as indicated in volume fraction in mortar sample is significantly less than in cement paste sample. Another mortar sample, indicated as high-performance mortar (HPM), has a lower w/c of 0.34 where the autogenous shrinkage is expected to be more severe. To compare the CNF's effect in regular mortar and high-performance mortar, CNF dosage is decreased to 0.05 % to cement weight thus the volume fraction is comparable.

Table 3.3 Mix composition for autogenous shrinkage test

Mix	w/c	s/c	CNF (wt%)	SP (wt%)	CNF Volume Fraction
Plain Paste	0.40	0	0	0.32	0
Paste+CNF	0.40	0	0.08	0.32	3.49×10^{10}
Plain Mortar	0.40	2.75	0	0.32	0
Mortar+CNF	0.40	2.75	0.08	0.32	1.41×10^{10}
Plain HPM	0.34	1.75	0	0.2	0
HPM+CNF	0.34	1.75	0.05	0.2	1.19×10^{10}

Autogenous shrinkage is measured in specimens contained in corrugated plastic tubes according to ASTM C1698-09[10], where volumetric deformation is restrained to longitudinal change due to the corrugated feature of the tubes. The tubes are approximately 43 cm in length, and 3 cm in diameter, and they are placed on oiled steel frames that allow longitudinal movement. The test

set-up is shown in Fig 3.10. Fresh cement paste or mortar is poured into the tube while vibrated, and the specimen is then sealed with caps at both ends. The initial length of the capped tube is measured with a calibration bar before test, and the measurement is started from the point of initial setting. Though autogenous shrinkage is believed to occur immediately after mixing with water and cement while it is still liquid, the method is not able to measure the deformation before the plastic skeleton forms. The linear deformation is measured with an electronic digital indicator continuously during the entire measurement period. The initial setting time is measured for all six mixes using a Vicat needle test in accordance with ASTM C191[11]. Two identical samples are tested in parallel and an average shrinkage strain is calculated in 3 days. Beyond 3 days, the shrinkage is too small to measure with the deformation indicator. Samples were kept and measured in an environmental chamber at 23 °C and 50 % relative humidity.



Figure 3.10 Set up of autogenous shrinkage test

3.5.2 Restrain Ring Test

Like other forms of shrinkage, autogenous shrinkage creates cracks when the shrinkage strain exceeds the strain capacity of the material. The ability to restrain shrinkage cracking can be considered as important as reducing the shrinkage strain. To examine CNF's effect on cracking resistance, a restrained ring test is performed on the same high-performance mortar mixes used for the autogenous shrinkage testing. The dimensions of the ring are shown in Fig. 3.11. The ratio of the thickness of the mortar sample and the steel is set to be 3, which ensures a high likelihood that a crack will form within a few days [8]. A mortar ring is cast around a steel ring, which introduces hoop tensile stress once the material begins to shrink as shown in Fig. 3.12. When the tensile stress exceeds the tensile strength (in conjunction with fracture mechanics [12]) of the mortar ring, a crack forms and will typically continue to enlarge with time.

Fresh mortar is poured between the steel ring and the outer molds in three layers, and manual roddings are applied to each layer for consolidation. The rings are then sealed, and the specimen is cured for 24 h before the forms are removed. After demolding, samples are immediately sealed with silicone gel to prevent drying, and kept in an environmental chamber (23 °C, 50%) for the entire duration of measurement. The time of the first cracking is recorded, and then the evolution of crack width is monitored with a microscope for control and CNF sample for two weeks.

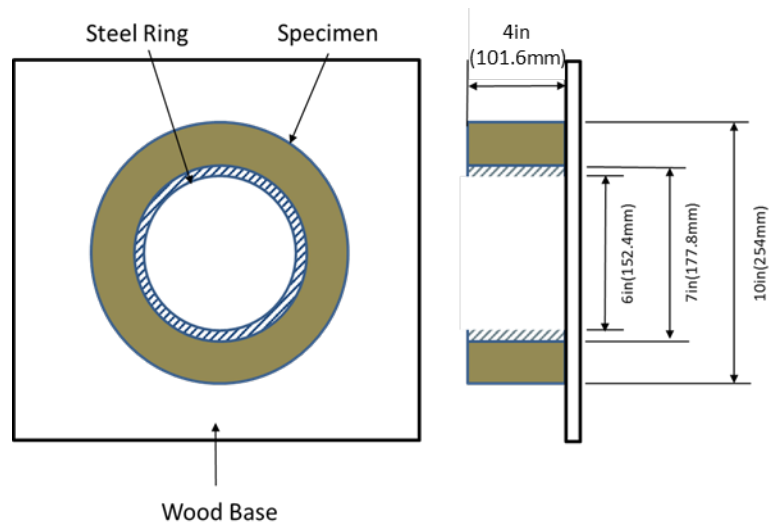


Figure 3.11 Set up of restrained ring test



Figure 3.12 Restrained ring sample and portable microscope

3.6 Experiment Results and Discussions

3.6.1 Mechanical Tests

Flexural strength and MOE are calculated for cement paste and mortar with 0, 0.05wt% and 0.10wt% of CNFs added from three-point bending test, and the results are shown in Fig 3.13 and 3.14 accordingly. In general, both 0.05% and 0.1 wt% could increase the flexural strength and

MOE of pastes and mortars, where 0.1 wt% of CNFs behaviors better than 0.05 wt% of CNF's addition. For cement paste, the flexural strength and MOE are increased by 18% and 21% at 28 days with 0.1 wt% of CNF compared to control sample, respectively. For the 28-day mortar, the higher dosage of CNF (0.1 wt% to cement weight) exhibits a 28% increase in flexural strength and 34% in Young's modulus. Since 0.1 wt% is proven to have a better performance than 0.05 wt%, it is only used dosage for concrete sample under compression test.

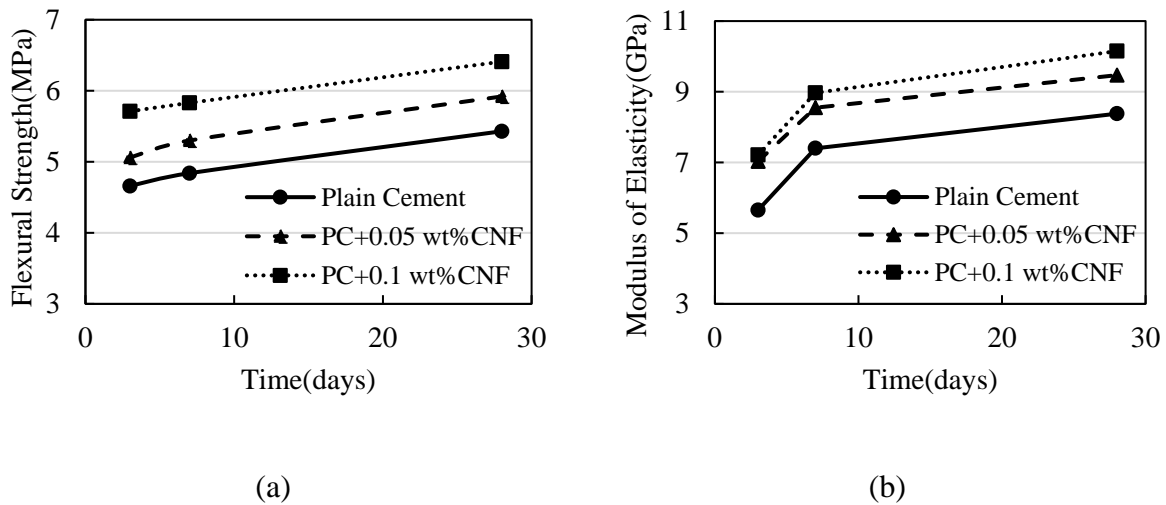


Figure 3.13 Three-point bending results of cement paste:
a) flexural strength; b) Young's modulus

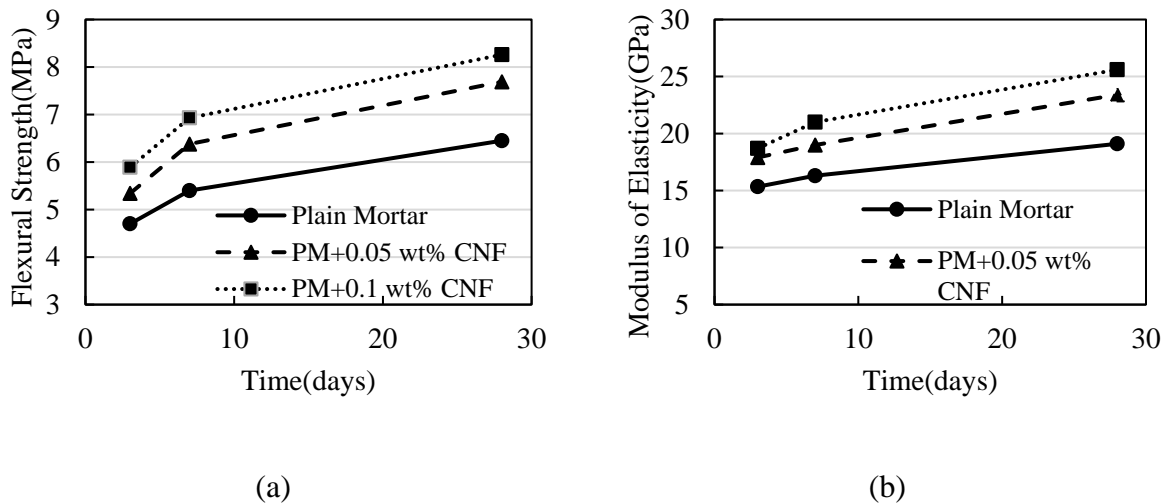


Figure 3.14 Three-point bending results of cement mortar:
a) flexural strength; b) Young's modulus

The test of cement composite at macroscale is then upscaled to concrete material. Results of the MOE and compressive strength for plain concrete and concrete with 0.1 wt% CNFs at 28 days are reported in Table 3.4. The MOE is increased from 35.7 to 46.2 GPa, which corresponds to a 30% improvement, while the compressive strength does not exhibit a significant increase, where only 10% of improvement has been seen at the end of 28 days. Considering the volume fraction of CNFs within the concrete matrix, the enhancement of Young's modulus is considerably significant. This could also be attributed to the reinforcement on ITZ between the aggregates and the bulk paste. Similar results have been reported for carbon nanotube reinforced concrete[13], where Young's modulus is increased by 56% and compressive strength is increased by 6% by adding 0.1 wt% well-dispersed CNTs. Though CNTs and CNFs are added for the same dosage weight of 0.1 wt% to cement weight, CNFs' specific surface area and fiber count[14] compared to CNTs are both lower due to the finer dimension of CNTs (around 20 nm in diameter). This could explain the differences in the Young's modulus, observed between CNT and CNF reinforced concrete.

Table 3.4. Results on compression test for concrete with or without CNF

	Young's Modulus (GPa)	Compressive Strength (MPa)
Plain Concrete	35.7	46.7
0.1 wt% CNF + Concrete	46.2	50.5

While considering the fiber volume fraction in different mixtures, the effect of CNFs on Young's modulus in mortar and concrete samples are significantly more pronounced than cement paste.

Due to the introduction of fine and course aggregates in mortar and concrete matrix, the CNF's volume fraction is reduced from 0.083% to 0.036% for mortar and 0.022% for concrete, however the improvement is 10% more in mortar and concrete than in paste, as shown in Table 3.5. This is in contrast to conventional fiber reinforcement in cement-based materials. Conventional micro fibers only reinforced the paste area within mortar sample while CNF has the potential to reinforce the interfacial zone between paste and aggregates.

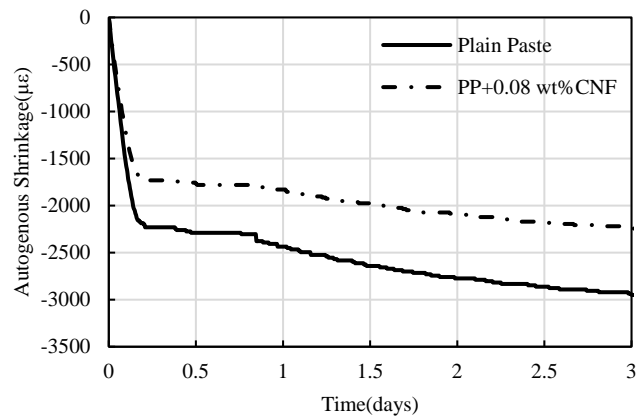
Table 3.5 Summary table for the effect of CNF within cement composites

	Tests	CNF Volume Fraction (%)	Young's Modulus Improvement (%)	Flexural Strength Improvement (%)	Compressive Strength Improvement (%)
Cement Paste (CP)	Flexural	0.083	21	18	Not measured
Cement Mortar (M)	Flexural	0.036	34	28	Not measured
Concrete (C)	Compression	0.022	29	Not measured	10

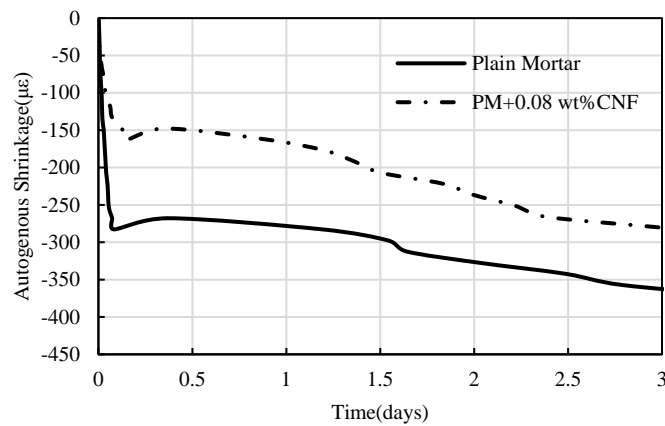
3.6.2 Autogenous Shrinkage

Values of autogenous shrinkage for cement paste ($w/c=0.4$), mortar ($w/c=0.4$) and high-performance mortar ($w/c=0.34$), both with and without CNF, are shown in Fig. 3.15. In general, the cement paste exhibits a larger autogenous shrinkage than the mortar, likely due to the sand providing restraint to the shrinkage in the cement paste matrix. The high-performance mortar ($w/c=0.34$) exhibits higher autogenous shrinkage values, compared to the mortar with $w/c=0.4$. The addition of CNFs decreases the autogenous shrinkage in all three mixes. 0.08 wt% of CNF reduces the 3-day autogenous shrinkage of cement paste with $w/c=0.4$ from 3000 to 2200

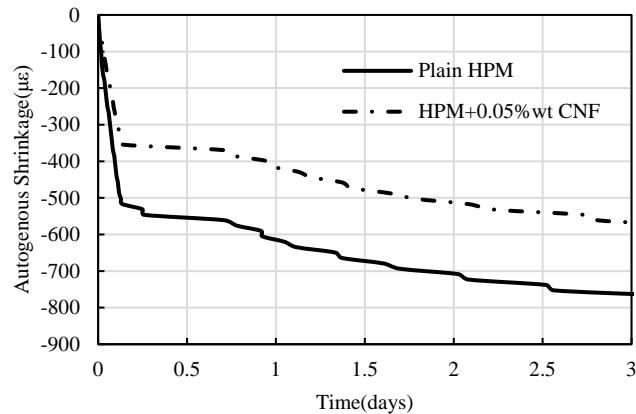
microstrain. The 3-day autogenous shrinkage of mortars is reduced from 370 to 280 microstrain with 0.08 wt% of CNFs. It should be mentioned here that the CNF volume fraction in the mortar specimens is lower than that of the pastes, simply because in mortars there is a smaller amount of cement. In addition, 0.05 wt% of CNF is able to reduce the autogenous shrinkage from 770 to 580 microstrain in HPM at the end of 3 days measurement. CNF shows a similar effect in autogenous shrinkage mitigation in HPM, where w/c ratio and s/c ratio are both smaller than regular mortar.



(a)



(b)



(c)

Figure 3.15. Autogenous shrinkage for: (a) cement paste ($w:c=0.4$); (b) cement mortar ($w:c:s=0.4:1:2.75$); (c) high performance mortar(HPM) ($w:c:s=0.34:1:1.75$)

3.6.3 Restrained Ring Test

Results of the restrained ring test are presented in Fig. 3.16. The first crack of plain HPM specimen forms 3 days after casting, while the CNF added sample has the first crack on the fourth day of observation. The addition of CNFs delays the formation of the first crack by one day. Crack widths are recorded immediately after cracking, and continued for twelve consecutive days. After the first crack, specimens are considered partially restrained. However, as shrinkage continues, the width of the crack can increase with time. It was found that at the end of the twelve-day measurement, the crack width increased about 0.7 mm for plain HPM and 0.5 mm for the CNF reinforced HPM. Results indicate that CNFs are not only able to effectively delay the development of the first crack, but also reduce the width of the crack.

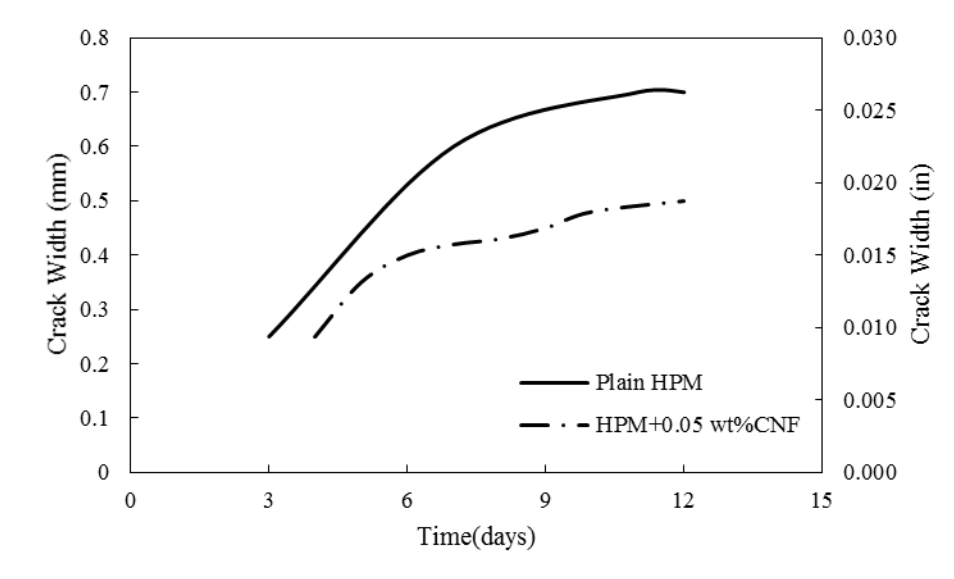


Figure 3.16. Restrained ring test of cement mortar with or without CNF

Gdoutos *et al.*[15] has conducted a fracture mechanics study with CNT and CNF added cement mortar and found out that the effective crack length is higher with 0.1 wt% CNF addition. Also, a large increase of strain energy release rate was observed, which is considered the energy necessary to initiate a crack. With the hypothesis that CNF enhance the material's ability to control the coalescence of cracks at the nanoscale and the subsequent formation of the microcracks, the required energy to initiate cracking is increased. Danoglidis[16] evaluate another property of CNT added cement mortar: first crack strength, which is defined as the point on the load-deflection curve where the curve becomes nonlinear. With a higher first crack strength in CNT-reinforced mortar, the material could sustain a larger maximum stress before microcracking and it is controlled by matrix parameters. Both studies explain the mechanism of the delay of first crack in restrained ring test with nanoreinforced mortar. On the other hand, the development of crack width is significantly restrained due to the addition of CNF, which was also seen in micro fiber reinforced cement composites [8]. It is generally accepted that micro-

fibers with high fiber specific surface (FSS) area are particularly effective in controlling the shrinkage cracking width [14]. FSS is defined as a function of fiber surface area and the fiber count in a unit volume of concrete. The concept could extend to nano-fibers that have much larger FSS than micro fibers, which suggests a stronger effect on shrinkage cracking mitigation.

CNF's effect on autogenous shrinkage and shrinkage are concluded in Table 3.6. Similarly to mechanical properties testing, the volume fraction of CNF is lower in mortar compared to paste sample, yet a similar reduction on autogenous shrinkage has been seen for both samples. It indicates that CNF's effect on reducing the autogenous shrinkage is more pronounced in mortar than in paste. Furthermore, the effect of CNF on reducing the autogenous shrinkage and restraining the crack width is quite promising on high performance concrete application compared to micro fibers.

Table 3.6 Comparison of autogenous shrinkage and shrinkage cracking results

	CNF Volume Fraction	Autogenous Shrinkage Reduction	Shrinkage Crack Width
PC+0.08 wt% CNF (w:c=0.4)	0.093%	23%	--
PM+0.08 wt% CNF (w:c:s=0.4:1:2.75)	0.038%	24%	--
HPM+0.05 wt% CNF (w:c:s=0.34:1:1.75)	0.050%	25%	29%

3.7 Summary

The results of flexural tests indicate that CNF's addition could increase the flexural strength and Young's modulus for both cement paste and mortar materials. The effect is more obvious for mortar especially considering the volume fraction of CNF added is substantially less in mortar than in paste. This indicates that CNF changes the interfacial zone between the aggregate and bulk paste resulting in a higher improvement on mortar. The test is upscaled to concrete material and compression test is conducted. The 0.1 wt% of CNF is able to increase the MOE of concrete material without increasing its compressive strength. In addition, autogenous shrinkage and shrinkage cracking tests are conducted with cement paste and mortar with or without CNF. It finds the addition of well-dispersed CNF could reduce the autogenous shrinkage, and the effect is more pronounced for mortar than for paste considering the fiber volume fraction. The reducing effect on autogenous shrinkage in regular mortar and high performance mortar is comparable due to the addition of CNFs. Moreover, CNFs are not only able to delay the formation of shrinkage cracks, but also restrain the development of the crack width.

References

- [1] Y. Jenq, S.P. Shah, Two Parameter Fracture Model for Concrete, *J. Eng. Mech.* 111 (1985) 1227–1241. doi:10.1061/(ASCE)0733-9399(1985)111:10(1227).
- [2] ASTM C469/C469-14, Standard Test Method for Static Modulus of Elasticity and Poisson's Ratio of Concrete in Compression, West Conshohocken, PA, 2014.
www.astm.org.
- [3] P. Lura, O.M. Jensen, K. van Breugel, Autogenous shrinkage in high-performance cement paste: An evaluation of basic mechanisms, *Cem. Concr. Res.* 33 (2003) 223–232.
doi:10.1016/S0008-8846(02)00890-6.

- [4] A. Noushini, K. Vessalas, G. Arabian, B. Samali, Drying shrinkage behaviour of fibre reinforced concrete incorporating polyvinyl alcohol fibres and fly ash, *Adv. Civ. Eng.* 2014 (2014).
- [5] K. Kohno, T. Okamoto, Y. Isikawa, T. Sibata, H. Mori, Effects of artificial lightweight aggregate on autogenous shrinkage of concrete, *Cem. Concr. Res.* 29 (1999) 611–614.
- [6] O.M. Jensen, P.F. Hansen, Water-entrained cement-based materials: I. Principles and theoretical background, *Cem. Concr. Res.* 31 (2001) 647–654.
doi:[https://doi.org/10.1016/S0008-8846\(01\)00463-X](https://doi.org/10.1016/S0008-8846(01)00463-X).
- [7] O.M. Jensen, P.F. Hansen, Water-entrained cement-based materials: II. Experimental observations, *Cem. Concr. Res.* 32 (2002) 973–978. doi:[https://doi.org/10.1016/S0008-8846\(02\)00737-8](https://doi.org/10.1016/S0008-8846(02)00737-8).
- [8] and S.P.S. Mirosław Grzybowski, Shrinkage Cracking of Fiber Reinforced Concrete, *Mater. J.* 87 (n.d.). doi:10.14359/1951.
- [9] S. Kawashima, S.P. Shah, Early-age autogenous and drying shrinkage behavior of cellulose fiber-reinforced cementitious materials, *Cem. Concr. Compos.* 33 (2011) 201–208. doi:<https://doi.org/10.1016/j.cemconcomp.2010.10.018>.
- [10] A. International, ASTM C1698-09, Standard Test Method for Autogenous Strain of Cement Paste and Mortar, West Conshohocken, PA, 2014. www.astm.org.
- [11] ASTM C191-13, Standard Test Methods for Time of Setting of Hydraulic Cement by Vicat Needle, West Conshohocken, PA, 2013. www.astm.org.

- [12] C.O. Surendra P. Shah Shashidhara Marikunte, Wei Yang, and Emil Becq-Giraudon, A Method to Predict Shrinkage Cracking of Concrete, *Mater. J.* 95 (n.d.).
doi:10.14359/9875.
- [13] M.S.K.-G. Surendra P. Shah, Uncoupling Modulus of Elasticity and Strength, *Concr. Int.* 39 (2017) 37–42.
- [14] ACI Committee 544, ACI 544.1R-96 Report on fiber reinforced concrete, 2002.
- [15] E.E. Gdoutos, M.S. Konsta-Gdoutos, P.A. Danoglidis, Portland cement mortar nanocomposites at low carbon nanotube and carbon nanofiber content: A fracture mechanics experimental study, *Cem. Concr. Compos.* 70 (2016) 110–118.
doi:10.1016/j.cemconcomp.2016.03.010.
- [16] P.A. Danoglidis, M.S. Konsta-Gdoutos, E.E. Gdoutos, S.P. Shah, Strength, energy absorption capability and self-sensing properties of multifunctional carbon nanotube reinforced mortars, *Constr. Build. Mater.* 120 (2016) 265–274.
doi:10.1016/j.conbuildmat.2016.05.049.

Chapter 4

Experimental Work with CNT Reinforced Cementitious Materials in Nano Scale

4.1 Introduction

The mechanical tests with CNT reinforced cement paste, mortar and concrete suggest a nanomodification on the interface area between bulk paste and aggregates, which is known as the weakest link in the composite matrix and significantly affects the properties of concrete. The bulk paste is modified in the vicinity of the aggregate particles, which forms the transitional zone next to the aggregate. The formation of interfacial transitional zone (ITZ) is generally described as a phenomenon associated with particle packing, known as the “wall effect”, and the anhydrous cement grains pack against the relatively flat aggregate surface [1]. Another explanation of the paste modification is proposed by Ollivier [2], where microbleeding leads to an accumulation of water around the aggregate particles before setting and a gradient of

anhydrous cement is present. The relatively high mobility ions, such as Ca^{++} , Al^{3+} , and SO_4^{2-} , tend to diffuse into the ITZ, which results in the precipitation of calcium hydroxide (CH) and aluminate hydration products such as ettringite. Lower mobility ions like silicate and ferrite tend to form hydration products near their dissolution source. The modification on ITZ could be further supported by the Ca/Si ratio because it can distinguish hydrates rich in C-S-H and CH [3]. C-S-H typically exhibits $0.8 < \text{Ca/Si} < 2.5$, which CH typically exhibits $\text{Ca/Si} > 10$. Near aggregates, the Ca/Si ratio is increased because of the presence of the large CH crystals [4], as shown in Fig. 1.

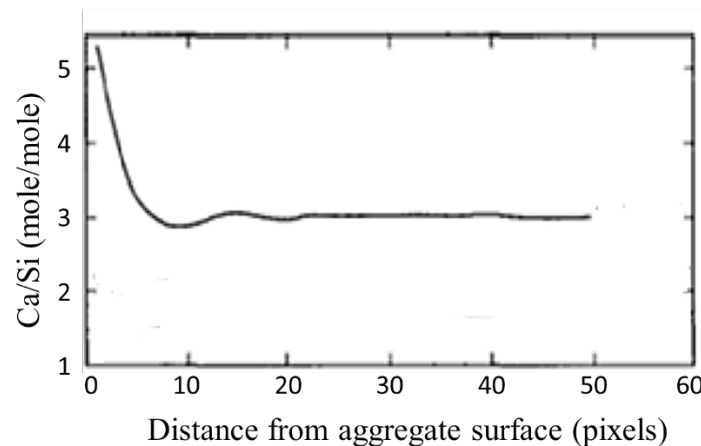


Figure 4.1. Ca/Si ratio vs. distance from aggregate surface (based on [4])

The average thickness of ITZ is 20-40 μm , and the region is characterized with higher w/c and thus a higher porosity than the bulk paste. The lower strength and stiffness of the ITZ directly affects the strength and stiffness of concrete; hence it is expected that reinforcing the ITZ will greatly improve the concrete bulk properties. Because of the porous structure and weak compaction of cement hydrates, modification of ITZ can be achieved by using pozzolanic materials, such as silica fume [5], where silica fume reacts with CH producing more C-S-H. However, addition of silica fume often results in a more brittle concrete [6].

A thorough physical and chemical characterization of the effect of CNFs on the ITZ between cement paste and aggregates is conducted, including MOE evaluation using peak-force quantitative nano-mechanical mapping (QNM) under atomic force microscopy (AFM) and scanning electron microscopy (SEM)-based energy dispersive micro-analysis (EDS). The AFM-QNM, see Fig. 2, provides MOE with higher spatial resolution than the commonly used nanoindentation technique [7]. The AFM-QNM technique has been successfully used on comparative study of nano-mechanical properties of cement paste with the nanoindentation, where a good agreement is found between the two techniques [8][9]. It has also been used to investigate MOE on C-S-H gel/cement grain interfaces with the addition of nanoSiO₂ [10], and it is found to be improved by the nano-reinforcement. The technique is being used to investigate the ITZ between cement paste and aggregates for the first time. The microstructure of ITZ is also examined with SEM/EDS, where Ca/Si ratio is measured with line-scanning protocol.

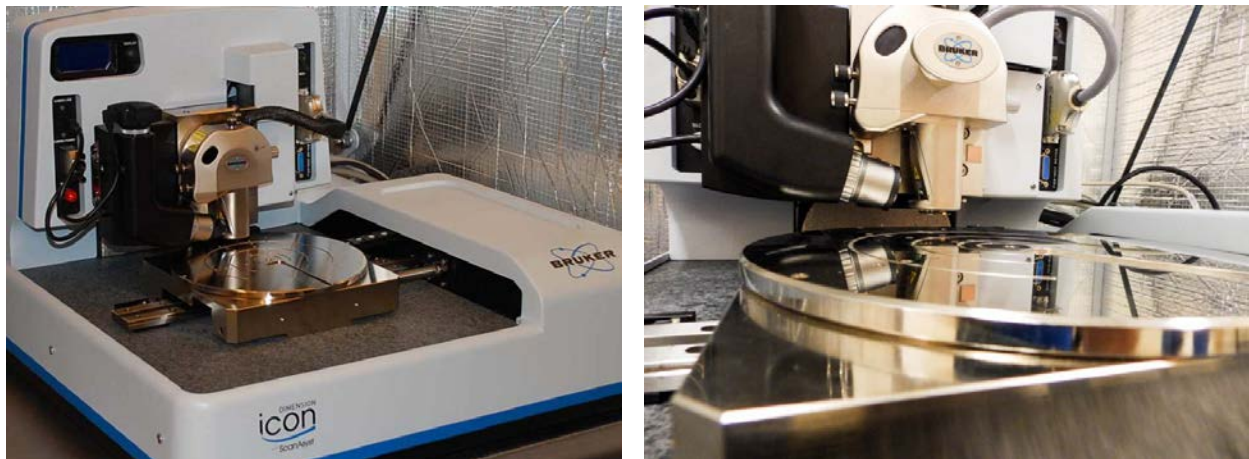


Figure 4.2. AFM equipment

4.2 Nanomechanical Characterization with CNT Reinforced Cement Composite

4.2.1 PeakForce Quantitative Nanoscale Mechanical Characterization (QNM)

PeakForce QNM can measure the mechanical properties of the sample, including MOE, adhesion and deformation, at atomic scale resolution. By tapping on the sample surface, the PeakForce mode produces force curves and extract quantitative data to create property maps. The AFM probe is brought to contact with the surface by attractive forces for a short period of time and a force-separation curve is collected for each scan point without deforming the surface sample [11]. The tapping process controls the maximum force on the tip by keeping a constant vibration amplitude of the cantilever. The method is especially useful to make localized measurements of MOE, which is of interest in this investigation of the ITZ, which is a narrow area in microscale. This section will demonstrate the procedure for the sample preparation and the measuring process.

4.2.2 Sample Preparation

To achieve reliable results during examination in QNM, high quality sample preparation is required. Mortar and concrete samples are prepared, where the w/c is 0.485, and s/c is 2.75. For mortar, the cement is mixed with water and sand followed the regular mortar mixing procedure. For concrete, a large limestone aggregate is embedded in mortar while mixing. After 28 days of moist curing, a small block is trimmed from the mortar or concrete specimen. Because of the addition of nanomaterials, the CNF sample appears dark grey, while the sample without CNFs is light grey. The sample is then ground with a series of sandpapers, ranging from 240 to 400 grits for 5 minutes at each grade. After the finest grinding step, the sample is polished with progressively smaller diamond suspensions on a polishing cloth from 9 μm to 1 μm , until the surface is flat and scratch free under optical microscopy. The polishing machine is set to be 150

rpm, and it lasts for 10-15 mins for each diamond suspension grade. Finally, the sample is cleaned with ethanol in an ultrasonic bath for 10 mins. The flatness of the sample surface is crucial for PeakForce QNM measurements, and it will be examined under AFM.

In order to assess the ITZ mechanical properties of specimens with and without CNFs, a $10\mu\text{m} \times 10\mu\text{m}$ test area next to aggregate is chosen. As mentioned above, the thickness of ITZ is 20 to $40\mu\text{m}$. Therefore, the $10\mu\text{m} \times 10\mu\text{m}$ test area is adequate to collect the mechanical properties of ITZ. The ITZ for mortar sample is between bulk paste and sand, which is shown in Fig. 3 and 4. While the ITZ for concrete sample is between bulk paste and limestone aggregate as shown in Fig. 5 and 6.

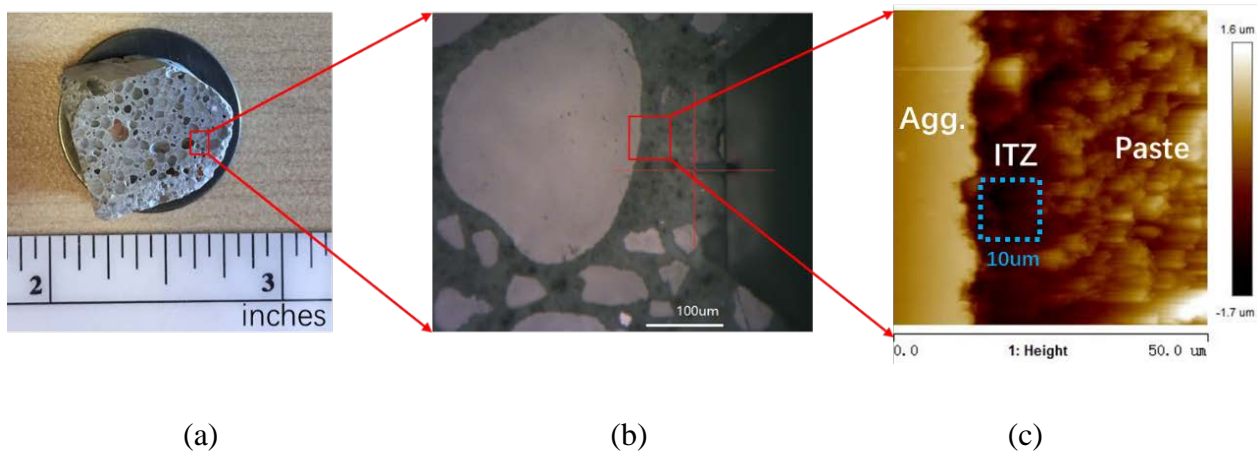


Figure 4.3. Test area for AFM QNM (mortar without CNF)

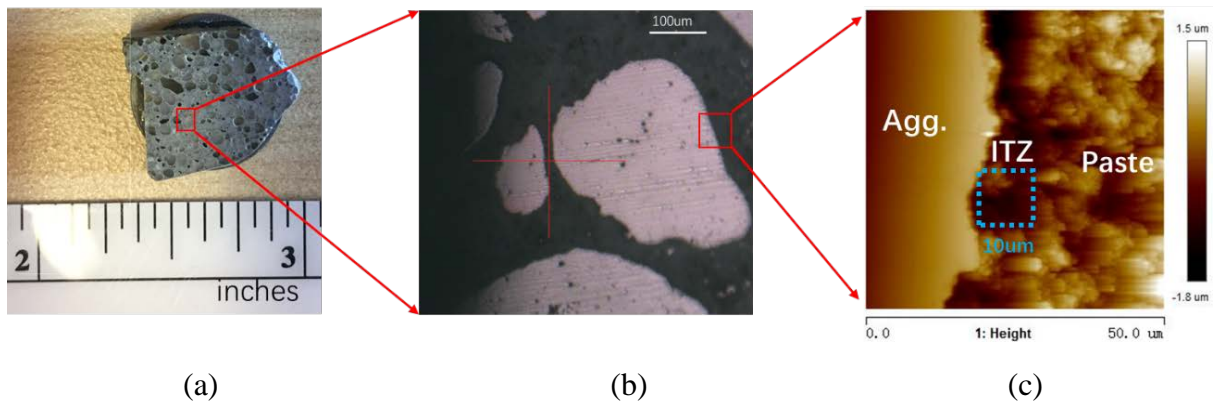


Figure 4.4 Test area for AFM QNM (mortar with CNF)

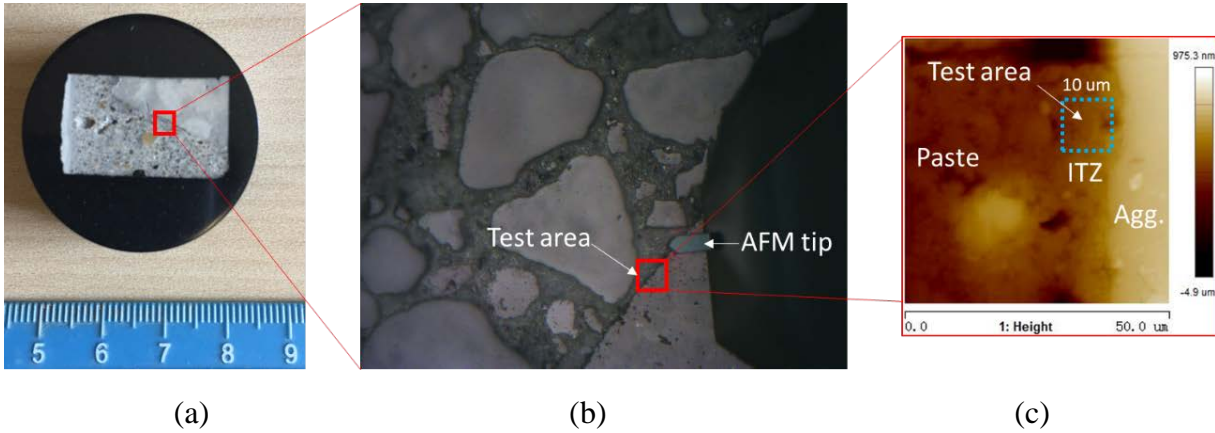


Figure 4.5. Test area for AFM-QNM (concrete without CNFs)

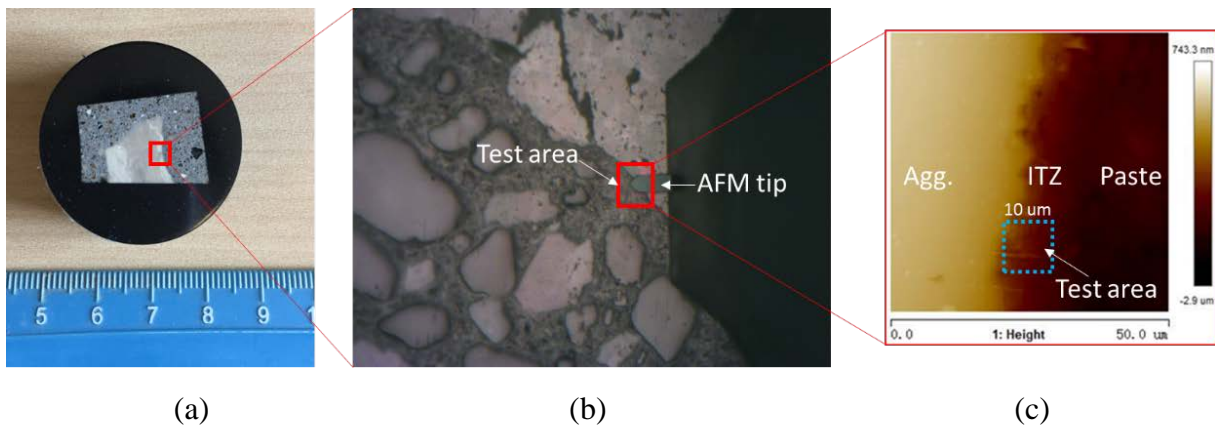


Figure 4.6. Test area for AFM-QNM (concrete with CNFs)

The peak force QNM is a contact-type measurement; the tip directly touches the sample and it may scratch the surface if it is not smooth enough. Therefore, a smooth surface is especially essential for getting accurate and repeatable morphology information and mechanical properties of the test area. The 3D topography of the samples is observed based on AFM tapping mode, see Fig. 7. The aggregate has the smoothest surface and the largest height after polishing compared to ITZ and paste. Since the aggregate is the stiffest part in the sample, it is almost impossible to

get an even surface from aggregate to paste as a whole. Fortunately, with a scan area of 10 microns square, the scan can remain within the ITZ area. Therefore, to confirm if the test area has been thoroughly polished, the spectral Root-Mean-Square (RMS) amplitude is measured at baseline within ITZ. For example, it can be seen from Fig. 4.8 that the roughness of test area of mortar sample with CNF fluctuated from -150 nm to 200 nm, while the roughness of test area of mortar sample without CNF varied from -200 nm to 200 nm. Therefore, the RMS for mortar sample with CNF is 87.4 nm and 96.6 nm for test sample without CNF. The roughness for all test samples are reported in Table 1. These values are adequate to conduct an AFM-QNM test.

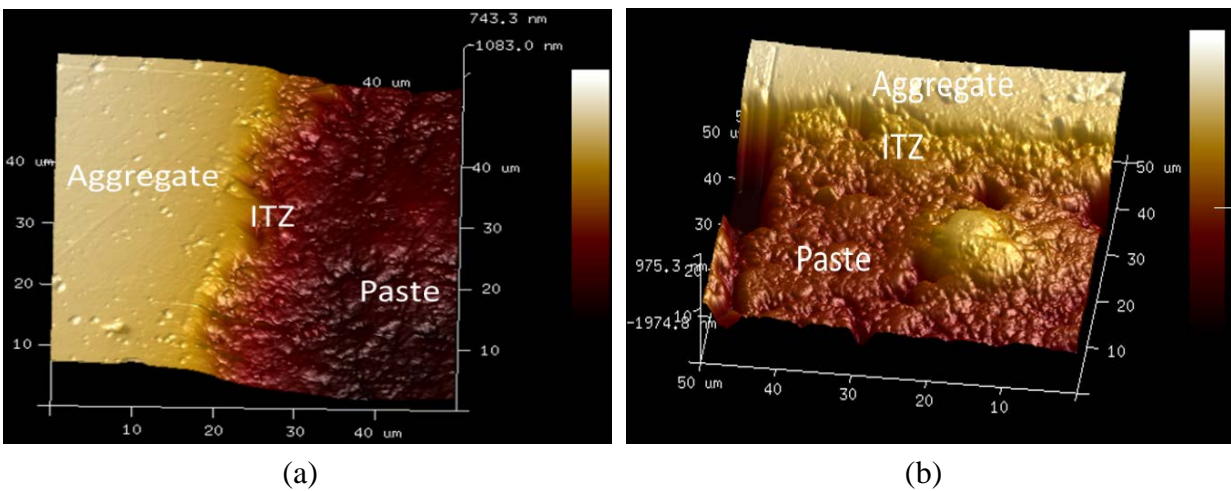


Figure 4.7. Topography of ITZ (a) without CNF and (b) with CNF

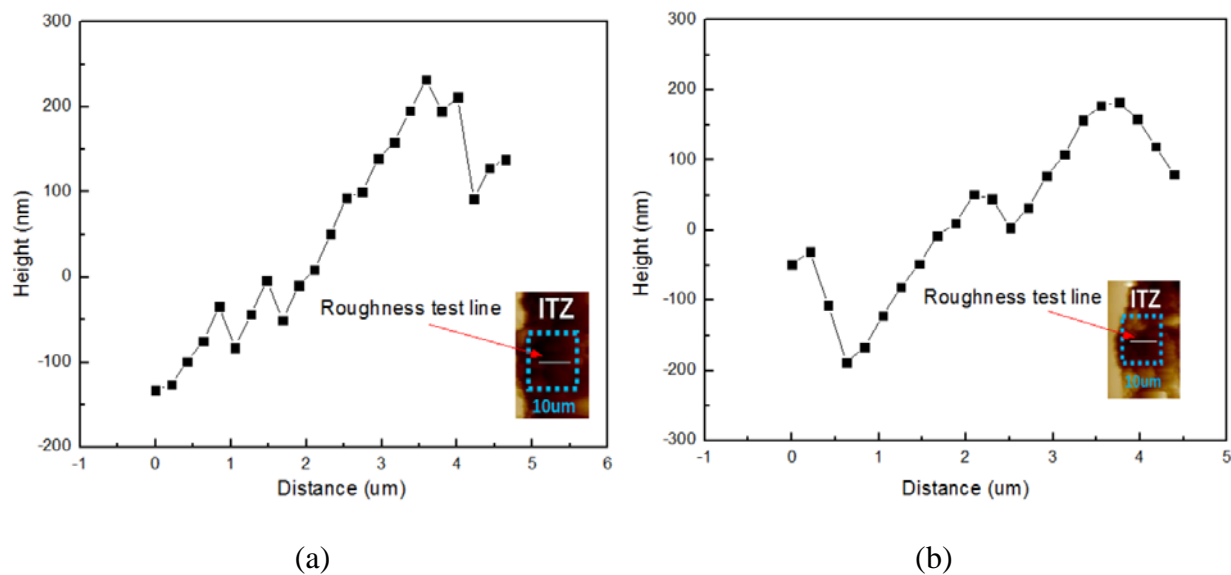


Figure 4.8. Roughness of mortar samples (a) with CNF and (b) without CNF

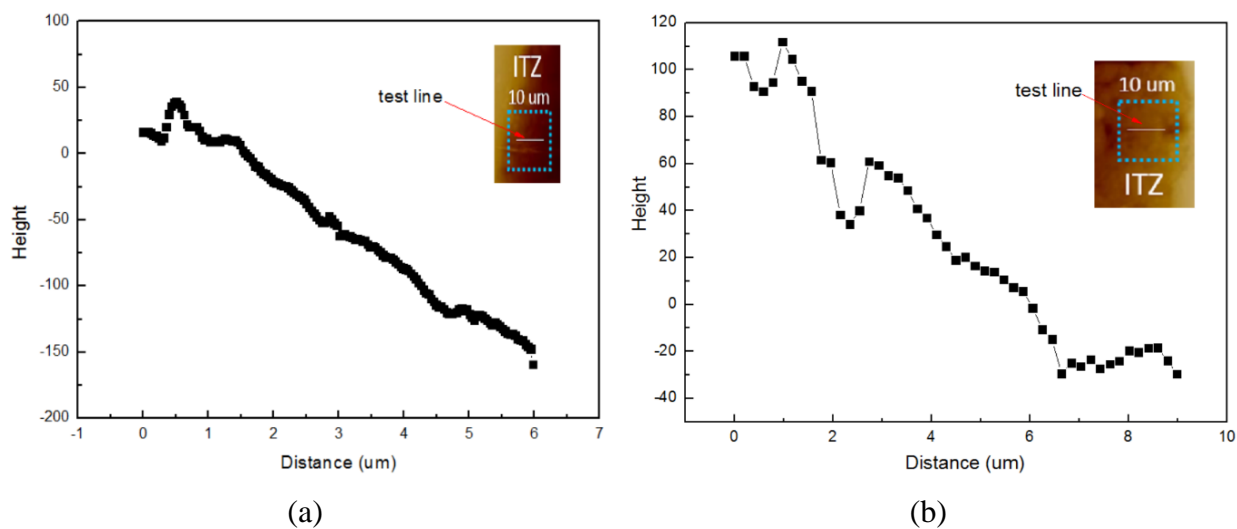


Figure 4.9. Roughness of concrete samples (a) with CNF and (b) without CNF

Table 1. Roughness of test samples

	Plain Sample	CNF Sample
Mortar	96.6	87.4

Concrete (nm)	83.4	71.3
----------------------	------	------

4.2.3 Test Process

The probe used for the AFM measurements is Tap-525A and has a spring constant of 200 N/m. Before each measurement, a calibration is needed for deflection sensitivity for the cantilever and tip radius for the probe. The deflection sensitivity is calibrated against a clean sapphire sample. The tip radius is calibrated against a highly oriented pyrolytic graphite sample (HOPG) which has a MOE similar to cement sample (HOPG is 18 GPa in modulus). After calibration, the deflection sensitivity and tip radius are input into AFM software as calculation parameters. Then, the probe indents a selected area of the sample with the scanning rate of 0.5 Hz at a resolution of 256 pixels by 256 pixels within the test area. As shown in Fig. 9, the cantilever is pulled down toward the surface by attractive forces (step 1), and get in touch with the substrate surface (step 2). The tip then stays on the surface and the force increases until the it reaches the peak force (step 3). Then the probe starts to withdraw (step 4) and the adhesion force increases until the tip is pulled of the surface (step 5). The tip is then pulled back to air and a force-separation cycle finishes (step 6). The estimation of modulus is obtained between step 1-3, while the adhesion is

calculated based on step 4-6.

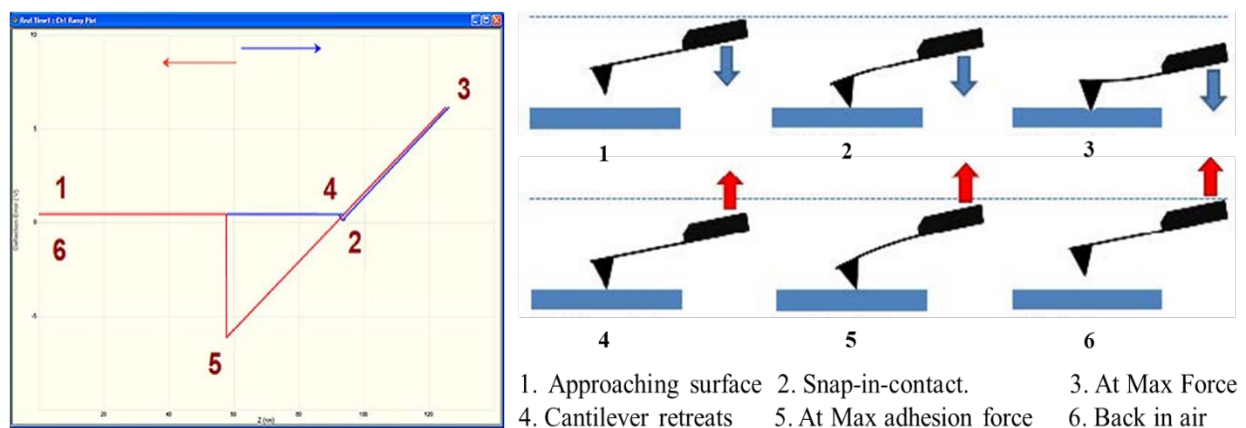


Figure 4.10. Test process of PeakForce Tapping Mode

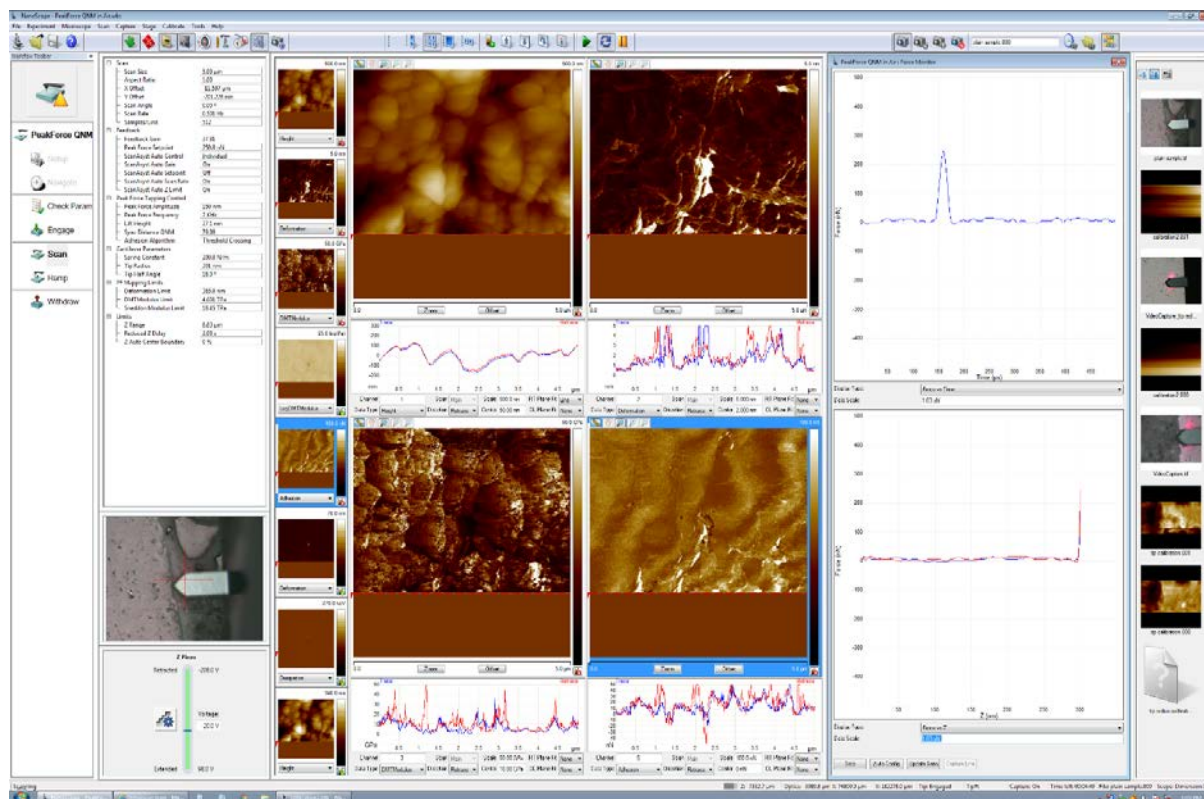


Figure 4.11. Nanoscope Analysis Interface

The MOE is calculated using the DMT model, which is valid for a spherical indenter[12]. The equation used for analysis is described below.

$$F_L(i) = \frac{4}{3}E^*\sqrt{R^*}d^{3/2} + F_{pull-off} \quad (1)$$

where F_L is the load force, E^* is the reduced Young's modulus, $E^* = E/(1-\nu^2)$, ν is the Poisson ratio, R^* is the reduced radius and $1/R^* = 1/R_{indenter} + 1/R_{surface}$, d is the indentation depth, and $F_{pull-off}$ is the force at the point of pull-off of the AFM probe, or the pull-off force. The pull-off force can be found from the force-deformation curves collected from QNM test. The Poisson ratios for the calculation is assumed to be 0.3. The obtained property map is processed through the Nanoscope Analysis (Bruker) software.

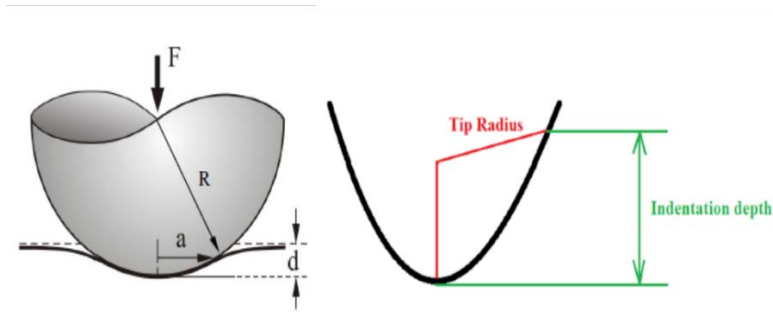


Figure 4.12. Schematic photo of spherical AFM tip

Another important mechanical property acquired in the QNM is the adhesion force, which can be the result of any attractive force between the tip and the sample. The adhesion typically increases with increasing probe radius, and is estimated by accounting the area below the zero force reference and above the withdrawing curve, as seen in Fig. 12. The adhesion force measured with QNM is much more meaningful if the tip is functionalized. If the silica tip is functionalized with CNTs, the adhesion between the probe and substrate can reflect the chemical interaction between the nanomaterial and cement hydration products.

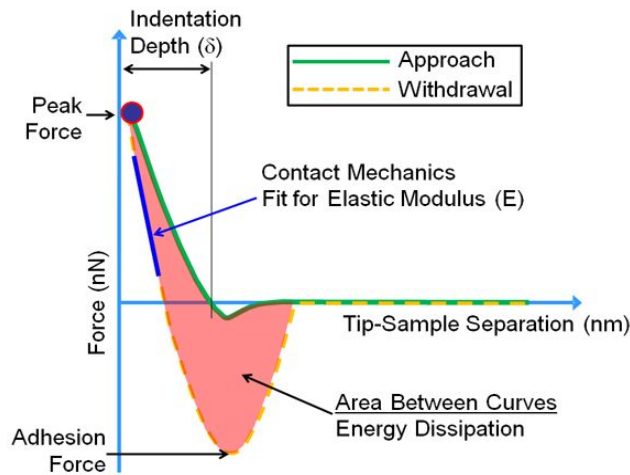


Figure 13. Tip-separation curve

4.2.4 Test Results

Each point on Fig. 8 is the average of 256 point on the parallel direction along the sand edge and they are plotted along the 10 μ m along the distance to the sand. A statistical process has been performed to the results in Fig. 8 and a possibility plot of Young's modulus is drawn in Fig. 9. As the left column shows, the addition of CNF moves the probability curve to the right, and the average Young's modulus is increased by 36.7%. The right column of the Fig 18 shows the statistic result of interface area with or without CNF. The average Young's modulus is also developed by 13.5%. It approves that CNF is not only able to increase the Young's modulus for cement paste, but also the interface between sand and paste. This is very difficult to achieve by using conventional fiber reinforcement.

Fig. 8 shows the probability distribution of Young's modulus. It is obvious that the Young's moduli of ITZ without CNF are concentrated in 7.5GPa~22GPa while the Young's moduli of

ITZ with CNF are centered on 15GPa~37GPa. The concentration tendency is shifted to the right for CNF reinforced ITZ, which implies that the addition of CNFs does strength the stiffness of ITZ.

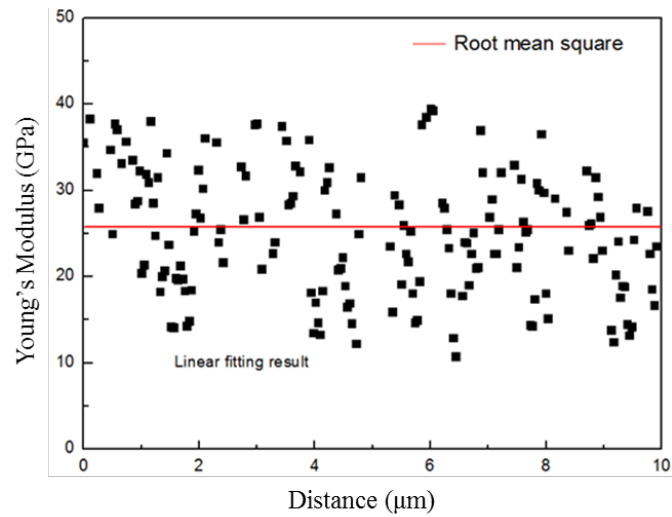


Figure 4.13. Young's Modulus of concrete with CNF (left-hand side close to the aggregate)

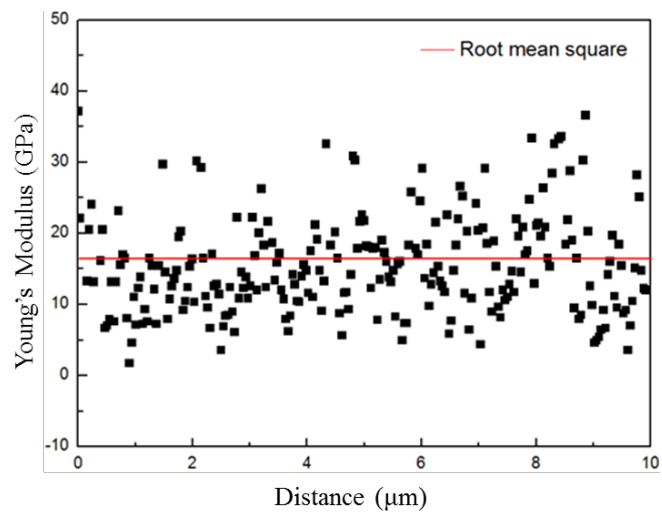


Figure 4.14. Young's Modulus of concrete without CNF (right-hand side close to the aggregate)

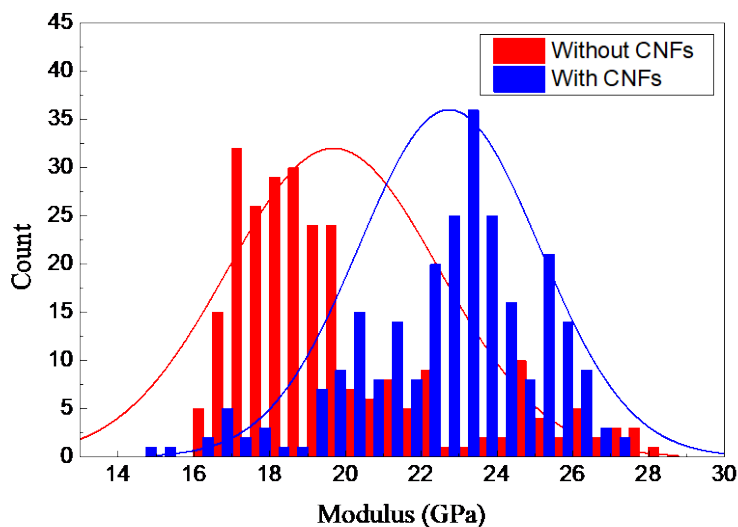


Figure 4.15. Histogram of Young's Modulus for Interface Area of Mortar

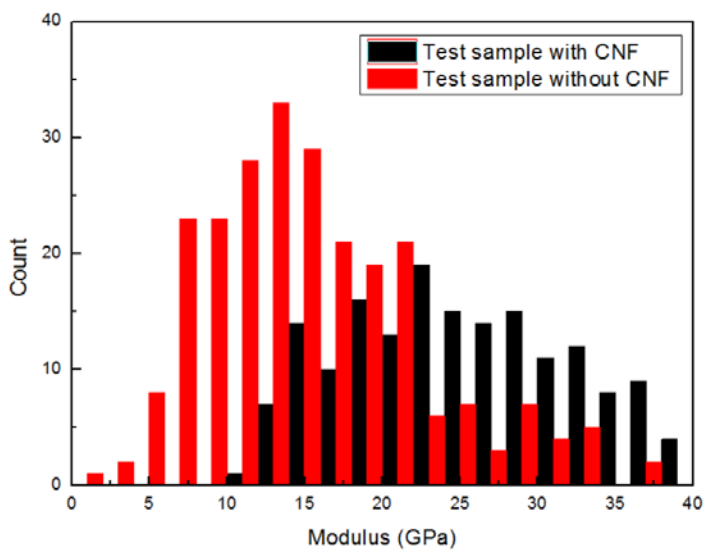


Figure 4.16. Histogram of Young's Modulus for Interface Area of Concrete

Table 2. MOE on ITZ for Mortar of Concrete from AFM-QNM Test

	Plain Sample	CNF Added Sample
Mortar (GPa)	18	24

Concrete (GPa)	15	25
----------------	----	----

4.3 SEM/EDS Test with CNT Reinforced Cement Composite

4.3.1 Scanning Electron Microscope (SEM) with CNT reinforced concrete

SEM imaging has the ability to provide images of the microstructure in sub-micro scale and perform chemical analysis simultaneously. In this session, the application of SEM on concrete material is presented with a focus on the chemical analysis at the interface area. The SEM used is Hitachi SU8030 as shown in Fig. 4.17. The imaging modes used in the study are secondary electron and X-ray, which are based on the electron reflection from the beam and specimen interaction. The concrete sample is polished and a thin carbon layer is deposited on the polished surface to increase the electron conductivity.



Figure 4.17. Hitachi SU8030 SEM

Secondary electrons (SE) are low-energy electrons produced as a result of an elastic collision of a primary beam electron with an electron of an atom within the specimen [13]. It produces the detailed images of surface topography especially when combined with the in situ chemical analysis. The energy-dispersive X-ray spectrum (EDS) is a mode under SEM which can be used for qualitative and quantitative chemical analyses as shown in peaks on a continuous background. The peak positions are specific to a particular element, and the height is proportional to its relative abundance. The classification with respect to the Ca/Si ratio is used to distinguish hydrates rich in C-S-H, rich in calcium hydroxide, and monosulfate (AFm)[3], which is shown in Table 5. A SE image of CNF added concrete is shown in Fig. 4.18, where a fiber is wrapped by hydration products. The EDS analysis is performed along the fiber, and the spectrums are showing on the right. Based on the Ca/Si ratio, the hydration product is mainly C-S-H.

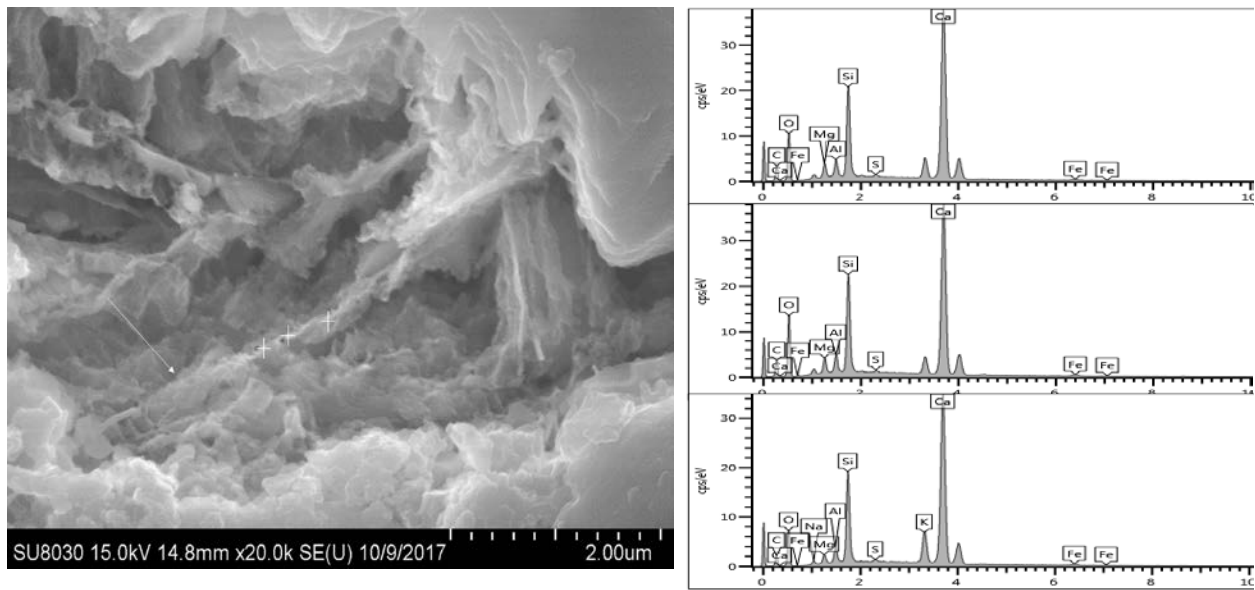


Figure 4.18. SEM of CNF added concrete sample

Table 4.3. Ca/Si ratio of the major hydrated phases

Hydration Products	Ca/Si Ratio
Calcium-Silicate-Hydrate (C-S-H)	0.8~2.5
Calcium Hydroxide (CH)	≥ 10
Ettringite (AFm)	≥ 4.0

The chemical composition within ITZ is in particular interest, where the MOE is increased by the addition of CNFs. The chemical composition in the ITZ as well as in bulk cement paste is determined by using EDS line analysis, which plots relative concentration of selected elements along a line. The atomic ratio of calcium to silicon is calculated on each line of the five lines drawn from the aggregate to the bulk paste.

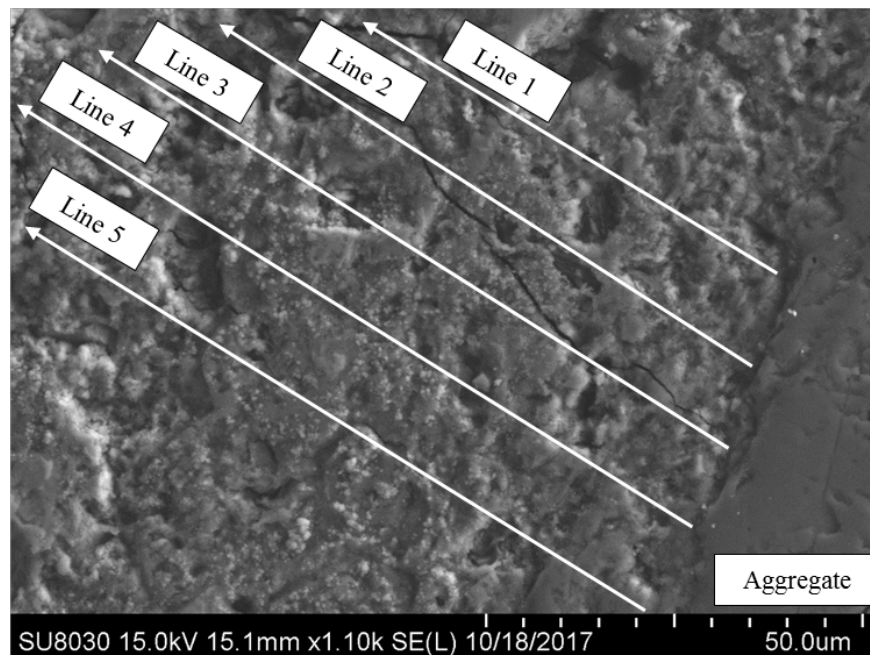


Figure 4.19. Line protocol of SEM/EDS results on an area containing aggregate, ITZ, and bulk paste.

For Ca/Si ratio collected from SEM/EDS, the range between 1.2 and 2.3 is defined as typical C-S-H gel as proposed by Hewlett [14]. The EDS results with this line protocol are shown in Fig 14 for concrete with and without CNFs. From the EDS results on plain concrete shown in Fig 14(a), it is found that the Ca/Si ratio tends to be above the range of 1.2-2.3 near the aggregate (approximately 20-40 μm range next to the aggregate), with a large variation along these line, which is a sign of the presence of CH and a likely porous structure. After a distance of around 40 μm , the Ca/Si ratio tends to fall in the range of 1.2-2.3 indicating a C-S-H rich region and the chemical compositions is much more uniform. It provides clear evidence that the interfacial transitional zone (ITZ) exists and its width varies from 20 to 40 μm . This finding corresponds to previous research on ITZ of normal concrete.

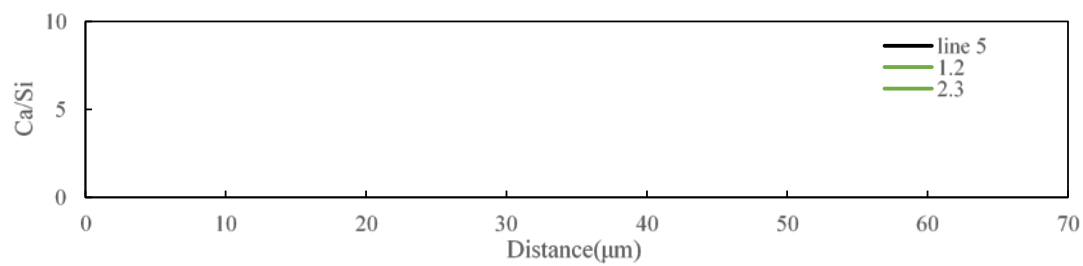
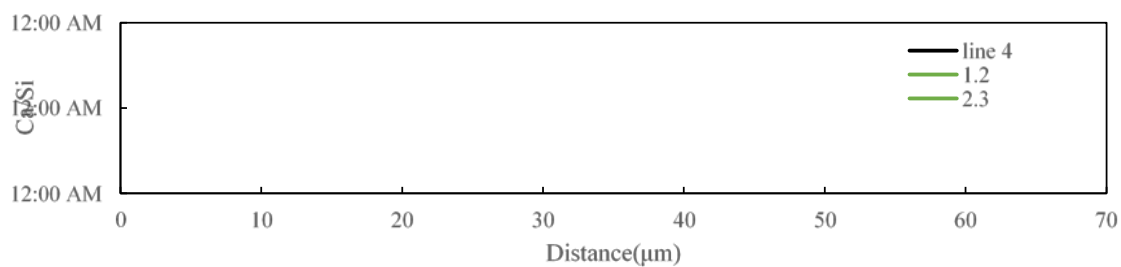
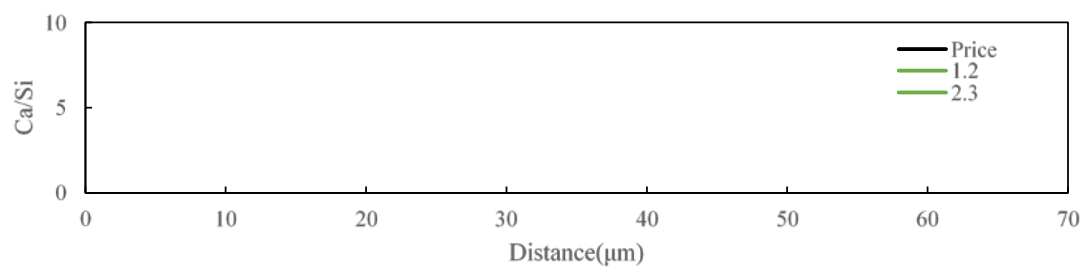
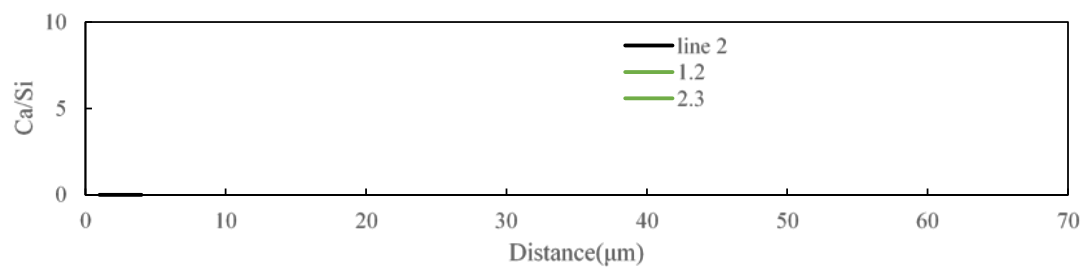
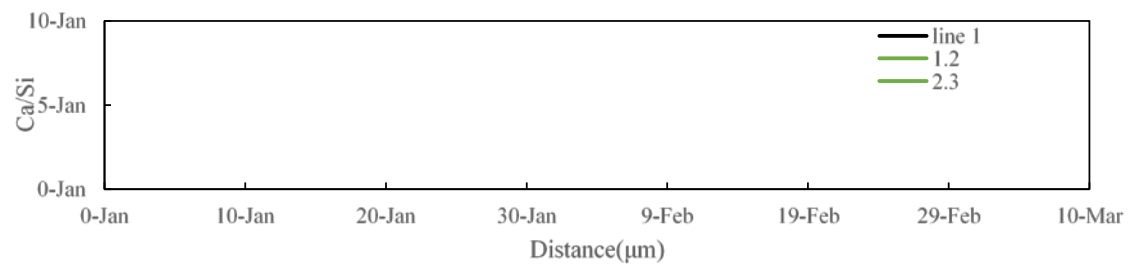
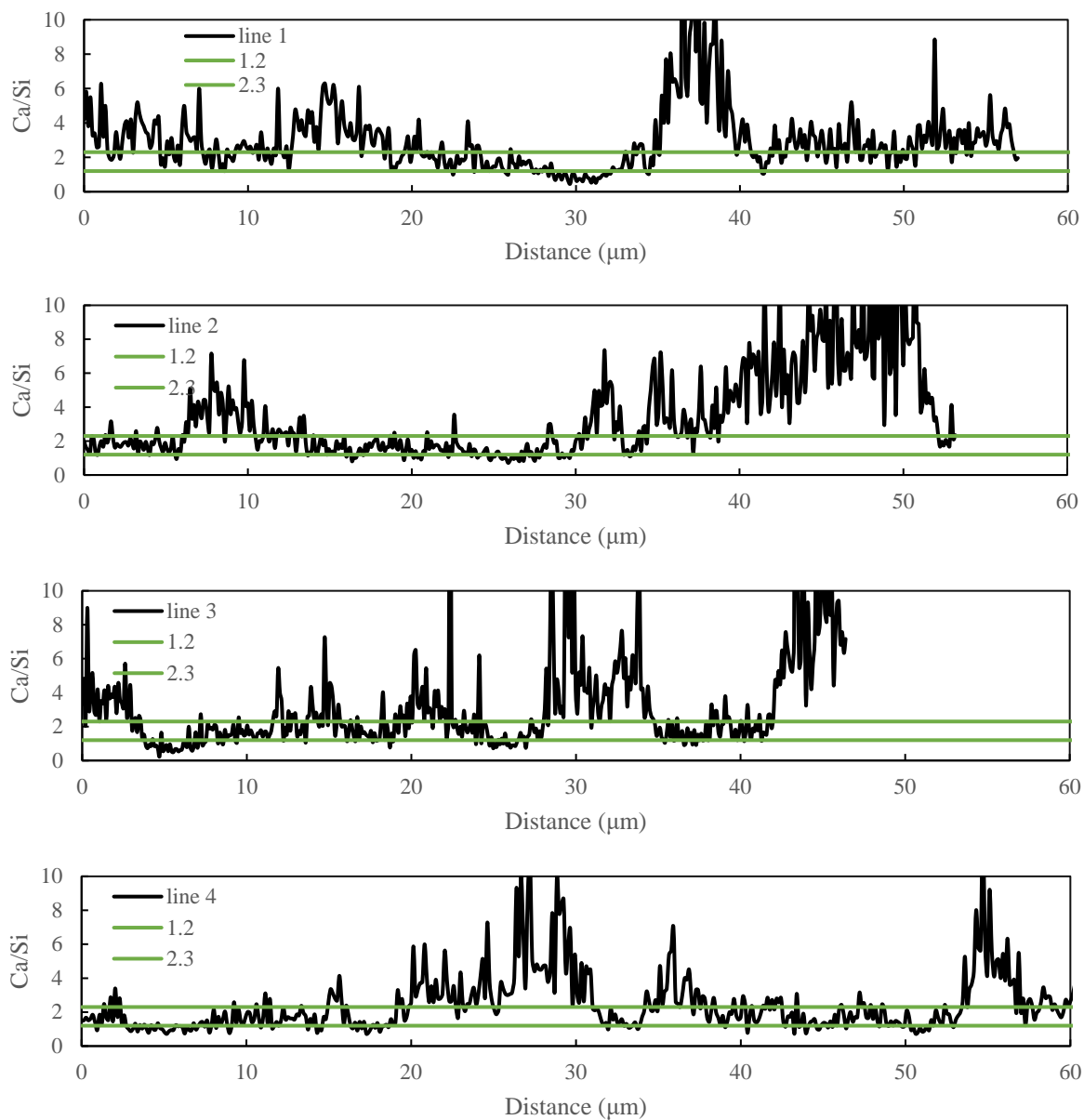


Figure 4.20. Ca/Si ratio of plain concrete



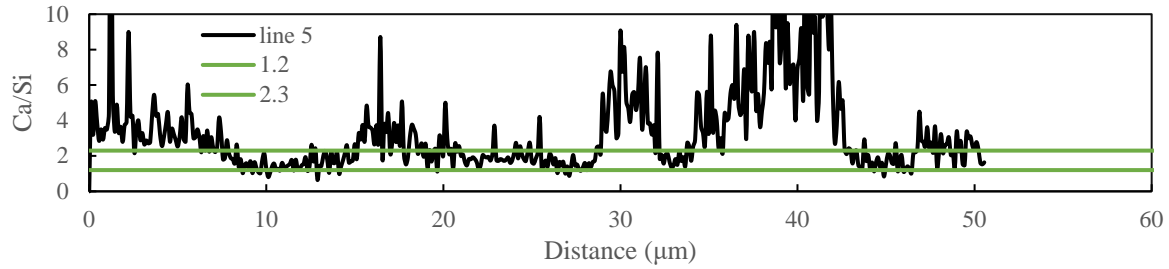


Figure 12. Ca/Si ratio of CNF added concrete

For CNF added concrete, the Ca/Si has a distinct phenomenon compared to plain concrete. There is no clear band between bulk paste and aggregate with respect to Ca/Si ratio. From the beginning of the line, the Ca/Si has a tendency to fall in the range of 1.2-2.3 immediately, as shown in Fig 14(b). Research has shown that lower Ca/Si ratio at ITZ often indicates a higher amount of C-S-H gel, and lower amount of CH existing in the cement matrix [15][16]. A statistical study has been performed on the area 20 μm next to aggregate for 5 lines analyzed for each sample. The probability is plotted versus the value of Ca/Si ratio for both samples and it clearly shows the CNF sample has a high probability for low Ca/Si ratio with a peak at 2.0 (Fig. 15). In addition, the shape of the curve for the CNF sample is narrower than the control sample, which indicates a uniform microstructure compared to control sample.

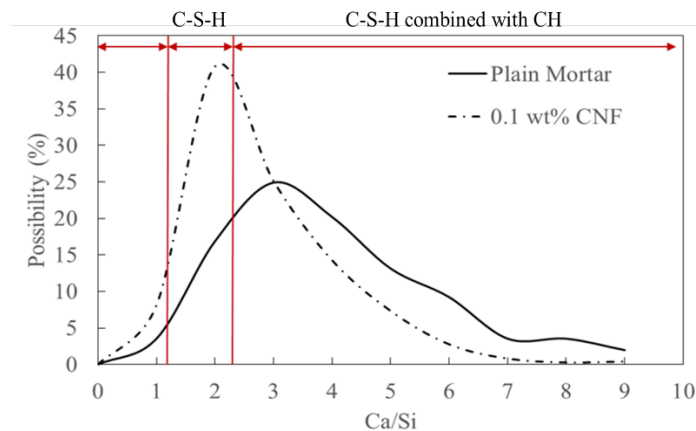


Figure 13. The probability of Ca/Si within ITZ (20 μm next to aggregate) of concrete specimens from SEM/EDS

4.4 Summary

The improvement of Young's modulus in mortars and concrete is more pronounced from the mechanical tests, indicating a potential enhancement at ITZ. The AFM-QNM technique was successfully used for the first time to investigate the ITZ between cement paste and aggregates. It was found that the average MOE is increased by 36.7% for ITZ in cement mortar, and by 55% to 63% in concrete. The microstructure of ITZ was also examined with SEM/EDS, where Ca/Si ratio is measured with line-scanning protocol. Based on the imaging results CNF reinforced ITZ shows a lower Ca/Si ratio, which indicates a higher amount of C-S-H phase than plain ITZ. Since C-S-H gel is mainly responsible for the stiffness and strength, ITZ with CNFs exhibits a higher Young's modulus.

Reference

- [1] K.L. Scrivener, A.K. Crumbie, P. Laugesen, The Interfacial Transition Zone (ITZ) Between Cement Paste and Aggregate in Concrete, *Interface Sci.* 12 (2004) 411–421. doi:10.1023/B:INTS.0000042339.92990.4c.
- [2] J.P. Ollivier, J.C. Maso, B. Bourdette, Interfacial transition zone in concrete, *Adv. Cem. Based Mater.* 2 (1995) 30–38. doi:https://doi.org/10.1016/1065-7355(95)90037-3.
- [3] J. Tragardh, Microstructural features and related properties of self-compacting concrete, *1st Int. Rilem Symp. Self Compact. Concr.* 7 (1999) 175–186.

- [4] D.P. Bentz, P.E. Stutzman, E.J. Garboczi, Experimental and simulation studies of the interfacial zone in concrete, *Cem. Concr. Res.* 22 (1992) 891–902.
doi:[https://doi.org/10.1016/0008-8846\(92\)90113-A](https://doi.org/10.1016/0008-8846(92)90113-A).
- [5] P. Duan, Z. Shui, W. Chen, C. Shen, Effects of metakaolin, silica fume and slag on pore structure, interfacial transition zone and compressive strength of concrete, *Constr. Build. Mater.* 44 (2013) 1–6. doi:<https://doi.org/10.1016/j.conbuildmat.2013.02.075>.
- [6] C. Tasdemir, M.A. Tasdemir, F.D. Lydon, B.I.G. Barr, Effects of silica fume and aggregate size on the brittleness of concrete, *Cem. Concr. Res.* 26 (1996) 63–68.
doi:[https://doi.org/10.1016/0008-8846\(95\)00180-8](https://doi.org/10.1016/0008-8846(95)00180-8).
- [7] W. Zhu, J.J. Hughes, N. Bicanic, C.J. Pearce, Nanoindentation mapping of mechanical properties of cement paste and natural rocks, *Mater. Charact.* 58 (2007) 1189–1198.
doi:<https://doi.org/10.1016/j.matchar.2007.05.018>.
- [8] W.-W. Li, W.-M. Ji, Y.-C. Wang, Y. Liu, R.-X. Shen, F. Xing, Investigation on the Mechanical Properties of a Cement-Based Material Containing Carbon Nanotube under Drying and Freeze-Thaw Conditions, *Materials (Basel)*. 8 (2015) 8780–8792.
doi:[10.3390/ma8125491](https://doi.org/10.3390/ma8125491).
- [9] W. Li, S. Kawashima, J. Xiao, D.J. Corr, C. Shi, S.P. Shah, Comparative investigation on nanomechanical properties of hardened cement paste, *Mater. Struct.* 49 (2016) 1591–1604. doi:[10.1617/s11527-015-0597-3](https://doi.org/10.1617/s11527-015-0597-3).
- [10] J. Xu, D.J. Corr, S.P. Shah, Nanomechanical investigation of the effects of nanoSiO₂ on C–S–H gel/cement grain interfaces, *Cem. Concr. Compos.* 61 (2015) 7–17.

doi:<https://doi.org/10.1016/j.cemconcomp.2015.04.011>.

- [11] P. Trtik, J. Kaufmann, U. Volz, On the use of peak-force tapping atomic force microscopy for quantification of the local elastic modulus in hardened cement paste, *Cem. Concr. Res.* 42 (2012) 215–221. doi:<https://doi.org/10.1016/j.cemconres.2011.08.009>.
- [12] B. V. Derjaguin, V.M. Muller, Y.P. Toporov, Effect of contact deformations on the adhesion of particles, *J. Colloid Interface Sci.* 53 (1975) 314–326. doi:10.1016/0021-9797(75)90018-1.
- [13] J.I. Goldstein, D.E. Newbury, P. Echlin, D.C. Joy, A.D. Romig, C.E. Lyman, C. Fiori, E. Lifshin, Electron optics, in: *Scanning Electron Microsc. X-Ray Microanal.*, Springer, 1992: pp. 21–68.
- [14] P.C. Hewlett, *Lea's Chemistry of Cement and Concrete*, Butterworth-Heinemann, Oxford, 2003.
- [15] S. Erdem, A.R. Dawson, N.H. Thom, Influence of the micro- and nanoscale local mechanical properties of the interfacial transition zone on impact behavior of concrete made with different aggregates, *Cem. Concr. Res.* 42 (2012) 447–458. doi:<https://doi.org/10.1016/j.cemconres.2011.11.015>.
- [16] K. Wu, H. Shi, L. Xu, G. Ye, G. De Schutter, Microstructural characterization of ITZ in blended cement concretes and its relation to transport properties, *Cem. Concr. Res.* 79 (2016) 243–256. doi:<https://doi.org/10.1016/j.cemconres.2015.09.018>.

Chapter 5

Simulation of CNT Reinforced Cementitious Material Considering the ITZ

5.1 Introduction

From the previous chapters, the CNFs is found to be able to enhance the ITZ of concrete material, which could significantly improve the MOE in the macro scale. The reinforcement effect of ITZ is modeled with finite element method in this chapter. An analytical model of hot mix asphalt mixtures was developed with the consideration of the ITZ, where a finite element analyses is used to examine the stress distribution at ITZ and the model was successfully validated by the experiment results[1]. Another study has proposed a micromechanical analytical

model to predict the modulus of asphalt concrete, and the ITZ was treated as springs with constant stiffness[2]. Unlike the model that has neglected the thickness of the ITZ in the matrix, the new model will consider both the thickness and the modulus of ITZ to account for the effect of CNFs. Since the thickness of ITZ is extremely small when comparing with the size of aggregate, it is hard to build the FEM model with both phases in terms of mesh generation and accuracy control. Therefore, a new model is developed by Prof. Zhu using the effective aggregate. By validated with laboratory experiment results, the model is proven to be valid to simulate the ITZ's effect, linking the real interfacial condition to the macro-mechanical behavior of concrete. The input parameters for the model includes the MOE of ITZ with or without the nano reinforcement from the AFM-QNM test, as well as the MOE of the mortars and the aggregates.

5.2 Model Development

To simulation the ITZ's effect on concrete properties, two commonly used models have been considered. One is the interphase model, which treats ITZ as a thin layer of a third material with specific thickness. However, it is difficult to build a FEM model considering its tiny size compared to the other two phases (aggregate and bulk paste). For example, during the finite element simulation, the stiffness matrix often becomes nearly degenerate when parts of the surface are separated by a rather small thickness, meanwhile the singularity from the element stiffness matrix and mesh generation within ITZ are also difficult to deal with. The second model is the spring layer interface model, where the matrix and the aggregate are connected with springs without considering the thickness of the interface. While the spring layer model is easy to be implemented in the analytical and numerical model, it doesn't represent the real condition at

the interface with discontinuous displacement between bulk paste and the aggregates. For the spring layer interface model, at the interface, we have

$$\sigma_{rr}^{(1)} = \sigma_{rr}^{(2)} = k_r [u_r] \quad (1)$$

$$\sigma_{r\theta}^{(1)} = \sigma_{r\theta}^{(2)} = k_\theta [u_\theta] \quad (2)$$

where the superscript (1) and (2) indicate matrix and inclusion, respectively. Therefore, $\sigma_{rr}^{(1)}$ and $\sigma_{r\theta}^{(1)}$ are the stress exerted by the matrix on the inclusion, while $\sigma_{rr}^{(2)}$ and $\sigma_{r\theta}^{(2)}$ are the stress exerted by the inclusion on the matrix. $[u_r]$ and $[u_\theta]$ are the displacement jumps. k_r and k_θ are the interface spring constants. Apparently, for the spring layer interface model, the stresses are still continuous across the interface while the displacements may be discontinuous (the displacements are continuous only under the case of perfect contact, namely $k_r = k_\theta = \infty$). Thus, the interfacial effect can be interpreted as the displacement jumps, and the jumps in normal and tangential displacement are proportional to the stress components. This model is quite easy to be implemented in the analytical and numerical simulation. However, the constants k_r and k_θ are quite difficult to be measured directly, which makes it unrealistic to link the interface spring constants to the real interfacial condition.

By combining both models, the “effective aggregate model” is firstly presented to better incorporate the ITZ into the finite element model of concrete behaviors. To consider the interface effect, the concept of “effective aggregate” is put forward, namely, the Young’s modulus and Poisson’s ratio for each aggregate particle are replaced by an effective Young’s modulus, and effective Poisson’s ratio, in which the effect of thickness and the Young’s modulus of ITZ is

taken into account in an averaged manner. The detail information for numerical simulation can be found in our paper[3], and it is discussed in the following sections.

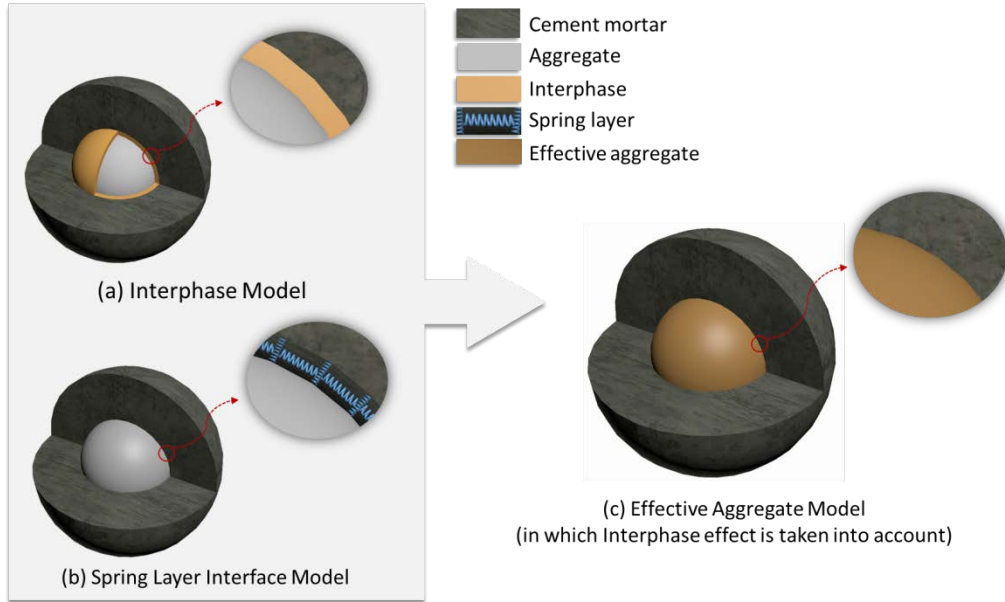


Figure 5.1. Models describing the interfacial zone

5.2.1 Spherical symmetry

A spherical inclusion (aggregate) of radius a consisting of homogeneous isotropic material 2, is embedded in the unbounded isotropic matrix 1. The inclusion is surrounded by a thin flexible interphase 3 coating of thickness h and Young's properties K_3 (bulk modulus) and G_3 (shear modulus), see Fig. 5.1(a). The radial displacements and stresses for above three-phase spherically symmetric Young's problem can be in the form

$$u_r^{(j)} = A_j r + B_j / r^2 \quad (3)$$

$$\sigma_{rr}^{(j)} = 3K_j A_j - 4G_j B_j / r^3 \quad (j=1, 2, 3) \quad (4)$$

where A_j, B_j ($j=1, 2, 3$) are unknown constants; G_1, K_1 are the bulk modulus and shear modulus of matrix, G_2, K_2 are the bulk modulus and shear modulus of inclusion, G_3, K_3 are the bulk

modulus and shear modulus of interphase. To get the relationship between interface parameter (k_r) and interphase parameter (K_3 , G_3 , and h), considering Eqs. (3) and (4), the radial displacement jump $[u_r]$ can be approximated by

$$[u_r] = u_r^{(3)}(a+h) - u_r^{(3)}(a) \cong \left(\frac{\partial u_r^{(3)}}{\partial r} \right)_{r=a} h = (A_3 - 2B_3/a^3)h$$

$$A_3 = \frac{A_2(4G_3 + 3K_2)}{3K_3 + 4G_3} \quad (5)$$

$$B_3 = \frac{3A_2 a^3 (K_1 - K_2)}{3K_3 + 4G_3}$$

Since

$$\sigma_{rr}^{(2)}(a) = 3K_2 A_2 - 4G_2 B_2 / r^3 = k_r [u_r] \quad (6)$$

we can immediately derive

$$k_r = \frac{3K_2(3K_3 + 4G_3)}{t(4G_3 + 9K_2 - 6K_3)} \quad (7)$$

5.2.2 Axisymmetry

Similarly, the displacements and stresses for three-phase spherically axisymmetric problem (see

Fig.5.1(a)) can be in the form

$$u_r^{(j)} = \beta \left[12\nu_j A_j \rho^2 + 2B_j + 2(5 - 4\nu_j)C_j / \rho^3 - 3D_j / \rho^5 \right] r P$$

$$u_\theta^{(j)} = \beta \left[(7 - 4\nu_j)A_j \rho^2 + B_j + 2(1 - 2\nu_j)C_j / \rho^3 + D_j / \rho^5 \right] r P \quad (8)$$

$$\sigma_{rr}^{(j)} = 2G_j \beta \left[-6\nu_j A_j \rho^2 + 2B_j - 4(5 - \nu_j)C_j / \rho^3 + 12D_j / \rho^5 \right] P$$

$$\sigma_{r\theta}^{(j)} = 2G_j \beta \left[(7 + 2\nu_j) A_j \rho^2 + B_j + 2(1 + \nu_j) C_j / \rho^3 - 4D_j / \rho^5 \right] \quad \&$$

$$P = \frac{1}{2} (3 \cos^2 \theta - 1), \quad \rho = r / a \quad (j=1,2,3)$$

where ν_1, ν_2 , and ν_3 are the Poisson's ratios for matrix, inclusion, and interphase, respectively.

A_j, B_j, C_j, D_j are undetermined constants. To get the relationship between interface parameter (k_θ) and interphase parameter (K_3, G_3 , and h), considering Eq.(8), the radial displacement jump $[u_\theta]$ can be approximated by

$$\begin{aligned} [u_\theta] &= u_\theta^{(3)}(a+h) - u_\theta^{(3)}(a) \cong \left(\frac{\partial u_\theta^{(3)}}{\partial r} \right)_{r=a} h \\ &= \beta \left[3(7 - 4\nu_3) A_3 + B_3 - 4(1 - 2\nu_3) C_3 - 4D_3 \right] h \quad \& \end{aligned} \quad (9)$$

According to Eqs.(2), (8), and (9), we can get

$$k_\theta = \frac{2G_2 G_3 M}{2G_2 M + G_3 N} \quad (10)$$

$$M = (7 + 2\nu_2) A_2 + B_2, \quad N = (7 - 16\nu_2) A_2 - B_2$$

in which A_2 , and B_2 can be obtained from the following linear equations (Eq.(11) is basically from Eq. (8) according to the traction continuity equations (2-3))

$$2(5 - \nu_1) C_1 - 6D_1 - 3\nu_2 g A_2 + g B_2 = 1 \quad (11)$$

$$-2(1 + \nu_1) C_1 + 4D_1 + (7 + 2\nu_2) g A_2 + g B_2 = 1$$

$$-2(5-4\nu_1)C_1+3D_1+12\nu_2(1-e)A_2+2(1+2e)B_2=2$$

$$-2(1-2\nu_1)C_1-D_1+[7-4\nu_2+2m(7+2\nu_2)]A_2+(1+2m)B_2=1$$

$$e=\frac{3K_2(1-2\nu_2)}{2ak_r(1+\nu_2)}, \quad g=\frac{G_2}{G_1}, \quad m=\frac{G_2}{ak_\theta}$$

5.2.3 Effective aggregate considering interphase effect

Since the interphase does have its own stiffness, the Young's modulus and Poisson's ratio for aggregate particles E_f and ν_f can be replaced by an effective Young's modulus $\hat{E}_f^o(s)$ and Poisson's ratio $\hat{\nu}_f^o(s)$, in which the interfacial effect can be taken into account in an averaged manner.

Based on Achenbach and Zhu, the spring layer interface model can be considered into twofold[4], see Fig. 5.2. When an inclusion with a linear distribution of vertical spring layer (constant k_r per unit length) is subjected to radial stresses $\sigma_r=1$ (see Fig. 5.2(a)), the radial displacement at $r=a$ (a is the radius of the inclusion) can be written as

$$u_r = \frac{1-(\nu_2)^2}{E_2} \left(1 - \frac{\nu_2}{1-\nu_2} \right) a + \frac{1}{k_r} \quad (12)$$

If the inclusion is substituted by an effective media with an effective Young's modulus $\hat{E}_f^o(s)$ and Poisson's ratio $\hat{\nu}_f^o(s)$, and the spring layer effect is taken into account, we would have the effective radial displacement at $r=a$ (\bar{u}_r) of the same form as Eq. (12) but without the last term.

Considering $u_r = \bar{u}_r$, we have

$$\frac{1-(\nu_2^0)^2}{E_2^0} \left(1 - \frac{\nu_2^0}{1-\nu_2^0}\right) a = \frac{1-(\nu_2)^2}{E_2} \left(1 - \frac{\nu_2}{1-\nu_2}\right) a + \frac{1}{k_r} \quad (13)$$

Similarly, we consider an inclusion is distributed by a linear circumferential body forces

$f_\theta = -4r$, which are equilibrated by circumferential shear stresses $\sigma_{r\theta} = a^2$ at $r = a$, see Fig.

5.2(b). The shear stresses $\sigma_{r\theta}$ are applied by a layer of circumferential interface constants k_θ .

Since the circumferential displacements for the inclusion plus spring layer equals the displacements of the effective inclusion, the following equation can be obtained

$$\frac{a^3}{2G_2} + \frac{a^3}{k_\theta} = \frac{a^3}{2G_2^0} \quad (14)$$

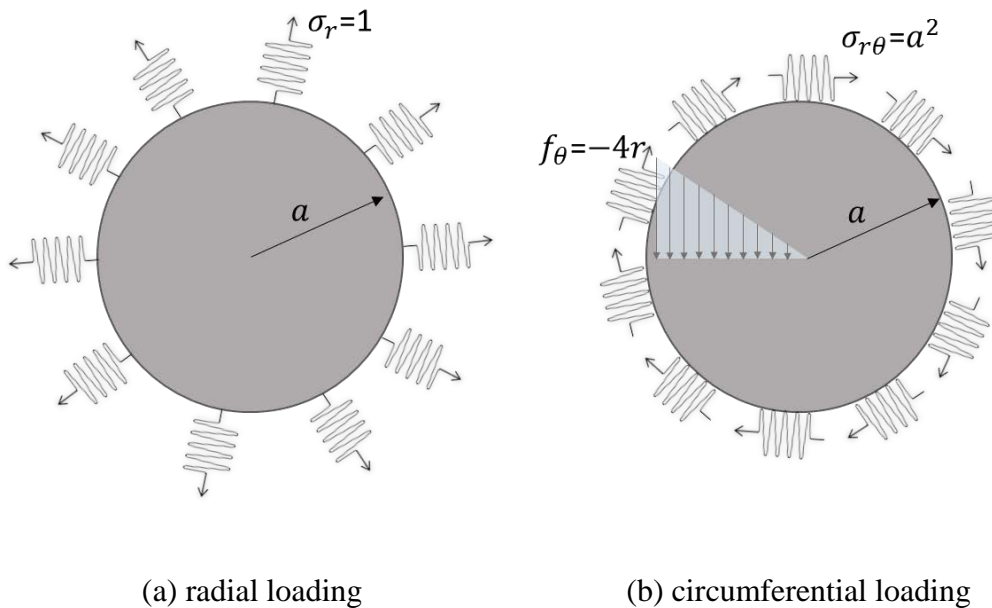


Figure 5.2. Calculation of effective Young's modulus and effective Poisson's ratio of inclusion based on spring layer interface model

Combined Eq.(13) and Eq.(14), the effective Young's modulus and the effective Poisson's ratio of inclusion are in the form

$$\frac{\nu_2^0}{E_2^0} = \frac{2ak_\theta G_2 (1 + \nu_2^0)}{ak_\theta + 2G_2} \quad (15)$$

$$\nu_2^0 = 0.5 - \frac{ak_\theta G_2 (1 + \nu_2^0)}{ak_\theta + 2G_2} \left[\frac{1}{2G_2} (1 - 2\nu_2) + \frac{1}{ak_r} \right]$$

Substitute Eqs. (7) and (10) into Eq.(15), we can finally get the effective Young's modulus and the effective Poisson's ratio of aggregate in the expression of interphase parameters (K_3 , G_3 , and t), see Eq.(16)

$$\frac{\nu_2^0}{E_2^0} = \frac{4aG_2^2 G_3 M (1 + \nu_2^0)}{aG_2 G_3 M + 2G_2 (2G_2 M + G_3 N)} \quad (16)$$

$$\nu_2^0 = 0.5 - \frac{2aG_2^2 G_3 M (1 + \nu_2^0)}{2aG_2 G_3 M + 2G_2 (2G_2 M + G_3 N)} \left[\frac{1}{2G_2} (1 - 2\nu_2) + \frac{h(4G_3 + 9K_2 - 6K_3)}{a3K_2 (3K_3 + 4G_3)} \right]$$

Clearly, based on Eq. (16), we can easily incorporate the real interfacial condition (the Young's properties K_3 and G_3 and the thickness of ITZ, which can be measured from nano-scale metrology technique, see sub-section 3.3) into the numerical model.

$$\frac{\nu_2^0}{E_2^0} = \frac{4aG_2^2 G_3 M (1 + \nu_2^0)}{aG_2 G_3 M + 2G_2 (2G_2 M + G_3 N)}$$

$$\nu_2^0 = 0.5 - \frac{2aG_2^2 G_3 M (1 + \nu_2^0)}{2aG_2 G_3 M + 2G_2 (2G_2 M + G_3 N)} \left[\frac{1}{2G_2} (1 - 2\nu_2) + \frac{h(4G_3 + 9K_2 - 6K_3)}{a3K_2 (3K_3 + 4G_3)} \right]$$

where G_1 and K_1 are the bulk modulus and shear modulus of matrix; G_2 and K_2 are the bulk modulus and shear modulus of inclusion (aggregate); and G_3 and K_3 are the bulk modulus and shear modulus of interphase. In addition, a is the radius of the aggregate and h is the thickness of

the ITZ. With the developed model, the real interfacial condition can be incorporated (G_3 , K_3 and h) into the calculation. And these factors will be measured from AFM-QNM technique as mentioned in Chapter 4.

5.3 FEM Simulation Process

The simulation process is shown in Fig 5.3, and will be discussed in the following subsections.

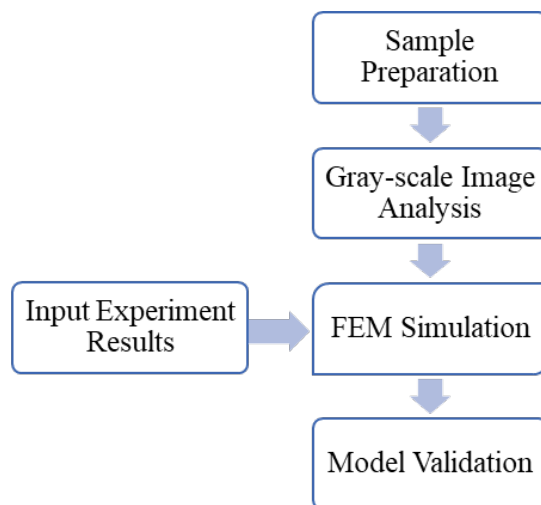


Figure 5.3 FEM simulation process

5.3.1 Sample Preparation

Mortar and Concrete cylindrical samples with the dimension of 100mm x 200mm are prepared with type I Ordinary Portland Cement. Natural rounded river sand is used as fine aggregate.

Locally available limestone is used as coarse aggregate with the same gradation shown in Fig 3.6. To validate the developed finite element model, two sets of concrete samples are prepared with different amounts of coarse aggregate. 0.1 wt% of CNT (to cement) is added into mortar sample and concrete sample 2. The mix proportions for all samples are shown in Table 5.1.

Superplasticizer (SP) is added in all control mixes, and the same amount of SP existed in CNF

solution to aid the dispersion. All samples are cured in humidity room (100% humidity, 23 °C) for 28 days before testing.

Table 5.1 Mix proportions of cylindrical samples

	water/ cement	sand/ cement	coarse aggregate/ cement	SP/ cement	CNF/ cement
Plain Mortar	0.51	2.46	None	0.40%	None
Mortar+CNF	0.51	2.46	None	0.40%	0.10%
Concrete Sample 1	0.51	2.46	1.5	0.40%	None
Concrete Sample 2	0.51	2.46	3.5	0.40%	None
Sample 2+CNF	0.51	2.46	3.5	0.40%	0.10%

5.3.2 Gray-scale image analysis

To consider the interfacial effect in the finite element modelling, real distribution of coarse aggregates is obtained via gray-scale image processing. It is used to quantify the coarse aggregate and micro-pores along the longitudinal half section of the cylindrical samples, which is based on the intensity of pixels after converting RGB image to gray-scale image. The processing is shown in Fig 5.4, where sample 1 and sample 2 have different amount of aggregates. The area of each aggregate is calculated based on the number of pixels within its outline, and the perimeter of each aggregate is measured along the length of the outline. Thus, the equivalent radius of each aggregate can be obtained through either the area equivalence principle or perimeter equivalence principle.



Figure 5.4. Gray-scale image processing

5.3.3 Input experiment results

To successfully simulate the Young's modulus of cement concrete with the developed model, input parameters such as Young's modulus of cement mortar, aggregate and ITZ are based on test results. The detailed description of test procedure and test results for each parameter is listed below.



Figure 5.5 Input parameters for the simulation model

(1) Modulus and Poison's ratio of coarse aggregate

The modulus and Poison's ratio of coarse aggregate are the necessary parameters in the developed finite element model, which are indicated as K_2 and G_2 . The MOE of limestone aggregate is measured via Ultrasonic Pulse Velocity Testing (UPVT).

UPVT works in a nondestructive way by measuring the velocity of the ultrasound waves traveling through the specimen. The wave is generated by a transmitter from one end, and received by a receiver at the other end, see Fig. 5.5. After getting the velocity of the ultrasound wave, the Young's modulus of limestones used in the concrete sample can be obtained through Eq.(17) immediately

$$E_2 = \frac{V^2 \rho (1+\nu)(1-2\nu)}{1-\nu} \quad (17)$$

where V is the ultrasound wave velocity, ρ is the density of the aggregate and measured as 2550 kg/m³, and ν is Poison's ratio and assumed to be 0.1 for limestone aggregate.

To ensure the accuracy, five large aggregates (larger than 19mm) were sieved from the same stockpile of coarse aggregate for cement concrete samples. Each aggregate was polished to form two parallel surfaces. Both the transmitter and the receiver were 1 Hz. After testing, the average value of five samples' Young's modulus is 54.9 GPa.

(2) Compression test of cylindrical samples

Compression tests are performed with cylindrical mortar and concrete samples, according to ASTM C469. To determine the Young's modulus of the specimen, a compressometer is used to measure the deformation during compression. The compression result is shown in Table 5.2.

Table 5.2 Compression Test Results for Mortar and Concrete Cylinders

	Compressive Strength (MPa)	Young's Modulus (GPa)
Plain Mortar	40.6	27.3
Mortar+CNF	43.1	36.5
Concrete Sample 1	39.2	33.1
Concrete Sample 2	46.7	35.7
Sample 2+CNF	50.5	46.2

(3) AFM-QNM for Young's modulus at ITZ

PeakForce™ QNM™ (Quantitative Nanomechanical Property Mapping) is used to characterize the ITZ of concrete samples with or without CNF, and the procedure is discussed in Chapter 4. The Young's modulus of ITZ for plain concrete is 17 GPa, while the Young's modulus of ITZ for CNF added concrete is 24 GPa.

5.3.4 Finite element simulation

The images processed in Fig.5.6(a) were imported into the FEM software ABAQUS as geometric models of the concrete cylinder specimens with a size of 10cm × 20cm (4in × 8in), to ensure the consistency of geometry between the specimens and the numerical model. The input parameters for numerical simulation are summarized in Table 5.3. Here, the data of Young's

modulus of aggregate, cement mortar with and without CNF, ITZ with and without CNF are all collected from Section 5.3. It is mentioned by Garboczi and Bentz[5] that the ITZ had the same Poisson's ratio as the bulk paste but a smaller Young's modulus, therefore, the Poisson's ratios of mortar and ITZ are all set as 0.3. The thickness of ITZ in cement-based materials is usually around 10-40 μm . For instance, Zimbelmann (1985) found the thickness of ITZ ranged from 10 μm to 30 μm [6]. Ollivier et al. thought that there was 15 μm to 20 μm around the aggregates. Based on the above literatures, the thickness of ITZ is set as 20 μm in the numerical simulation[7].

Table 5.3. Input parameters for numerical simulation

Components	Young's modulus (GPa)	Poisson's ratio	Density (kg/m³)
Coarse Aggregate	54.9	0.1	2550
Plain Mortar	27.3	0.3	2261
Mortar+0.1 wt% CNF	36.5	0.3	2261
ITZ (without CNF)	17	0.3	—
ITZ (with 0.1 wt% CNF)	24	0.3	—

By applying Eq. (16) to consider the interfacial effect, the effective Young's modulus (\tilde{E}_2) and the effective Poisson's ratio ($\tilde{\nu}_2$) of each aggregate should be calculated. It is noticed that Eq. (16) contains the parameter a , which is the equivalent radius of aggregate. Since each aggregate has different size, therefore, based on Eq. (16), each aggregate would have different effective

Young's modulus and effective Poisson's ratio. To figure out each aggregate's effective Young's properties, the aggregates are numbered (See Fig. 5.6(a)), and the corresponding equivalent radius and effective Young's parameters are calculated according to Eq. (16). Here, Tables 5.4 and 5.5 list the partial aggregates' Young's parameters. Aggregates with different effective Young's modulus are represented in different color as shown in Fig.5.6(b).



Figure 5.6 Aggregate profile in FEM model

Table 5.4 Young's parameters of partial aggregates in Sample 1

Aggregate Number	Area (cm ²)	$\tilde{\alpha}_a$ (cm)	\tilde{E}_2 (GPa)	$\tilde{\nu}_2$	Perimeter (cm)	$\tilde{\alpha}_p$ (cm)	\tilde{E}_2 (GPa)	$\tilde{\nu}_2$
61	1.09	0.576	52.4	0.08	4.04	0.761	52.5	0.08
62	0.03	0.588	47.7	0.10	0.66	0.644	48.0	0.10
63	0.65	0.100	52.1	0.08	3.25	0.105	52.2	0.08
64	0.08	0.455	49.6	0.09	1.19	0.517	50.3	0.09
65	0.95	0.157	52.3	0.08	4.30	0.189	52.5	0.08
66	0.35	0.550	51.6	0.08	2.36	0.685	51.8	0.08

67	0.05	0.332	48.7	0.10	0.80	0.377	48.8	0.09
68	0.08	0.124	49.6	0.09	1.12	0.128	50.1	0.09

Table 5.5 Young's parameters of partial aggregates in Sample 2

Aggregate Number	Area (cm ²)	$\tilde{\alpha}_a$ (cm)	Plain				+0.1 wt% CNF					
			\tilde{E}_2 (GPa)	$\tilde{\nu}_2$	\tilde{E}_2 (GPa)	$\tilde{\nu}_2$	Perimeter (cm)	$\tilde{\alpha}_p$ (cm)	\tilde{E}_2 (GPa)	$\tilde{\nu}_2$	\tilde{E}_2 (GPa)	$\tilde{\nu}_2$
81	0.08	0.162	49.8	0.09	51.4	0.08	1.24	0.198	50.4	0.09	51.8	0.08
82	0.29	0.303	51.4	0.08	52.3	0.08	2.16	0.344	51.7	0.08	52.5	0.08
83	0.13	0.205	50.5	0.09	51.8	0.08	1.44	0.229	50.8	0.08	52.0	0.08
84	0.09	0.169	49.9	0.09	51.5	0.08	1.15	0.183	50.1	0.09	51.6	0.08
85	1.14	0.603	52.4	0.08	52.9	0.07	4.99	0.794	52.7	0.08	53.0	0.07
86	0.08	0.156	49.6	0.09	51.3	0.08	1.18	0.188	50.2	0.09	51.7	0.08
87	0.15	0.218	50.7	0.09	51.9	0.08	1.49	0.237	50.9	0.08	52.0	0.08

Boundary conditions and loads of the simulation are in consistent with those of the compression tests. Moreover, the models are all meshed by free triangular elements (3-node linear plane strain triangle). After the FEM analysis, all unknowns at the nodes of the boundary are derived, then the Young's modulus of cement concrete, E_{eff} , can be determined by $E_{eff} = \bar{\sigma} / \bar{\varepsilon}$, where $\bar{\sigma}$ and $\bar{\varepsilon}$ are the average strain and stress obtained from the numerical simulation, respectively.

5.4 Results and Discussion

5.4.1 Comparison and validation

The calculated Young's modulus of concrete samples by numerical simulation and the test results are listed in Table 5.6.

Table 5.6 Comparison of Young's modulus between simulation results and test results

Sample	E_{eff} (GPa)	Measured E_0 (GPa)
Sample 1 (Plain Concrete 1)	32.82	33.1
Sample 2 (Plain Concrete 2)	37.40	35.7
Sample 3 (Concrete 3+0.1wt%CNF)	45.33	46.2

From Table 5.6, it can be confirmed that the effective aggregate model with ITZ considered can lead the simulation results to agree well with the test data, which indicates the high accuracy of FEM modeling we have established. Furthermore, the effect of ITZ on the Young's property of concrete is unneglectable, and the effective aggregate model proposed in this study is validated. Both the simulation (E_{eff}) and test results (E_0) in Table 5.6 show that the Young's modulus of concrete is increased with the addition of CNFs effectively.

However, it should be noted that the little difference between predicted and test value could be possibly caused by limitation of UPVT method for measuring the Young's Modulus of aggregate, and the assumption that the thickness of ITZ is 20 μ m. In other words, the actual thickness of ITZ should vary with the microstructural feature of aggregate and cement

mortar[8][9][10], and thus the assumption of the uniform thickness of ITZ may cause the difference between simulation and test data.

Figure 5.7 gives the internal distribution of the von Mises stress and strain in both sample 2 and sample 3 under the compression test. It was found that both cases have almost the same highest local stress, however, the local stress amplification (ratio of the highest to lowest local stress) for sample 3 (with CNFs) was much lower than the stress amplification in sample 2 (no CNFs). Meanwhile, aggregates in sample 2 bear much higher stress than the aggregates in sample 3. And especially, the stress concentration around the defects (air void here) is more distinct in sample 2 than in sample 3. In addition, the vertical strains in the cement concrete without CNFs is also higher than in the cement concrete with the addition of CNFs. All above suggest that cement concrete with stiffer ITZ is more likely to resist damage once the specimen is loaded. This may be because aggregate-ITZ system has better stress transfer capability due to the high Young's modulus of ITZ, which makes it more compatible with the deformation of the cement mortar and leads to higher toughness. Besides, the existence of CNF in cement mortar can further balance the stress and strain distribution between aggregates and cement mortar by improving the Young's modulus of cement mortar.

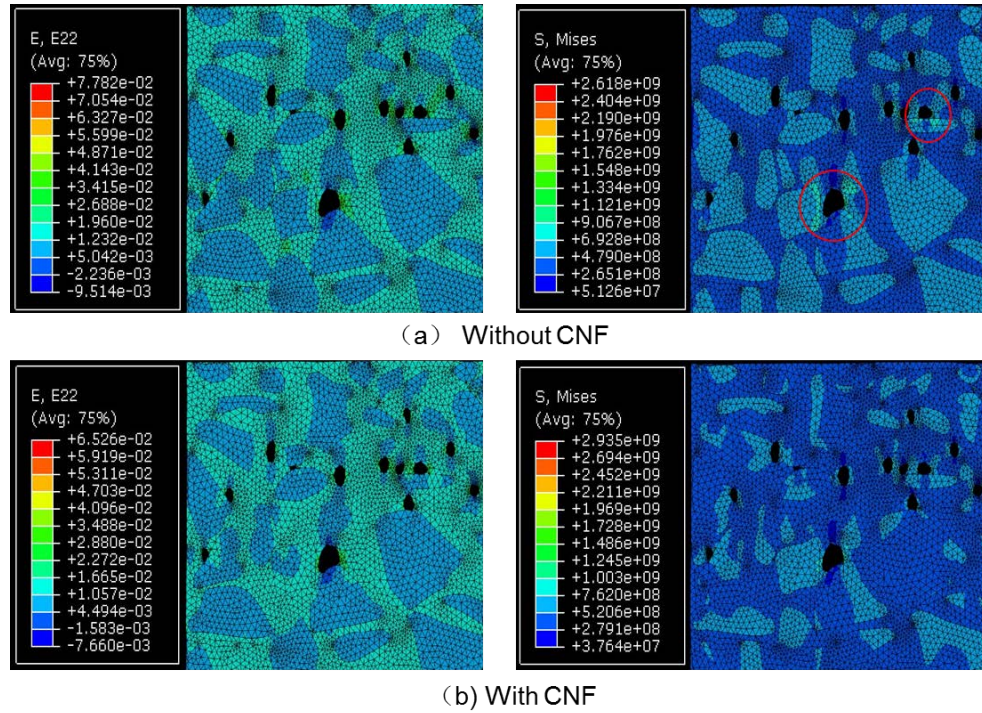


Figure 5.7. Von Mises stress contours and strain contours for FEM simulations of cement concrete (a) without or (b) with CNFs

5.4.2 Influencing factor analysis

In order to find out the factors which may affect the simulation of Young's modulus for the cement concrete, a further study was conducted, where the effect of Young's modulus of aggregate and cement mortar, as well as the properties of ITZ on the Young's modulus of cement concrete was analyzed via FEM simulation.

(1) Young's Modulus of Aggregate

The Young's modulus of cement mortar (E_1) is set as 36.5GPa during the analysis. The effect of Young's modulus of aggregate (E_2) on E_{eff} under 5 different Young's modulus of ITZ (E_3) is firstly analyzed, and the ITZ thickness is set as 20 μ m (See Fig.5.8). It is obviously seen that E_{eff}

increases with the increase of E_2 , and the higher E_3 is, the more obvious the growing trend of E_{eff} is. In addition, there are little difference among E_{eff} in the case of $E_3=15, 25$ & 50 GPa. As E_3 is correlated with the contact strength between aggregate and cement mortar to some degree, the higher E_3 is, the less significant its effect of weakening the Young's modulus of concrete is, which can explain the little difference mentioned above. Moreover, with the effect of E_3 getting less obvious, the influence of E_2 on E_{eff} is more remarkable, which leads to the change in the growing trend.

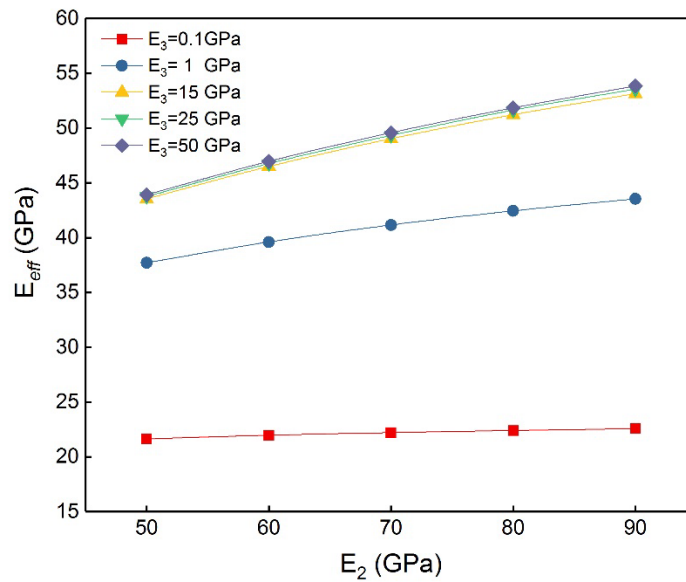


Figure 5.8. Effect of Young's modulus of aggregate on that of concrete under different ITZ Young's modulus

Besides, to find out the effect of ITZ thickness on the variation of E_{eff} with E_2 , 5 values of ITZ thickness (h), $10\sim 50\mu\text{m}$ (intervals $10\mu\text{m}$), are chosen and analyzed in the case of $E_3=0.1$ GPa (Fig.5.9(a)) and 25 GPa (Fig.5.9(b)) respectively. Comparing the two figures, the effect of ITZ

thickness on E_{eff} is pretty more significant than that of E_2 on E_{eff} when $E_3=0.1\text{GPa}$, but in the case of $E_3=25\text{GPa}$, the condition is on the opposite. It is easily known that ITZ with a very small Young's modulus (e.g. 0.1GPa) has a more significant weakening effect on the Young's modulus of concrete when its thickness is larger. However, when the Young's modulus of ITZ is large enough (e.g. 25GPa), the thickness of ITZ has little impact on E_{eff} .

To sum up, the Young's modulus of concrete is positively correlated with the Young's modulus of aggregate, and the effect of Young's modulus of aggregate is more significant when the effect of ITZ properties is less obvious.

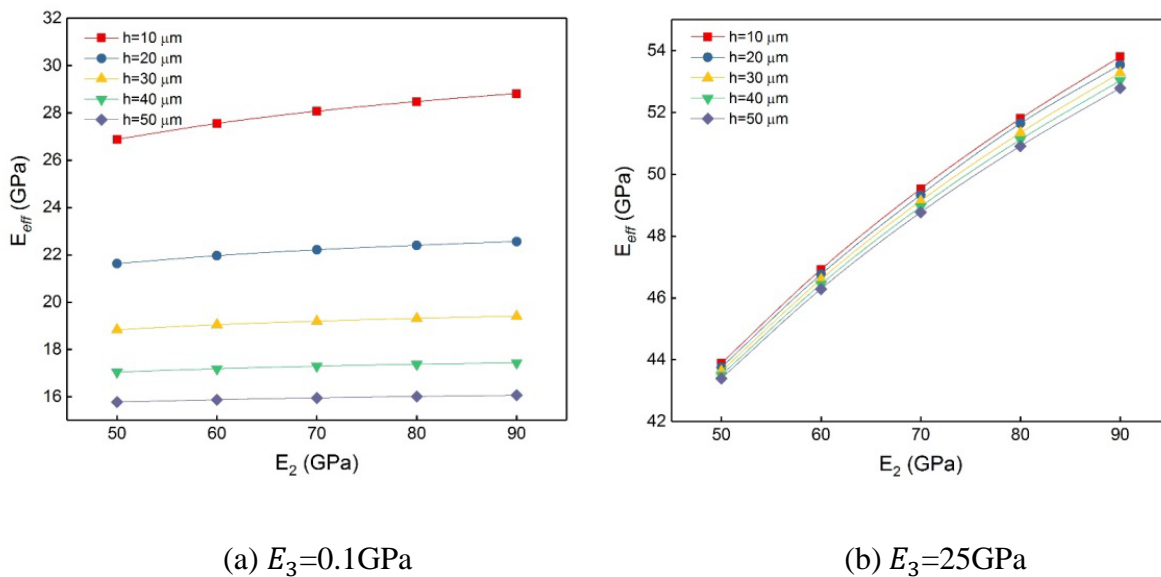


Figure 5.9. Effect of Young's modulus of aggregate on that of concrete under different ITZ thickness

(2) Young's Modulus of Cement Mortar

The Young's modulus of aggregate is set as 50GPa . There are also 5 kinds of ITZ Young's modulus and 5 kinds of ITZ thickness taken into consideration respectively. In each case, the

Young's modulus of cement mortar is controlled as the only variable from 50 to 90GPa (intervals 10GPa).

As shown in Fig.5.10 ($h=20\ \mu\text{m}$), the Young's modulus of concrete E_{eff} is positively correlated with the Young's modulus of cement mortar E_1 . Fig.5.11(a) shows that increasing the thickness of ITZ in the case of $E_3=0.1\text{GPa}$ can significantly affect the impact of E_1 on E_{eff} . However, when E_3 is getting larger (See Fig.5.11(b), $E_3=25\text{GPa}$), the effect of ITZ thickness seems to be no longer noticeable.

It is obvious that the Young's modulus of cement mortar is one of the main factors affecting the concrete's Young's modulus, since cement concrete is mainly consisted of aggregate and cement mortar. Thus, a similar conclusion can be drawn that when the weakening effect of ITZ on concrete is getting more ignorable, namely the thickness getting smaller or the ITZ's Young's modulus getting larger, the effect of Young's modulus of cement mortar is more remarkable.

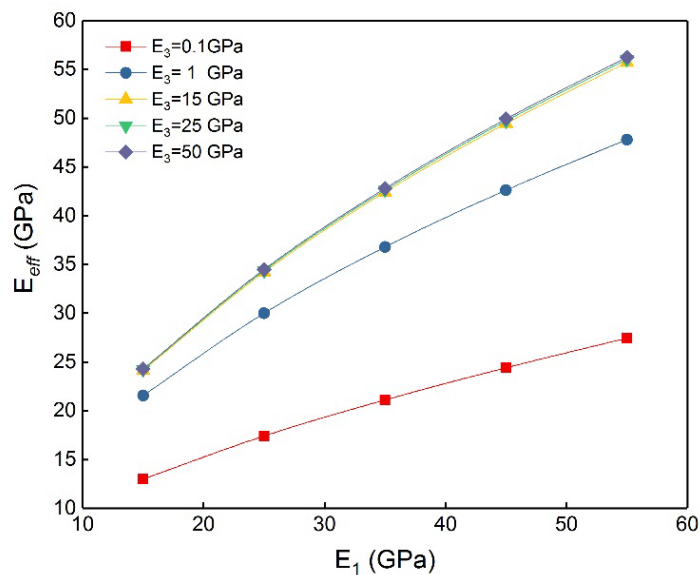


Figure 5.10. Effect of Young's modulus of cement mortar on that of concrete under different ITZ thickness

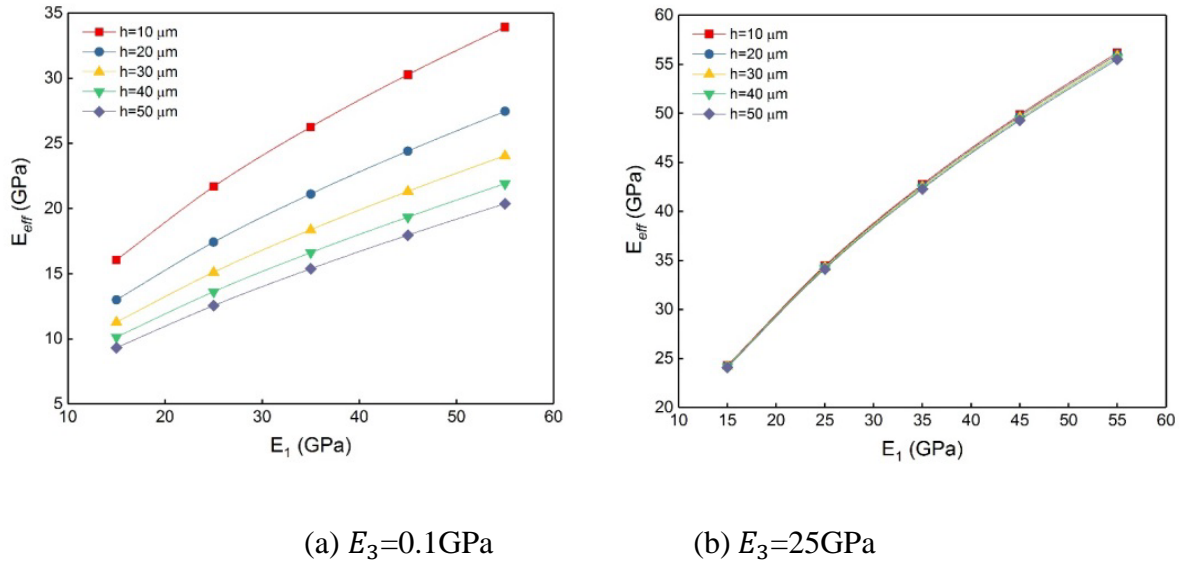


Figure 5.11. Effect of Young's modulus of cement mortar on that of concrete under different ITZ thickness

(3) Properties of ITZ

The Young's modulus of aggregate and cement mortar are set as 50GPa and 36.5GPa based on test results, respectively. And 7 Young's modulus of ITZ, i.e. 0.1GPa, 1GPa, 5-45GPa (intervals 10GPa), are used to conduct the analysis with the consideration of 5 different ITZ thickness. It can be clearly seen from Fig. 5.12 that the Young's modulus of ITZ has significant effect on that of concrete before it reaches 35GPa, however when it is larger than 35GPa, the Young's modulus of concrete maintains stable. In addition, from Fig.5.12, we can find that with the increase of ITZ thickness, the differences among the curves are getting larger.

This situation is consistent with that in Fig.5.8 and Fig.5.10. To be specific, when the Young's modulus of ITZ is relatively low, its effect on E_{eff} is more noticeable than the effect of Young's

modulus of aggregate and cement mortar. That is to say, the ITZ properties are more important and considerable for the Young's properties of concrete when it works as a rather weak chain between aggregate and cement mortar. Thus, the effects of the thickness of ITZ are more significant when its Young's modulus is small enough, while the effects become negligible when E_3 is getting larger as the ITZ is strengthening.

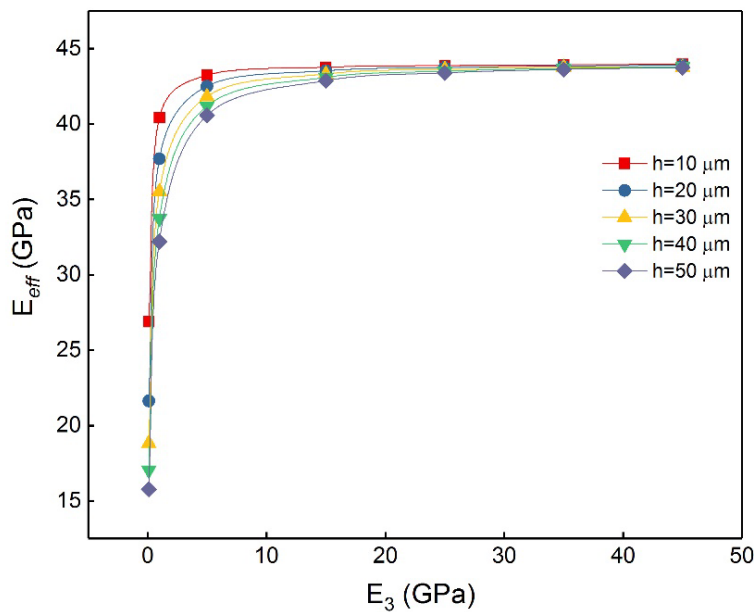


Figure 5.12. Effect of properties of ITZ on Young's modulus of concrete

Fig.5.13 shows the strain contours for FE simulations of cement concrete, where the distribution of strain is significantly changing with the thickness and Young's modulus of ITZ. It can be found that with the increase of ITZ thickness or with the decrease of Young's modulus of ITZ, the effective aggregates would experience higher local tensile strains. However, the strain distribution in cement concrete will become more homogeneous when a stiff ITZ exists between the cement mortar and aggregate. The mechanical properties of cement concrete largely depend on the stress/strain transfer from the stiff inclusions (coarse aggregate) into the soft matrix

(cement paste). Since ITZ as a transition zone plays an important role in the efficiency of load transfer, it is no doubt that the properties of ITZ will significantly affect the macro-mechanical behavior of cement concrete. Apparently, a weak ITZ does not allow an effective stress transfer across its thickness, and it therefore leads to the diminution in the load carry capacity of the concrete, irrespective of the load type.

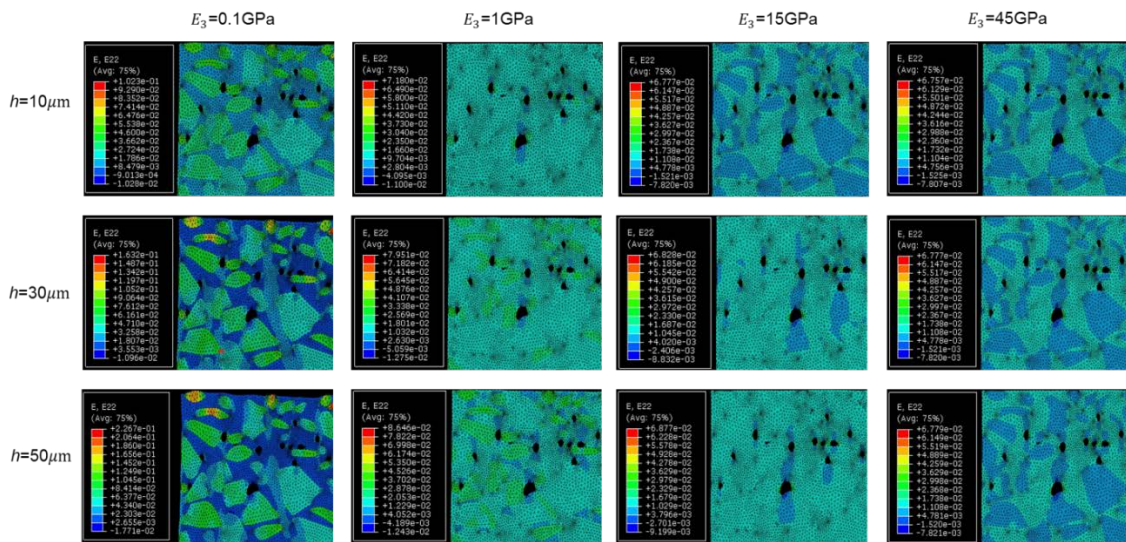


Figure 5.13. Strain contours for FE simulations of cement concrete with different ITZ properties

5.5 Summary

A new effective aggregate model is proposed in this chapter to link the real interfacial condition to the macro-mechanical behavior of cement concrete. The simulation results of concrete model with and without CNF can agree well with the test results, which indicates that the ITZ effect should be considered when implementing the numerical simulation. Despite the changes in ITZ properties, the Young's modulus of cement concrete is positively correlated with both of the Young's modulus of aggregates and cement mortar. However, the effect of both two components

on concrete Young's modulus can be less noticeable than that of ITZ when the latter one is rather weak. The effect of ITZ properties, namely its Young's modulus and thickness, on the elastic properties of cement concrete is proved to be significant. Based on the sensitivity analysis, it is found that a larger thickness of ITZ with a relatively low Young's modulus has more noticeable effect on the Young's modulus of concrete, and the effect of ITZ thickness is negligible when the Young's modulus of ITZ is large enough. Moreover, when ITZ thickness is kept as a constant, the increase in Young's modulus of ITZ can lead to an increase in the Young's modulus of cement concrete, for it can work as a stronger chain between cement mortar and aggregates.

Reference

- [1] B. Huang, X. Shu, G. Li, L. Chen, Analytical modeling of three-layered HMA mixtures, *Int. J. Geomech.* 7 (2007) 140–148.
- [2] X. Zhu, Z. Yang, X. Guo, W. Chen, Modulus prediction of asphalt concrete with imperfect bonding between aggregate–asphalt mastic, *Compos. Part B Eng.* 42 (2011) 1404–1411. doi:<https://doi.org/10.1016/j.compositesb.2011.05.023>.
- [3] S.P.S. X. Zhu, Y. Gao, Z. Dai, D. J. Corr, Effect of interfacial transition zone on the Young's modulus of carbon nanofiber reinforced cement concrete, *Cem. Concr. Res.* (n.d.).
- [4] J.D. Achenbach, H. Zhu, Effect of interfacial zone on mechanical behavior and failure of fiber-reinforced composites, *J. Mech. Phys. Solids.* 37 (1989) 381–393. doi:[https://doi.org/10.1016/0022-5096\(89\)90005-7](https://doi.org/10.1016/0022-5096(89)90005-7).
- [5] E.J. Garboczi, D.P. Bentz, Analytical formulas for interfacial transition zone properties,

- Adv. Cem. Based Mater. 6 (1997) 99–108. doi:[https://doi.org/10.1016/S1065-7355\(97\)90016-X](https://doi.org/10.1016/S1065-7355(97)90016-X).
- [6] R. Zimbelmann, A contribution to the problem of cement-aggregate bond, *Cem. Concr. Res.* 15 (1985) 801–808. doi:[https://doi.org/10.1016/0008-8846\(85\)90146-2](https://doi.org/10.1016/0008-8846(85)90146-2).
- [7] J.P. Ollivier, J.C. Maso, B. Bourdette, Interfacial transition zone in concrete, *Adv. Cem. Based Mater.* 2 (1995) 30–38. doi:[https://doi.org/10.1016/1065-7355\(95\)90037-3](https://doi.org/10.1016/1065-7355(95)90037-3).
- [8] K.L. Scrivener, A.K. Crumbie, P. Laugesen, The Interfacial Transition Zone (ITZ) Between Cement Paste and Aggregate in Concrete, *Interface Sci.* 12 (2004) 411–421. doi:[10.1023/B:INTS.0000042339.92990.4c](https://doi.org/10.1023/B:INTS.0000042339.92990.4c).
- [9] A. Leemann, B. Münch, P. Gasser, L. Holzer, Influence of compaction on the interfacial transition zone and the permeability of concrete, *Cem. Concr. Res.* 36 (2006) 1425–1433. doi:<https://doi.org/10.1016/j.cemconres.2006.02.010>.
- [10] Y. Gao, G. De Schutter, G. Ye, Z. Tan, K. Wu, The ITZ microstructure, thickness and porosity in blended cementitious composite: Effects of curing age, water to binder ratio and aggregate content, *Compos. Part B Eng.* 60 (2014) 1–13. doi:<https://doi.org/10.1016/j.compositesb.2013.12.021>.

Chapter 6

Mechanism of CNT's Reinforcing Effect

6.1 Introduction

CNTs are proven to be able to increase the MOE of cement-based materials as well as autogenous shrinkage and shrinkage cracking. Particularly, the SEM/EDS test finds a lower Ca/Si ratio on the interface due to the addition of the nanomaterials, which indicates a modification on the hydration products. These phenomena are directly related to the hydration of cement, which could play an important role on microstructural development. Water molecules keep penetrate the cement grains through the hydration process. The formation of the hydration products, namely calcium-silicate-hydrate (CSH) gel and calcium hydroxide (CH), is accompanied by a heat release. Many studies have shown that the addition of nanomaterials into cement-based material influences the hydration reaction of cement to a certain extent, which may be reflected in the following two aspects. First, the nanomaterials themselves have the ability to participate in chemical reactions. For example, the widely investigated nano silica can react with

CH, forming more CSH which is the strength carrying structure of cement[1][2][3][4]. Second, owing to the large surface area and aspect ratio, nanomaterials may play as a nucleation site and thereby stimulate nucleation reactions of hydration phases on their surface[5][6][7]. In this chapter, although CNTs hardly exhibited reaction activity themselves, the nucleation effect could not be excluded completely. Another hypothesis is that the CNT changes the nanostructure of CSH, helping the alignment of the crystals in nanoscale. Therefore, in this chapter, the characterization of CNT's effect on cement hydration is conducted to explain the mechanism of its reinforcing effect on various properties.

Several characterization techniques have been conducted including the Fourier-transform infrared spectroscopy (FTIR), semi-adiabatic calorimetry and X-ray diffraction (XRD). The experiment is conducted with the collaboration with Prof. Tao[8], and the test procedure and the test results are presented in the following subsections.

6.2 FTIR Test

Fourier transform infrared spectroscopy (FTIR) is a common research method and an effective tool in material science, which has been successfully used to characterize the hydration products. It is used to obtain an infrared spectrum of absorption of the solid sample, showing the complex chemistry involved in the cement hydration.

The FTIR analysis is performed using a Thermo Nicolet Nexus 870, and the testing range of wavenumbers is 400–4000 cm^{-1} , which belongs to the middle infrared region. In this study, the tablet method is used to prepare the samples for FTIR analysis. The sample to be tested is evenly mixed with potassium bromide (KBr) powder in the ratio 1:100. Then, the mixed powder is

ground continuously for 5 min to ensure even dispersion of the sample in the potassium bromide powder and that the particles of the mixed powder could reach a certain fineness. A tablet is made from the mixed and finely ground powder, which was then tested. The test resolution used is 8.0 cm^{-1} , and each sample is scanned 64 times.

6.2.1 FTIR spectra of several fundamental samples

Figure 1 shows the FTIR spectra of CNT sample, indicating that no obvious vibration absorption peak appears in the FTIR spectra of the CNTs, and the individual small peaks in the spectra originated from the background. Therefore, it could be conducted that the absorption peaks in the spectra of the subsequent FTIR test basically obtained from the cement-based material itself.

CNTs do not exert any excessive interference influence on the spectra.

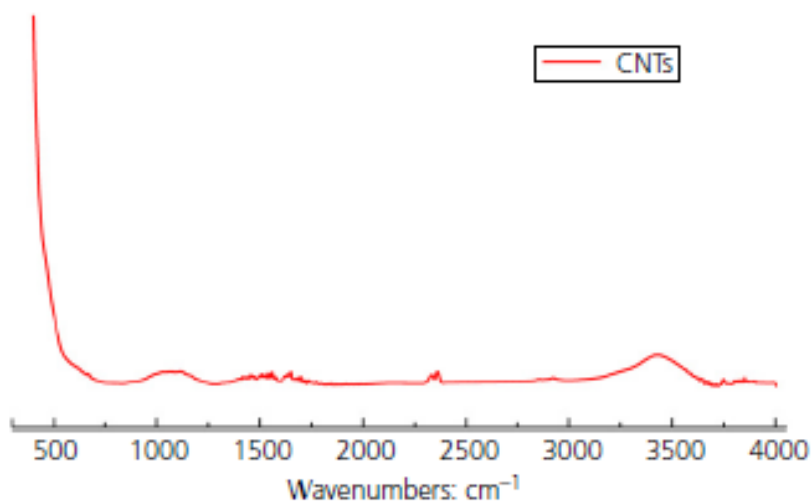


Figure 6.1 FTIR spectra of CNT sample

Figure 6.2 shows the FTIR spectra of the dry cement (cement clinker) sample. Figure 6.2 shows that the absorption peaks of cement clinker mainly concentrate in the range $500\text{-}1000\text{ cm}^{-1}$, absorption peaks of the mineral composites alite ($3\text{CaO}\cdot\text{SiO}_2$, C_3S) and belite ($2\text{CaO}\cdot\text{SiO}_2$, C_2S)

dominated by silicon-oxygen vibration, are mainly reflected in the regions near 922 and 519 cm^{-1} , respectively. However, the absorption peak near 1148 cm^{-1} corresponds to the silicon-oxygen vibration of sulfate, SO_4^{2-} [9][10][11].

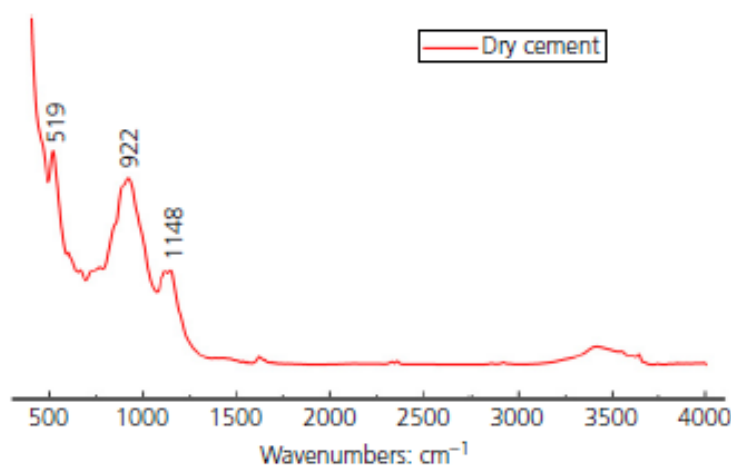


Figure 6.2 FTIR spectra of dry cement

Fig. 6.3 shows the FTIR spectra of the 7d plain cement sample. When cement hydration lasts for 7 days, the composition of the hydration products of the hardened cement paste is relatively stable, so that the absorption peaks in Fig. 6.3 basically reflect the FTIR spectra of typical Portland cement after hydration. Herein, the peaks at 3643, 3437 and 1651 cm^{-1} correspond to the hydroxyl vibrations of portlandite ($\text{Ca}(\text{OH})_2$) and the stretching and bending modes of water of crystallization, respectively. The set of absorption peaks in the range 1420-1480 cm^{-1} and the absorption peak at 874 cm^{-1} correspond to the vibrations of carbonate, CO_3^{2-} ; the peak at 1117 cm^{-1} can be attributed to the sulfur-oxygen (S-O) vibrations of sulfate, SO_4^{2-} ; and the peaks at 980, 516 and 463 cm^{-1} correspond to the vibration of silicon-oxygen in the gel[11]. The above-mentioned characteristic peaks can be identified readily after decades of research and analysis.

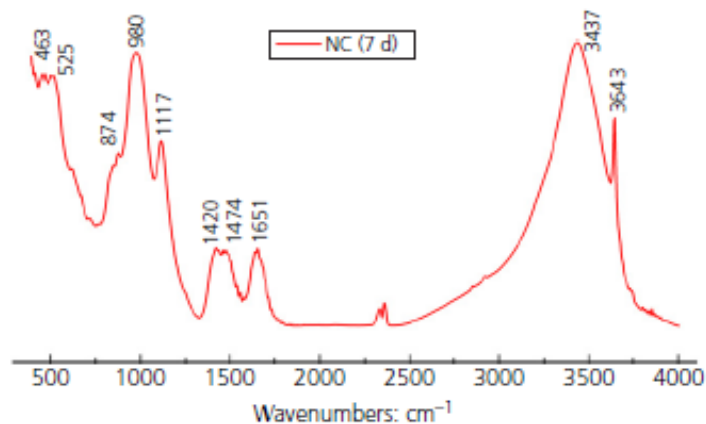


Figure 6.3. FTIR spectra of plain cement at 7 days

Modern cement chemistry[12][13][14] considers that all silicon-oxygen tetrahedrons in the main minerals (C_3S and C_2S) of Portland cement clinker are present as an isolated island shape, that is, Q_0 . This Q_0 can form C-S-H gel after hydration, and then the polymerization degree of the tetrahedron increases gradually to form Q_1 and Q_2 . Comparative analysis of Fig. 6.3 and 6.4 indicates that the peaks corresponding to silicon-oxygen vibrations shift from low wave number to high wave number during the hydration reactions of C_3S and C_2S , which results in the formation of C-S-H gel; that is, the transformation process of the silicon-oxygen tetrahedron occurs from Q_0 to Q_2 . This phenomenon has also been mentioned in other literature reports[11][15]. During the polymerization of silicon-oxygen tetrahedrons, the most obvious peak at 922 cm^{-1} , corresponding to silicon-oxygen vibrations, is considered as an example (Fig. 6.4), which shifts from wave number 922 cm^{-1} to the high wave number 980 cm^{-1} . This is an indicative phenomenon because the hydration process of cement-based materials can be reflected by this phenomenon. For Portland cement, the starting period is about 8-12 hours after the mixing with water.

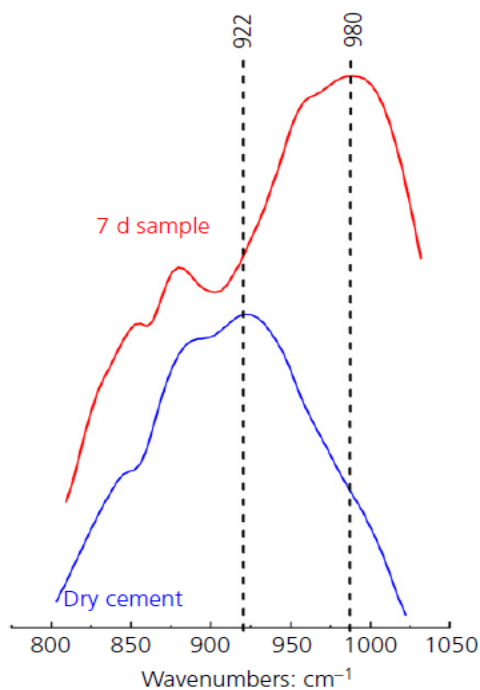


Figure 6.4 Shift of silicon-oxygen stretching vibration

6.2.2 FTIR study on cement paste mixed with SP

In the thesis, the comparative experiments have been performed using the blank cement sample and the cement sample with superplasticizer (SP) to verify the shift phenomenon of the above-mentioned characteristic peaks. The theoretical basis can be summarized as follows: according to the product description, the SP used in the thesis exhibited some retarding effect towards the gelation process, so that the retarding phenomenon should be reflected in the shift of the characteristic peak at 922 cm^{-1} . The w/c ratio for paste sample is 0.4, and the SP is added during mixing at the dosage of 0.4 wt% (to cement). After mixing, the samples are sealed for 8 h at $20\text{ }^{\circ}\text{C}$. Then, FTIR tests are performed every hour until 12 h of age.

Fig. 6.5 shows the FTIR spectra of the cement pastes with or without SP. Herein, the FTIR test is performed on the range of 400-4000 cm^{-1} ; however, the region where the characteristic peaks are located (Fig. 6.5), namely, 800-1025 cm^{-1} , is cut out for the convenience of comparison. The results show that, for the samples at the ages of 8 and 9 hours, the silicon-oxygen stretching vibration peak of the two groups of samples still remain at 920 cm^{-1} , which is the same as the peak value of the dry cement. Thus, the silicon-oxygen tetrahedrons in the hardened cement paste still exist in the form of monomers instead of dimers or polymers until the samples have been aged for 8 and 9 hours. For the plain cement, this status changes when the age reaches 10 hours. At the age of 10 hours, the characteristic peaks of plain cement begin to shift, and the peak values for 10, 11 and 12 were 945, 948, and 983 cm^{-1} , respectively. In contrast, there is no significant change for the sample with SP during the period 8-11 hours, and the characteristic peaks begin to shift at the age of 12 hours. The above-mentioned comparison clearly indicates that the polymerization degree of silicon-oxygen tetrahedrons in the C-S-H gel at this period can be intuitively reflected in the FTIR spectra. Based on FTIR results, the hydration of plain cement paste is delayed for approximately 2 hours due to the addition of SP.

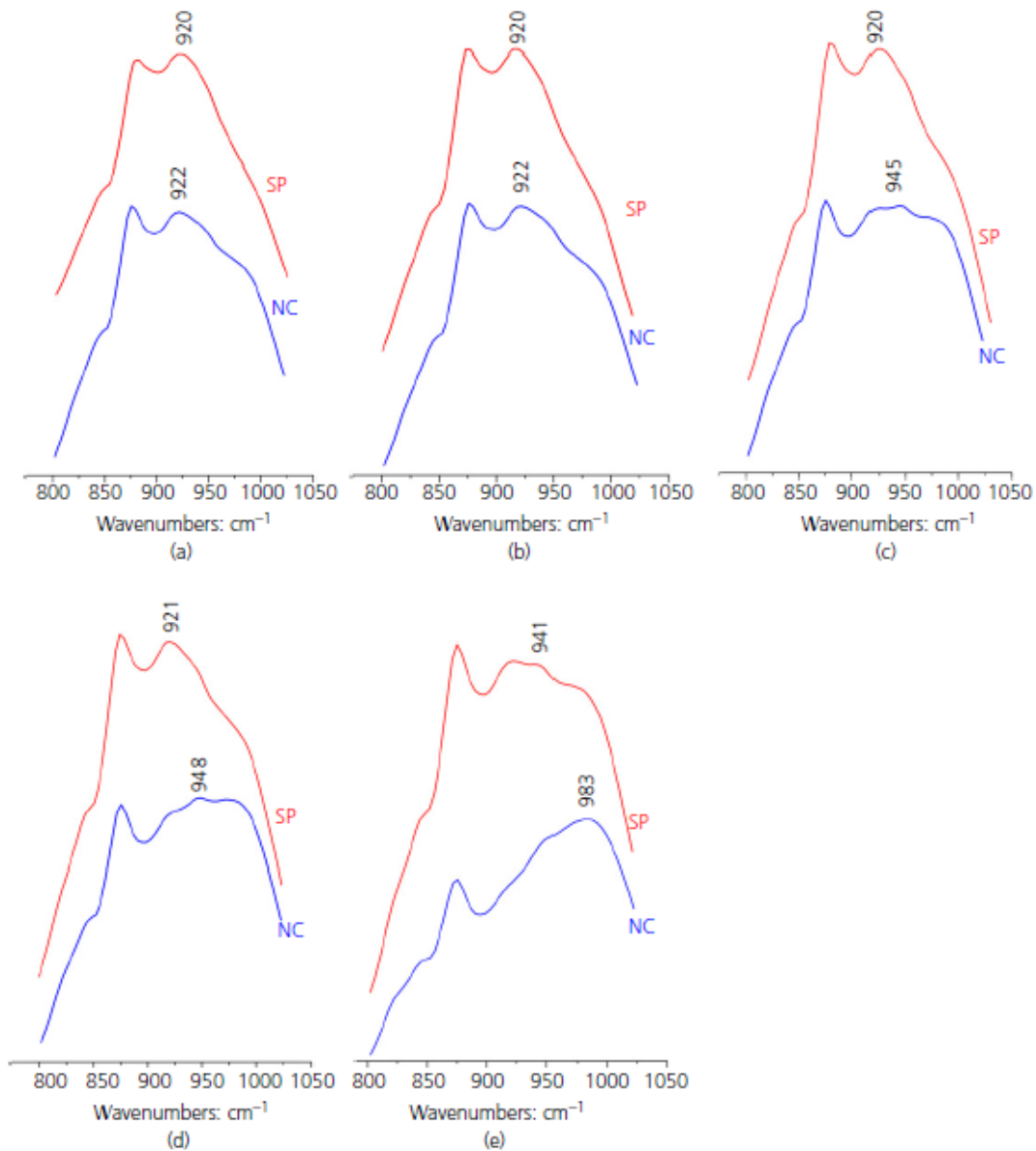


Figure 6.5 FTIR spectra of cement pastes with or without SP: (a) at 8 h; (b) at 9 h; (c) at 10h; (d) at 11 h; (e) at 12 h

6.2.3 FTIR study on cement paste incorporating CNTs

Comparative experiment between the blank cement sample and the sample reinforced with CNTs was conducted. CNTs are first dispersed with the use of sonication energy, and then added to

cement during mixing. In general, a certain amount of SP should be added when the CNTs are treated by ultrasonication for dispersion in order to prevent re-agglomeration of the CNTs after dispersion. However, in this experiment, considering that even a tiny amount of SP could significantly influence the reaction speed of cement hydration, which might lead to difficulty in controlling the entire test process, the influences of the SP must be removed in the experimental design. Thus, the CNTs are sonicated without the use of SP, and immediately mixed into the cement after the dispersion operation to ensure the optimum dispersion effect. The dosage of CNT is 0.08 % to cement weight, and similar casting and curing rules are used as mentioned above.

Figure 6.6 exhibits the FTIR spectra of the cement samples without or with CNTs, clearly revealing the shifting process of the characteristic peak from 921 to 983 cm^{-1} . During this process, the peak values of plain cement and CNT samples at each age exhibit a degree of consistency. Therefore, CNTs did appear to affect the polymerization of the silicon-oxygen tetrahedrons in the C-S-H gel at an early age, or at least from the current FTIR test.

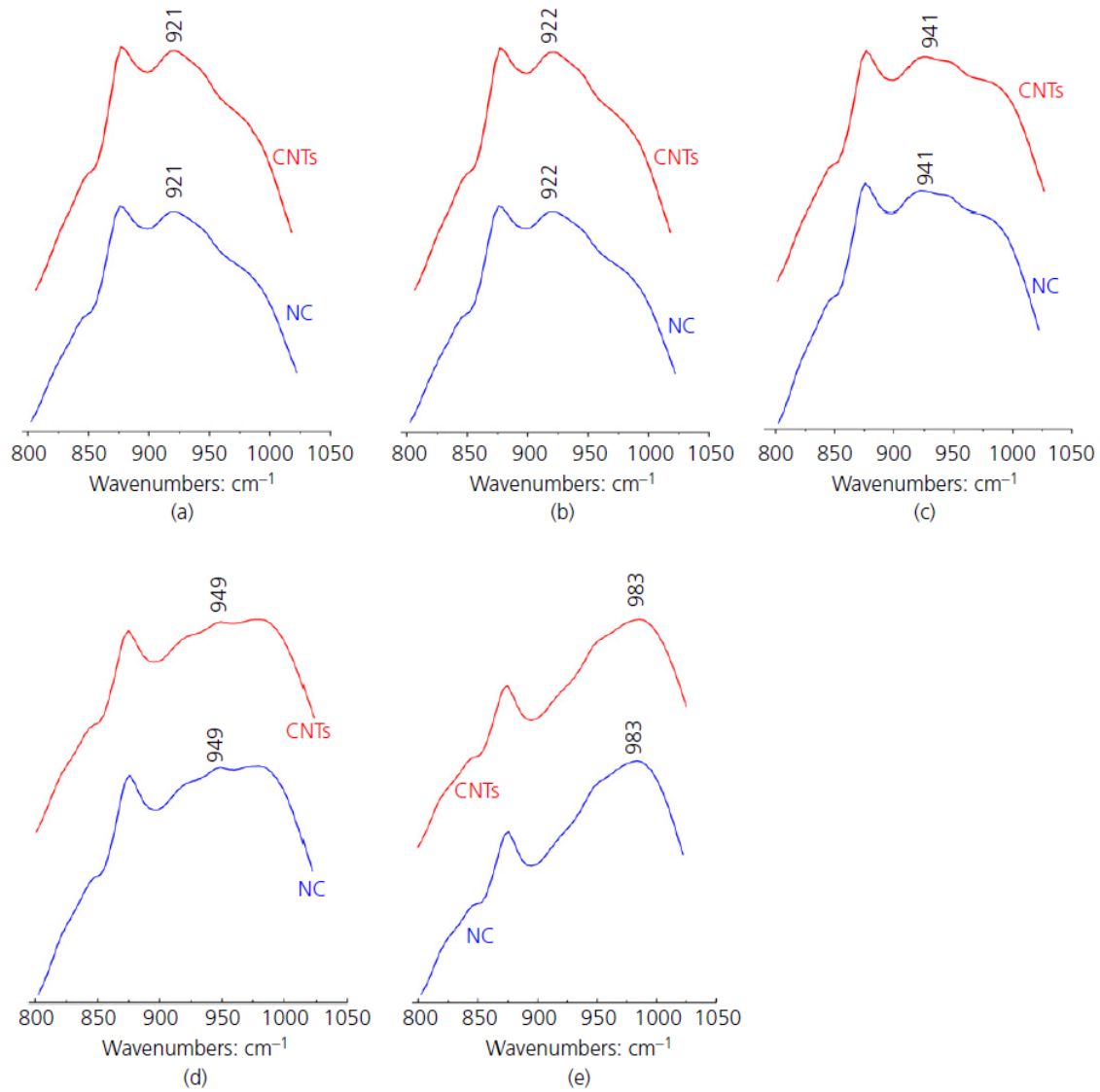


Figure 6.6 FTIR spectra of cement pastes with and without CNT: (a) at 8 h; (b) at 9 h; (c) at 10h; (d) at 11 h; (e) at 12 h

6.3 Semi-adiabatic Calorimetry Test

The hydration of cement is basically a series of chemical reactions, which will company with heat generation. And the quantification of the heat generation is commonly used as a way to study cement hydration. Hydration temperature reflects the heat release of the hydration reaction

in the system, and the hydration rate of cement is exactly consistent with hydration heat. In the past, isothermal calorimetry has been frequently used to serve the purpose. While due to the limit of the equipment in the lab, a semi-adiabatic calorimetry test is performed, and it is good enough to perform the comparison test for cement sample with or without CNTs. The mix proportion is similar to the samples used in FTIR test, and the semi-adiabatic calorimetry drum is shown in Fig. 6.7. Paste samples are mixed and cast in 5 cm x 10 cm cylindrical molds. A thermocouple is inserted in the cylinder immediately after casting, which is connected to a data logger and reads the temperature every five seconds. The sample is then covered with a cap and put in the small chamber in the calorimetry drum. The drum is well insulated from the environment to prevent heat loss.

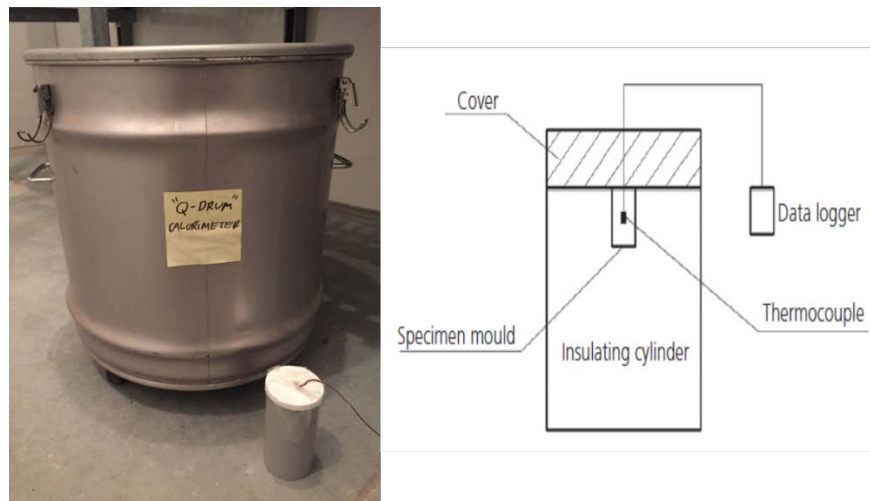


Figure 6.7 Picture of semi-adiabatic calorimetry

The temperature sensor measures the temperature evaluation, and result is shown in Fig 6.8. The starting temperature of all three samples is around 25°C , and rise to 70°C . The shape of temperature evaluation curve of all three samples are consistent, meaning the overall heat release is the same. Among them, the curve of sample with SP shifts to the right, indicating the

hydration is delayed for about 2 hours. The curve of sample with CNTs almost overlaps with the plain cement paste, which is found to be in consistent with the results of FTIR. There is no obvious evidence proving that CNTs change the hydration rate of cement paste.

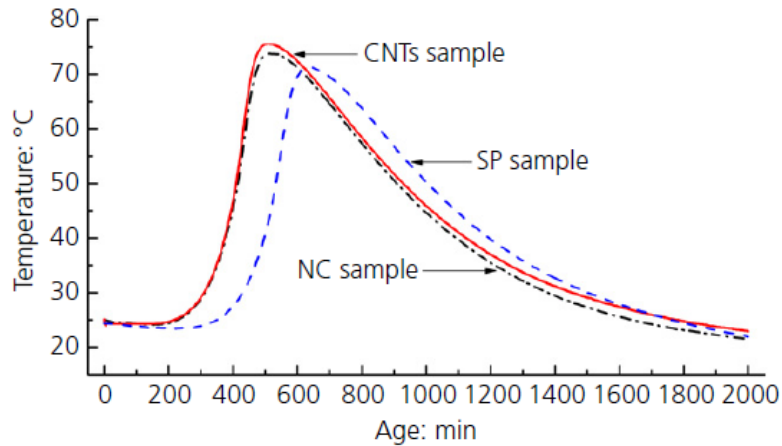


Figure 6.8 Semi-adiabatic calorimetry result

6.4 XRD Test

X-ray diffraction is another material characterization tool, which is largely used to provide information about the phase transitions, crystallite size, crystal structure, lattice parameters, and et al. The identification of different hydration phases, such as calcium hydroxide (portlandite) and ettringite, is based on the unique diffraction patterns of each compound or material under X-ray. The XRD test is still in process, and the results will be included in the final version of this dissertation.

6.5 Summary

In this chapter, the hydration process of cement at early age is characterized by FTIR spectroscopy, semi-adiabatic calorimetry, and XRD. The following conclusions could be drawn.

- (1) FTIR is a simple and rapid research method in operation, which can reflect the basic variation in the primary cement hydration products. As the hydration reaction proceeded, the peak value corresponding to silicon-oxygen vibrations in the FTIR spectrum shifted from low wavenumbers to high wavenumbers, which not only reflected the polymerization process of the silicon-oxygen tetrahedrons in the C-S-H gel, but also the hydration reaction speed of the cement paste at this stage. This viewpoint is confirmed by the experiment for the samples was added SP.
- (2) The shifting characteristics of the absorption peaks in the range 800-1025 cm^{-1} for the samples at the ages of 8-12 h are comprehensively investigated in this study. The research results show that the shifting speed of the characteristic peak for the blank sample is exactly the same as that for the sample reinforced with CNTs. Therefore, the addition of CNT materials into Portland cement doesn't influence the hydration reaction at early age, or at least it can't be detected by the aforementioned techniques. This conclusion is verified by the semi-adiabatic calorimetry test, where the heat of hydration is measured in the first 2 days. However, both the FTIR test and semi-adiabatic calorimetry test are performed with pure cement paste without the addition of fine or coarse aggregates. Previous chapters argue that the modification is more obvious on the interface between aggregate and bulk paste, resulting a better behavior of CNT added mortar and concrete. Further study on the interface area by FTIR test should be considered.

References

- [1] J. Björnström, A. Martinelli, A. Matic, L. Börjesson, I. Panas, Accelerating effects of colloidal nano-silica for beneficial calcium–silicate–hydrate formation in cement, *Chem. Phys. Lett.* 392 (2004) 242–248. doi:<https://doi.org/10.1016/j.cplett.2004.05.071>.
- [2] P. Mondal, S. Shah, L. Marks, J. Gaitero, Comparative Study of the Effects of Microsilica and Nanosilica in Concrete, *Transp. Res. Rec. J. Transp. Res. Board.* 2141 (2010) 6–9. doi:10.3141/2141-02.
- [3] G. Land, D. Stephan, The influence of nano-silica on the hydration of ordinary Portland cement, *J. Mater. Sci.* 47 (2012) 1011–1017. doi:10.1007/s10853-011-5881-1.
- [4] R. Yu, P. Spiesz, H.J.H. Brouwers, Effect of nano-silica on the hydration and microstructure development of Ultra-High Performance Concrete (UHPC) with a low binder amount, *Constr. Build. Mater.* 65 (2014) 140–150. doi:<https://doi.org/10.1016/j.conbuildmat.2014.04.063>.
- [5] J.J. Thomas, H.M. Jennings, J.J. Chen, Influence of Nucleation Seeding on the Hydration Mechanisms of Tricalcium Silicate and Cement, *J. Phys. Chem. C.* 113 (2009) 4327–4334. doi:10.1021/jp809811w.
- [6] P. Hou, S. Kawashima, D. Kong, D.J. Corr, J. Qian, S.P. Shah, Modification effects of

- colloidal nanoSiO₂ on cement hydration and its gel property, *Compos. Part B Eng.* 45 (2013) 440–448. doi:<https://doi.org/10.1016/j.compositesb.2012.05.056>.
- [7] S. Kawashima, P. Hou, D.J. Corr, S.P. Shah, Modification of cement-based materials with nanoparticles, *Cem. Concr. Compos.* 36 (2013) 8–15.
doi:<https://doi.org/10.1016/j.cemconcomp.2012.06.012>.
- [8] T. Shi, Y. Gao, D.J. Corr, S.P. Shah, FTIR study on early-age hydration of carbon nanotubes-modified cement-based materials, *Adv. Cem. Res.* (2018) 1–9.
doi:10.1680/jadcr.16.00167.
- [9] S.N. Ghosh, S.K. Handoo, Infrared and Raman spectral studies in cement and concrete (review), *Cem. Concr. Res.* 10 (1980) 771–782. doi:[https://doi.org/10.1016/0008-8846\(80\)90005-8](https://doi.org/10.1016/0008-8846(80)90005-8).
- [10] T.L. Hughes, C.M. Methven, T.G.J. Jones, S.E. Pelham, P. Fletcher, C. Hall, Determining cement composition by Fourier transform infrared spectroscopy, *Adv. Cem. Based Mater.* 2 (1995) 91–104. doi:[https://doi.org/10.1016/1065-7355\(94\)00031-X](https://doi.org/10.1016/1065-7355(94)00031-X).
- [11] M.Y.A. Mollah, W. Yu, R. Schennach, D.L. Cocker, A Fourier transform infrared spectroscopic investigation of the early hydration of Portland cement and the influence of sodium lignosulfonate, *Cem. Concr. Res.* 30 (2000) 267–273.

doi:[https://doi.org/10.1016/S0008-8846\(99\)00243-4](https://doi.org/10.1016/S0008-8846(99)00243-4).

[12] P.C. Hewlett, *Lea's Chemistry of Cement and Concrete*, Butterworth-Heinemann, Oxford, 2003.

[13] E. Lippmaa, M. Maegi, A. Samoson, G. Engelhardt, A.R. Grimmer, Structural studies of silicates by solid-state high-resolution silicon-29 NMR, *J. Am. Chem. Soc.* 102 (1980) 4889–4893. doi:10.1021/ja00535a008.

[14] H.F.W. Taylor, *Cement chemistry*, Thomas Telford Publishing, 1997.
doi:doi:10.1680/cc.25929.

[15] I.F. Sáez del Bosque, S. Martínez-Ramírez, M.T. Blanco-Varela, FTIR study of the effect of temperature and nanosilica on the nano structure of C–S–H gel formed by hydrating tricalcium silicate, *Constr. Build. Mater.* 52 (2014) 314–323.
doi:<https://doi.org/10.1016/j.conbuildmat.2013.10.056>.

Chapter 7

Transport Properties of CNT Reinforced Concrete

7.1 Introduction

The durability of cement-based material largely depends on its transport property, which is the movement of free water and ions through capillary pores. Based on the previous research on autogenous shrinkage and corrosion potential, there is a large possibility that CNT/CNF alters the microstructure as well as the pore system. A direct method to test the hypothesis is to investigate the transport property, which is determined by the microstructure of cement-based material. Transport properties describe the rate of ingress of deleterious species, such as water, chloride, and sulfate, from the environment into the cement matrix and their components. The

transport properties are direct indications of durability of concrete material, which determines the service life of concrete structures. It is believed that capillary voids larger than 50 nm referred to as macropores are detrimental to strength and impermeability, whereas voids smaller than 50 nm are more related to drying shrinkage and creep[1]. The macropores play an important role in the durability of concrete. The incorporation of nanomaterials, namely nanosilica and nanoclay, in concrete matrix is found to densify its microstructure, reduce the formation of microcracks, and thus improve its transport properties[2]. Another study analyzed the pore structure of CNT or carbon fiber added cement mortar, and it found the use of CNTs decreases the porosity of cement and reduces the total pore volume[3]. The transport processes for deleterious substances through concrete can be distinguished as diffusion, absorption and permeation depending on the driving forces and the nature of the transported matter[4]. In this chapter, the transport properties of CNT added concrete, including water sorptivity and chloride penetration, are examined in this chapter. Water sorptivity test is used to measure the rate of water absorption into the dry concrete, which is due to the surface tension acting in capillaries. Chloride penetration test measures the chloride diffusion, which is due to a concentration gradient across concrete. The penetration of chloride ions is maintained unidirectional by sealing all except one surface of the specimen. Permeability is the characterization of the ease of a fluid medium passing through the sample under the action of a pressure differential. The permeability property is not directly measured in the thesis, such as the rapid chloride permeability test. The reason is that CNT itself is electrical conductive and the conductivity of cement mortar, as the permeability measurement parameter, will be heavily affected. It is expected that CNF reinforced cement-based composites would exhibit improved transport properties relative to the conventional cement-based composites. In addition, the half-cell potential test is performed on the concrete embedded with

steel rebars. The reinforcement corrosion is the main cause of deterioration of concrete, causing serious durability issue. The ingress of chlorides depassivate the steel in concrete, and in the presence of oxygen and water, steel may start corroding.

7.2 Experiment Methods

7.2.1 Water sorptivity test

The water sorptivity test is carried out to determine the rate of absorption of water by concrete and evaluate the effect of CNTs on the development of capillary pores and capillary water suction of cementitious materials. The experiment is conducted according to ASTM C1585, which is shown in Fig. 7.1 Concrete cylindrical disks with the dimension of 100 mm x 50 mm are cast and cured to 14 days in humidity chamber (100% in humidity, 23 °C). Then, the specimens are oven-dried at 105 °C for 24 hours to remove the free water in the pores, and kept at another environmental chamber of 50 °C for temperature and 80% for relative humidity for 3 days. After that, the specimens are placed in a sealed container for 15 days before testing.

The principle of the sorptivity testing is that a specimen has one surface in free contact with water while the other surfaces are sealed with silicon gel. The quantity of water absorbed in time period of 30 minutes is regularly measured by weighing the specimen to determine the initial absorption from 1 min to first 6 hours. The absorption, I , is the change in mass divided by the product of the cross-section area of the test specimen and the density of water. The initial rate of water absorption value ($\text{mm/s}^{1/2}$) is calculated as the slope of the line that is the best fit plotted against the square root of time ($\text{s}^{1/2}$). The plot has to be linear with a regression coefficient (r^2), of less than an arbitrary value of 0.98.

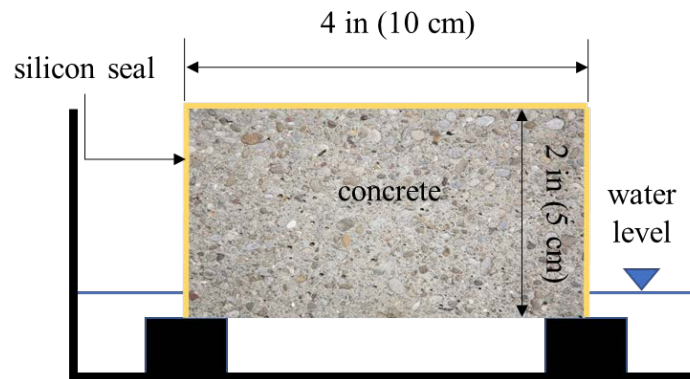


Figure 7.1 Schematic of water sorptivity test

7.2.2 Chloride penetration test

In order to investigate the effect of CNFs on chloride penetration of concrete, the penetration depth of chloride ions is measured according to ASTM C1585 on concrete specimens of 100 mm in diameter and 75 mm in thickness. After 14 days of wet curing, the specimens are fully immersed in the aqueous solution containing NaCl for 40 days, as shown in Fig. 7.2. The top surface of specimen is in free contact of the NaCl solution, while the other surfaces are sealed with silicon gel. Afterwards, the colorimetric method is applied to determine the penetration depth of chloride, see Fig 7.3. In this case, the spraying of 0.1 N AgNO_3 solution is applied on a cross-section of split concrete leads to the formation of white and brown regions subjected to the penetration of chloride.

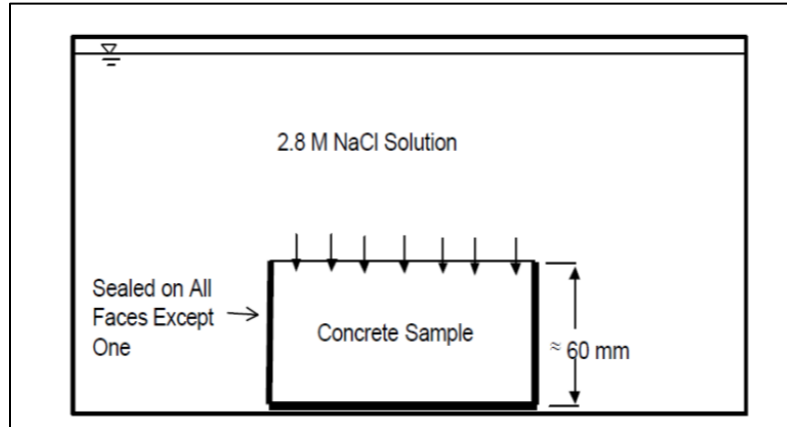


Figure 7.2 Set-up of chloride penetration test

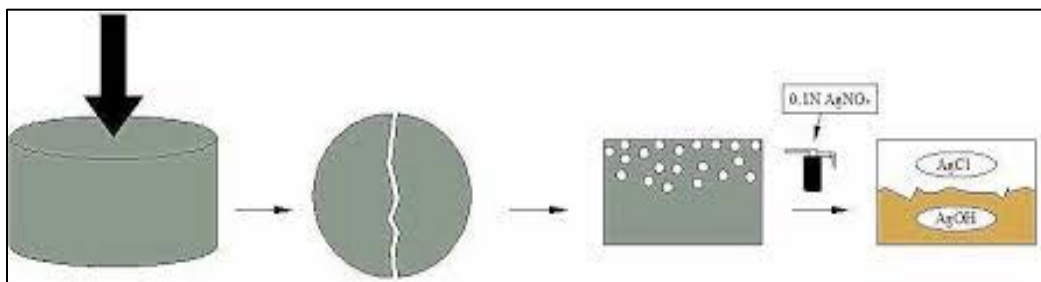


Figure 7.3 Colorimetric measurement of penetration depth

7.2.3 Half-cell potential test

Corrosion of steel in concrete is a major contributor to degradation of concrete in aggressive environments, and threatens the viability and durability of reinforced concrete structures. Since the addition of CNT increase the conductivity of cementitious materials[5], there is concern about the increase in galvanic activity and its impact on steel reinforcement corrosion. However, since CNT is believed to densify the microstructure of the cement matrix by reducing the fine pores, chloride ion intrusion could be arrested which would greatly improve corrosion behavior.

Konsta-Gdoutos et al. examined the corrosion resistance of CNT and CNF reinforced mortars. Both nanoscale fibers were included at an amount of 0.1 wt%. As it is shown in Fig. 7.4 [modified Fig. 9 in Ref.[6]] resistance to corrosion was greatly improved for both nano-reinforced mortars by significantly delaying the onset of the corrosion reaction.

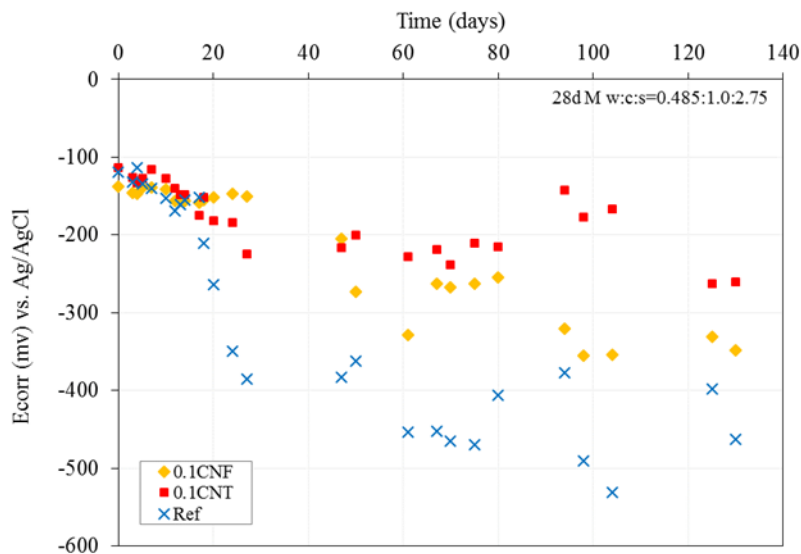


Figure 7.4 Half-cell Potential (Ag/AgCl) as a function of exposure time for reinforced cement mortars in 3.5 wt% NaCl Solution (Based on [6])

To further examine the ingress of chloride ions into concrete matrix, the half-cell potential test is conducted, which is followed with the ASTM C876[7]. Saturated copper/copper sulfate (Cu/CuSO₄) will be used as the reference electrode, and a voltmeter will be used to measure the corrosion potential. Fig.7.5 illustrate the test set-up for half-potential testing. The 4×8-in concrete cylinders embedded with four 1/2-in-diameter steel rebars will be prepared for corrosion potential testing, see Fig. 7.6. The concrete cylinders will be cured in lime-saturated water for 7 days after demolding, and then partially immersed in 3.5% sodium chloride(NaCl) solution to

accelerate the corrosion behavior of the steel. The half-cell unit measures changes in corrosion potentials over time, and will indicate whether the steel is actively corroding. The reading will be taken twice every week until its half-cell potential proceeds below -350mV , and then the sample will be cut in the middle for the examination of the steel corrosion.

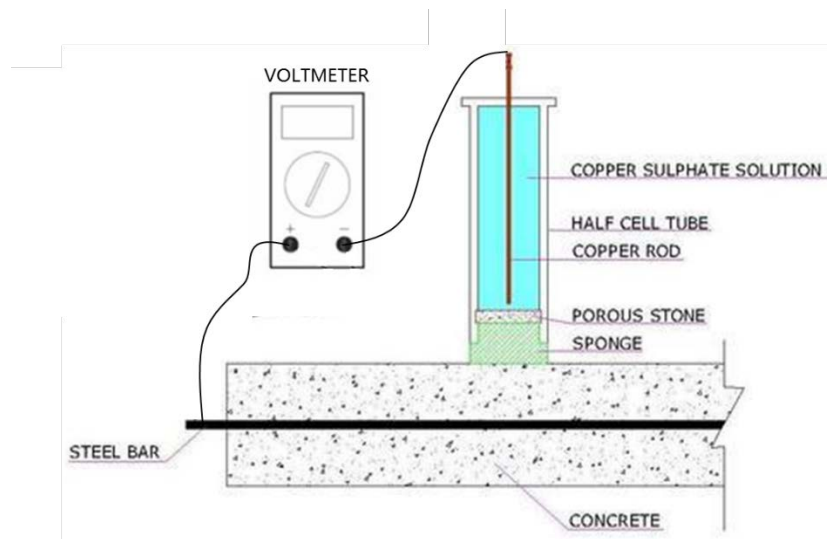


Figure 7.5 Schematic of half-cell potential testing

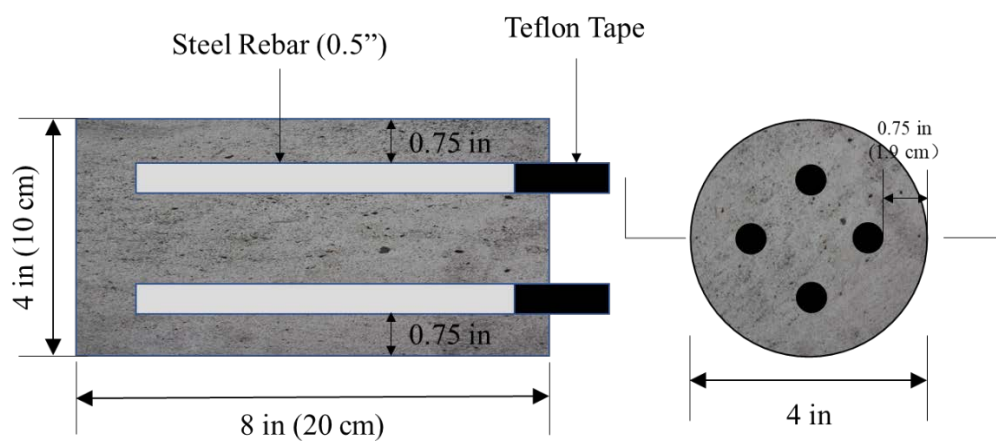


Figure 7.6 Reinforced concrete sample for half-cell potential testing

7.3 Experiment Results

7.3.1 Water sorptivity test

The rate of water absorption of plain concrete and CNF added concrete after 14 days of water curing are presented in Fig. 7.6. The water absorption of specimens is fitted using linear regression and the equation obtained is used to describe the capillary actions during 6 hours of testing. It can be seen that the cumulative volume of water absorbed in the concrete increased with the square root of time. The slope of the obtained line in Fig.7.6 defines the sorptivity of different concretes during the initial six hours of testing. The result shows that the rate of water absorption of plain concrete is reduced due to addition of 0.1 wt% of CNFs. According to the summarized sorptivity values in Table 1 the minimum water sorptivity at 14 days is 64×10^{-4} mm/sec^{1/2} for concrete with the addition of CNFs. The value is 15% lower when compared to plain concrete without CNF, which has the minimum water soptivity of 76×10^{-4} mm/sec^{1/2}.

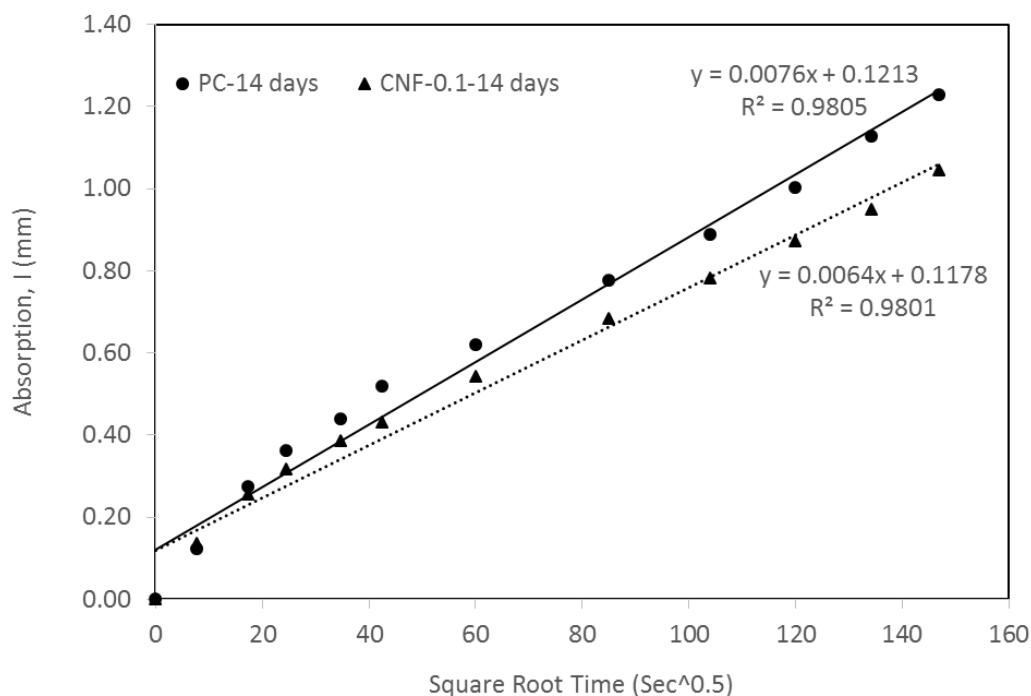


Figure 7.7. Water absorption rate of concretes containing 0.1 wt% CNF

Table 7.1. Sorptivity value of concrete containing CNFs after 14 days of curing

Type of mixes	Sorptivity value ($\times 10^{-4} \text{ mm/s}^{1/2}$)
Plain Concrete	76
CNF-0.1	64

7.3.2 Chloride penetration depth

The colorimetric method uses the principle of which a white deposit is formed through reaction between silver ions (Ag^+) and chloride ions (Cl^-). When the 0.1 N AgNO_3 is sprayed to concrete surface exposed to chloride ions, additional precipitation reaction beside white-precipitation reaction happens. That is, after creating of calcium hydroxide (CH) resulting from the hydration of cement, hydroxide ions at voids make brown-precipitation through reaction with silver ions.

On this experiment, seven measurements are performed in every 10 mm along the horizontal direction in order to obtain the average of chloride penetration depth. It was found that the average of chloride penetration depth on PC and CNF concretes are 16.5 mm and 14 mm, respectively, indicating that the addition of 0.1% CNF can decrease chloride penetration depth, likely through improving the microstructure of the cement-based materials.

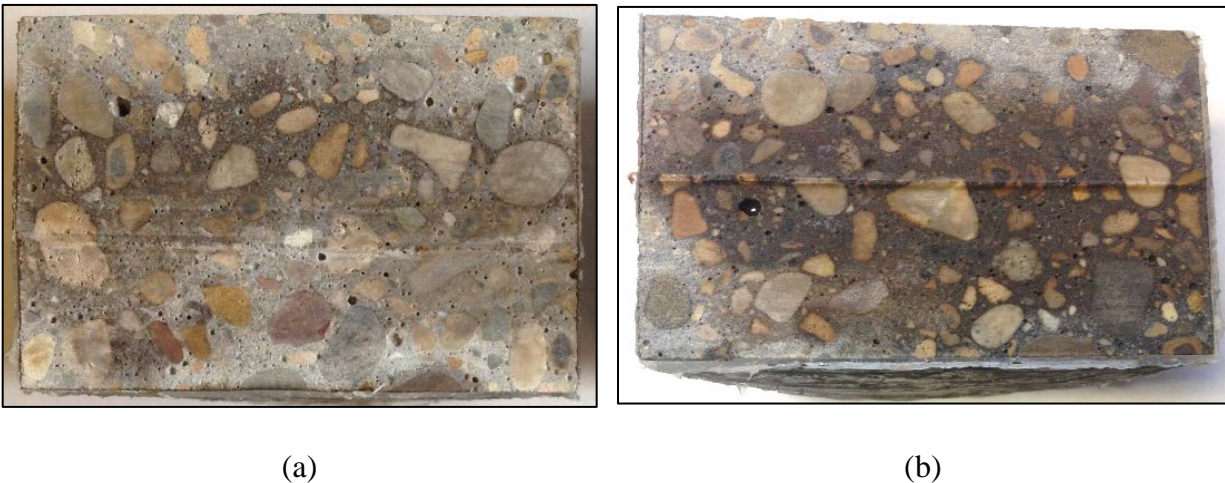


Figure 7.8. The difference of penetration depth between (a) plain concrete;
(b) concrete with CNF

7.3.3 Half-cell potential test

The half-cell potential test is still in the process and the measurement will be complete by the end of August (75 days period). The final results will be included in the final version of this thesis.

7.4 Summary

Three experiments are conducted to evaluate different aspects of the movement process of water or chloride ions. The incorporation of well dispersed CNFs is found to be effective on improving

the transport properties of concrete, which are important physical properties of concrete in relation to the durability parameters.

- (a) The water sorptivity value decreases from 76 to $64 \times 10^{-4} \text{ mm/s}^{1/2}$ due to the addition of 0.1 wt% CNF (to cement weight) at the age of 14 days.
- (b) The chloride penetration is slowed down in the CNF added concrete samples compared to plain concrete indicated by the penetration depth.
- (c) The half-cell potential measures the resistance of the reinforcement corrosion under accelerated condition, and the measurement is still in progress.

The enhancement of transport properties is due to the improvement of material's microstructure. Through the refinement of the porous structure, CNTs increase the volumetric stability of the composites by reducing autogenous shrinkage, which is discussed in chapter 3. Even though direct benefits of CNFs in cement-based composites have been identified, the mechanisms by which they interact with the hydration reaction to modify properties of the cement matrix are not yet fully understood.

Reference

- [1] P.K. Mehta, P.J.M. Monteiro, Concrete: Structure, Properties, and Materials, 2nd Ed, 1993.
- [2] X. He, X. Shi, Chloride permeability and microstructure of Portland cement mortars incorporating nanomaterials, *Transp. Res. Rec. J. Transp. Res. Board.* (2008) 13–21.
- [3] G.Y. Li, P.M. Wang, X. Zhao, Mechanical behavior and microstructure of cement composites incorporating surface-treated multi-walled carbon nanotubes, *Carbon N. Y.* 43

- (2005) 1239–1245. doi:<https://doi.org/10.1016/j.carbon.2004.12.017>.
- [4] L. Basheer, J. Kropp, D.J. Cleland, Assessment of the durability of concrete from its permeation properties: a review, *Constr. Build. Mater.* 15 (2001) 93–103.
doi:[https://doi.org/10.1016/S0950-0618\(00\)00058-1](https://doi.org/10.1016/S0950-0618(00)00058-1).
- [5] M.S. Konsta-Gdoutos, C.A. Aza, Self sensing carbon nanotube (CNT) and nanofiber (CNF) cementitious composites for real time damage assessment in smart structures, *Cem. Concr. Compos.* 53 (2014) 162–169.
doi:<https://doi.org/10.1016/j.cemconcomp.2014.07.003>.
- [6] M. Konsta, G. Batis, P. Danoglidis, A. K. Zacharopoulou, E. K. Zacharopoulou, M. Falara, S. Shah, Effect of CNT and CNF loading and count on the corrosion resistance, conductivity and mechanical properties of nanomodified OPC mortars, 2017.
doi:[10.1016/j.conbuildmat.2017.04.112](https://doi.org/10.1016/j.conbuildmat.2017.04.112).
- [7] ASTM C876-15, Standard Test Method for Corrosion Potentials of Uncoated Reinforcing Steel in Concrete, West Conshohocken, PA, 2015. www.astm.org.

Chapter 8

Conclusions and Scope of Future Work

8.1 Conclusions

This thesis investigates the performance of cement-based composites with the addition of well-dispersed CNFs, which particular emphasis on the characterization of cement nanocomposites in the nano- and microscales and the mechanism of CNTs impacts on the cementitious matrix and interfacial transitional zone(ITZ). The characterization work includes the mechanical properties (flexural strength, Young's modulus, compressive strength), autogenous shrinkage and shrinkage cracking, durability, and early age hydration. Though the test results have shown improvement on mechanical properties for both cement paste, mortar and concrete, the percentage is more significant in mortar and concrete compared to cement paste. To explain this, my hypothesis has

been that CNT is modifying the chemical structure of cement hydrates at the nanoscale at ITZ as well as bulk paste. Nano-characterization techniques has been employed with the focus on the ITZ, and a finite element model is developed to predict the Young's modulus considering the change at ITZ. The dispersion technique of CNT is also discussed in this thesis along with the using of ultraviolet-visible spectroscopy (UV-Vis) as a characterization technique of dispersion effect within aqueous solution. The results are quite promising and motivate the proposed study of CNT additions to concrete.

The main conclusions made in the course of this study are summarized below:

- (1) Like other fiber reinforced cement composites, homogenous distribution of CNT is found to be a key factor determining the properties of the resulting composites. Conventional mixing does not give enough shear force to separate agglomerated fibers, and pre-agitation is widely employed to achieve a full and stable dispersion within an aqueous solution. In this dissertation, well-dispersed CNT suspensions are achieved with a combination use of ultrasonication energy and superplasticizer, then characterize the dispersion effect with UV-Vis.
- (2) The results of mechanical tests indicate that CNF addition could increase the flexural strength and Young's modulus for both cement paste and mortar materials. By adding 0.1 wt% CNFs (to cement weight), the flexural strength is improved by 21% and 34% for cement paste and mortar, respectively. Young's modulus is increased by 18% and 28% for cement paste and mortar respectively, while Young's modulus of concrete is increased by 29%. The effect is more obvious for mortar and concrete especially considering the actual fiber amount added is substantially less in mortar than in paste.

- (3) The autogenous shrinkage tests show that the CNF has the effect of mitigating autogenous shrinkage for both paste and mortar sample at early ages. Similarly, CNF's effect is larger in mortar sample than in paste sample. In addition, CNF could restrain the expansion of the crack width from the restrained ring test showing potential self-healing capability.
- (4) The nano-scale metrology techniques have been adopted to investigate mechanical, structural, and chemical properties of ITZ in CNF reinforced cement concrete. The samples of cement mortar and concrete with and without CNFs are prepared. The quantitative nano-mechanical mapping (based on atomic force microscopy, AFM) technique is adopted to measure the Young's modulus of ITZ. The test samples are then studied by SEM/EDX to conduct elemental and phase investigation of ITZ. Based on AFM QNM test, it can be concluded that CNF is capable of improving the Young's modulus of ITZ. The average Young's modulus is increased by 36.7% for ITZ in cement mortar, and the Young's modulus of ITZ is increased by 55%~63% in cement concrete. Based on SEM/EDX observation, CNF reinforced ITZ does have richer C-S-H phase than plain ITZ. Since C-S-H gel is mainly responsible for the stiffness and strength, ITZ with CNFs will have a higher modulus of elasticity.
- (5) A new finite element model is developed to link the real interfacial condition to the macro-mechanical behavior of cement concrete, where an "effective aggregate" model is employed that considers the enhancement on ITZ as well as on bulk paste. The simulation results correspond well with the test results with concrete samples, confirming the effect on the nanomodification of ITZ. Based on the numerical simulation, it is found that a larger thickness of ITZ with a relatively low Young's modulus has more noticeable

effect on the Young's modulus of concrete, and the effect of ITZ thickness is negligible when the Young's modulus of ITZ is large enough.

(6) To study the CNF's effect on cement hydration at early ages, FTIR, semi-adiabatic calorimetry and XRD test are performed on cement pastes. The results of FTIR tell no difference on the shifting characteristics of the absorption peaks at the hydration ages of 8-12 hours with or without the addition of CNFs. The semi-adiabatic calorimetry test shows the similar result that there is no different between the plain cement or cement with CNTs indicated by the evolution of hydration heat. In conclusion, CNFs are not able to modify the hydration rate of cementitious materials.

(7) Transport properties is examined with two tests: water sorptivity and chloride penetration. The water sorptivity test finds the water absorption rate is decreased by 16% at the age of 14 days. The chloride penetration depth is measured as the indication of the chloride diffusion rate, which is also found to be reduced due to the addition of CNFs. The improvement of transport properties of concrete material proves that there is a refinement on the microstructure of cement matrix probably due to the filler effect of CNFs.

8.2 Scope of Future Work

8.2.1 Dispersion upscaling

The dispersion method used in this dissertation is proved to be effective to disperse CNT/CNF in aqueous solution. However the large consumption of ultrasonication energy, and complexity of operation process is not suitable for large quantity production, which is required for construction

in the field. The current dispersion technique uses lab scale ultrasonication equipment which limits the dispersion quantity up to 400 ml/batch. One way to consider is to develop a more concentrated CNT/CNF solution without increasing the ultrasonication energy by the use of stronger surfactant and optimizing other parameters while ultrasonication. Another way is to use large scale shear mixing technique which has been successfully utilized in the dispersion of other nanomaterials in organic solution.

8.2.2 Concrete characterization

With the beneficial effect of CNT on important properties such as Young's modulus in concrete established, future work is proposed to investigate the remaining critical properties related to the use of concrete as a structural material. Three major thrusts are proposed to fill gaps in the current state of concrete research related to the nanomodification with CNT: (1) Creep, (2) Drying Shrinkage.

The viscoelastic properties of concrete have been widely studied and are critical to the viability of concrete as a structural material. Due to observations that CNT modification has the potential to alter the nano- and micro-structure of the material in a beneficial way, there is reason to believe that creep behavior can also be expected to improve.

Another major issue related to volume change and dimensional stability in structural concrete is drying shrinkage. Drying shrinkage is caused by the evaporation of capillary water in cement paste after hardening. Drying shrinkage can cause cracking, which can induce durability concerns related to the ingress of water, such as corrosion of steel reinforcement. From prior

research, the incorporation of CNT reduces the autogenous shrinkage. Of particular interest is CNT's ability to restrain drying shrinkage of concrete.

8.2.3 Mechanism of CNT's effect on property improvement

FTIR and calorimetry results have shown that CNTs doesn't accelerate or delay the hydration of cement, while SEM/EDS proves there is a chemical modification on the ITZ due to the addition of CNTs. A possible mechanism of CNT's positive effect on the Young's modulus is the alteration of the nanostructure of C-S-H. However, the change of the nanostructure of C-S-H is difficult to detect due to two main reasons: difficulty in separating it from other phases and its broad diffraction signal. A further investigation is needed to examine the change of nanostructure of C-S-H gels when they are separated from other phases. In addition, the test results show that the enhancement at ITZ plays an important role on CNT's effect. Another possible mechanism is CNTs enhance the adhesion force between the paste and the aggregate, which could reinforce the ITZ in the concrete matrix. It is worth to investigate the potential improvement of the interaction between aggregate and cement paste with the addition of CNFs.